



**HAL**  
open science

# Investigation of geodesic acoustic mode flow oscillations using Doppler reflectometry in ASDEX Upgrade

Patrick Simon

► **To cite this version:**

Patrick Simon. Investigation of geodesic acoustic mode flow oscillations using Doppler reflectometry in ASDEX Upgrade. Plasma Physics [physics.plasm-ph]. Université de Lorraine, 2017. English. NNT : 2017LORR0076 . tel-01591866

**HAL Id: tel-01591866**

**<https://theses.hal.science/tel-01591866>**

Submitted on 22 Sep 2017

**HAL** is a multi-disciplinary open access archive for the deposit and dissemination of scientific research documents, whether they are published or not. The documents may come from teaching and research institutions in France or abroad, or from public or private research centers.

L'archive ouverte pluridisciplinaire **HAL**, est destinée au dépôt et à la diffusion de documents scientifiques de niveau recherche, publiés ou non, émanant des établissements d'enseignement et de recherche français ou étrangers, des laboratoires publics ou privés.



## AVERTISSEMENT

Ce document est le fruit d'un long travail approuvé par le jury de soutenance et mis à disposition de l'ensemble de la communauté universitaire élargie.

Il est soumis à la propriété intellectuelle de l'auteur. Ceci implique une obligation de citation et de référencement lors de l'utilisation de ce document.

D'autre part, toute contrefaçon, plagiat, reproduction illicite encourt une poursuite pénale.

Contact : [ddoc-theses-contact@univ-lorraine.fr](mailto:ddoc-theses-contact@univ-lorraine.fr)

## LIENS

Code de la Propriété Intellectuelle. articles L 122. 4

Code de la Propriété Intellectuelle. articles L 335.2- L 335.10

[http://www.cfcopies.com/V2/leg/leg\\_droi.php](http://www.cfcopies.com/V2/leg/leg_droi.php)

<http://www.culture.gouv.fr/culture/infos-pratiques/droits/protection.htm>

# Investigation of geodesic acoustic mode flow oscillations using Doppler reflectometry in ASDEX Upgrade

Von der Fakultät Energie-, Verfahrens- und Biotechnik der Universität Stuttgart  
zur Erlangung der Würde eines Doktors der  
Naturwissenschaften (Dr. rer. nat) genehmigte Abhandlung

Vorgelegt von

Patrick Simon

aus Mülheim an der Ruhr

Hauptberichter:	Prof. Dr. G. Tovar
Mitberichter:	Prof. Dr. G. Bonhomme
Mitberichter:	Prof. Dr. U. Stroth
Mitberichter:	Prof. Dr. S. Heuraux
Vorsitzender:	Prof. Dr. J. Starflinger

Tag der mündlichen Prüfung: 10.07.2017

Institut für Grenzflächenverfahrenstechnik und Plasmatechnologie  
der Universität Stuttgart

2017



# Abstract

One of the most important scientific challenges of today is the development of new technologies to satisfy the world's growing demand for energy in the face of declining fossil resources. One promising approach to providing energy is nuclear fusion, which in its most technically advanced application uses a hot plasma that is magnetically confined in a toroidal chamber known as a tokamak. Its efficiency, however, is limited by the transport of particles and heat due to turbulence in the edge of the fusion plasma. A thorough understanding of the complex system of plasma turbulence, and any mechanisms connected to its moderation, is therefore needed. The geodesic acoustic mode (GAM) is a radially localised plasma flow oscillation observed in the edge region of tokamak plasmas, and it is an important part of the turbulent system which contributes to the reduction of turbulent transport through velocity shearing.

This thesis investigates the fundamental behaviour of the GAM through a systematic experimental study of its properties in the ASDEX Upgrade tokamak. In particular, the role of the plasma geometry (e.g. the plasma boundary elongation, and whether a limiter or divertor configuration is used) on the scaling of the GAM frequency and amplitude, as well as the GAM radial structure are investigated in detail. The experimental data was obtained with the aid of microwave Doppler reflectometry, a diagnostic technique that can be used to measure plasma flow oscillations, such as the GAM, with high temporal and spatial resolution.

The GAM frequency scaling is compared with multiple theoretical and empirical models. The expected fundamental scaling behaviour of GAM frequency  $f_{\text{GAM}}$  with sound velocity  $c_s$  and major plasma radius  $R_0$  ( $f_{\text{GAM}} \propto c_s/R_0$ ), is reproduced, however, none of the existing models give a satisfyingly accurate prediction. The GAM amplitude is studied in connection with damping rates predicted by models for collisional and collisionless Landau damping processes. It is found, that, for ASDEX Upgrade plasma parameters, finite orbit width effects need to be considered in the calculation of collisionless damping rates, and that, contrary to many theoretical and numerical attempts to model the GAM behaviour, collisional damping also cannot be neglected, and may in fact be dominant in the very edge plasma region. In studying the GAM radial structure, three distinct states are identified for different plasma conditions: a continuum GAM, where the local GAM frequency varies radially,  $f_{\text{GAM}} \propto c_s(r)$ ; a single eigenmode GAM, where the GAM frequency is nearly

constant across its region of existence; and multiple eigenmode GAMs, where two radially neighbouring regions with different locked GAM frequencies exist. Transitions between these states are observed under variations of the plasma geometry. Radial correlation measurements indicate that the GAM does not propagate radially in typical elongated divertor discharges, but that it propagates radially inwards in limiter discharges with low elongation. First results on the magnetic signature of the GAM at ASDEX Upgrade and its poloidal structure are also obtained.

With this study, multiple shortcomings of the current theoretical models and numerical approaches, which are used to investigate the behaviour of GAMs and their role in the overall system of plasma turbulence, have now been clearly identified: the GAM frequency scaling is subject to more influences than is accounted for by any current model; collisional damping, which is often neglected, plays a similar role to collisionless damping and may even be dominant in the region of GAM activity; and the fundamental variation of GAM radial structure must also be properly accounted for in scaling predictions. The experimental results obtained for and presented in this thesis will be able to contribute to the development of future models for GAM behaviour.

# Zusammenfassung

Eine der größten aktuellen wissenschaftlichen Herausforderungen ist die Entwicklung neuer Technologien um den weltweit anwachsenden Energiebedarf zu decken, insbesondere im Angesicht sinkender Verfügbarkeit fossiler Brennstoffe. Einen vielversprechenden Ansatz dazu liefert die Kernfusion, die in ihrer am besten erforschten technischen Anwendung ein heißes Plasma in einer toroidalen Kammer, einem sogenannten Tokamak, magnetisch einschließt. Die Effizienz der Fusion wird jedoch durch den Transport von Teilchen und Energie, bedingt durch Turbulenz in der Randschicht des Plasmas, beschränkt. Daher ist es notwendig ein detailliertes Verständnis des komplexen Systems der Plasmaturbulenz und aller Prozesse, die diese Turbulenz einschränken können, zu entwickeln. Die geodätisch-akustische Mode (GAM) ist eine radial lokalisierte Schwingung der Plasmaflussgeschwindigkeit, die in der Randschicht von Tokamakplasmen beobachtet wird. Sie ist ein wichtiger Teil des gesamten Turbulenzsystems und trägt zur Verringerung des turbulenten Transports durch Verscherung turbulenter Strukturen bei.

In dieser Arbeit wird das fundamentale Verhalten der GAM im Rahmen einer systematischen experimentellen Studie untersucht, durchgeführt am Tokamak ASDEX Upgrade. Insbesondere wird dabei die Rolle der Plasmageometrie (unter anderem mit Hinblick auf die Plasmaelliptizität und die Unterschiede zwischen Limiter- und Divertorkonfiguration) bei der Skalierung der GAM-Frequenz und -Amplitude, sowie der radialen GAM-Struktur, hervorgehoben. Die experimentellen Daten werden mithilfe eines Doppler-Reflektometers erhoben, einer Mikrowellendiagnostik die die Messung von Schwingungen der Plasmaflussgeschwindigkeit, wie zum Beispiel der GAM, mit hoher zeitlicher und örtlicher Auflösung ermöglicht.

Die Skalierung der GAM-Frequenz wird mit mehreren theoretischen und empirischen Modellen verglichen. Das erwartete fundamentale Skalierungsverhalten der GAM-Frequenz  $f_{\text{GAM}}$  mit der Schallgeschwindigkeit  $c_s$  und dem großen Plasmaradius  $R_0$  ( $f_{\text{GAM}} \propto c_s/R_0$ ) wird grob reproduziert, allerdings gibt keines der existierenden Modelle eine Vorhersage mit zufriedenstellender Genauigkeit. Die GAM-Amplitude wird im Zusammenhang mit den Dämpfungsraten untersucht, die von Modellen für stoßbehaftete Dämpfung sowie für stoßfreie Landau-Dämpfung vorhergesagt werden. Dabei wird festgestellt, dass für typische ASDEX-Upgrade-Parameter die Auswirkung der Bahnbreite der Teilchenorbits berücksichtigt wer-

den muss, um die stoßfreien Dämpfungsraten zu berechnen. Weiterhin wird festgestellt, dass die stoßbehaftete Dämpfung, im Gegensatz zu vielen numerischen und theoretischen Ansätzen zur Modellierung des GAM-Verhaltens, nicht vernachlässigt werden darf, sondern allem Anschein nach im äußersten Randbereich des eingeschlossenen Plasmas sogar dominant ist. Bei den Untersuchungen zur radialen GAM-Struktur werden drei unterschiedliche Zustände unter verschiedenen Plasmabedingungen identifiziert: ein GAM-Kontinuum, bei dem sich die lokale GAM-Frequenz radial verändert,  $f_{GAM} \propto c_s(r)$ ; eine einzelne GAM-Eigenmode, mit einer annähernd konstanten GAM-Frequenz innerhalb der Region in der die GAM existiert; sowie mehreren benachbarten GAM-Eigenmoden, bei denen sich die GAM-Frequenz nur schrittweise zwischen Regionen mit konstanter Frequenz ändert. Zwischen diesen Zuständen werden Übergänge bei geeigneter Variation der Plasma-geometrie beobachtet. Radiale Korrelationsmessungen deuten an, dass die GAM in typischen Plasmabedingungen (hohe Elliptizität in Divertorkonfiguration) nicht radial propagiert, dafür gibt es aber Anzeichen innengerichteter radialer Propagation in kreisförmigen Plasmen in der Limiterkonfiguration. Zuletzt werden erste Ergebnisse über die magnetische Signatur der GAM in ASDEX Upgrade, sowie ihrer poloidalen Struktur präsentiert.

Diese Studie ermöglicht nun die klare Identifizierung mehrerer Mängel in den gängigen theoretischen Modellen und numerischen Ansätzen zur Erforschung des GAM-Verhaltens und der Rolle der GAM im Gesamtsystem der Turbulenz: die Skalierung der GAM-Frequenz wird von mehr Faktoren beeinflusst als in den bisherigen Modellen berücksichtigt wird; stoßbehaftete Dämpfung, die oft vernachlässigt wird, spielt in der Plasmaregion in der GAMs existieren eine ähnlich große oder sogar größere Rolle als stoßfreie Landau-Dämpfung; und die fundamental unterschiedlichen Formen der radialen GAM-Struktur müssen in den Skalierungsvorhersagen ebenso berücksichtigt werden. Die experimentellen Ergebnisse, die für diese Arbeit gesammelt wurden und hier präsentiert werden, leisten damit einen Beitrag zur Entwicklung zukünftiger Modelle für das Verhalten der GAM.

# Contents

Title . . . . .	1
Abstract . . . . .	3
Zusammenfassung . . . . .	5
Contents . . . . .	7
<b>List of abbreviations and symbols</b>	<b>11</b>
<b>1 Introduction</b>	<b>15</b>
<b>2 Nuclear fusion and basic plasma physics</b>	<b>19</b>
2.1 Introduction to nuclear fusion . . . . .	19
2.2 Magnetic confinement fusion using tokamaks . . . . .	21
<b>3 Turbulence and geodesic acoustic modes in fusion plasmas</b>	<b>27</b>
3.1 Turbulence . . . . .	27
3.1.1 Introduction to turbulence . . . . .	27
3.1.2 Turbulence in tokamaks . . . . .	29
3.1.3 Turbulence spectra . . . . .	31
3.1.4 Energy flow and interactions . . . . .	33
3.2 Linear instabilities . . . . .	34
3.2.1 Drift waves . . . . .	34
3.2.2 Core turbulence instabilities . . . . .	35
3.3 Shear flows and turbulence suppression . . . . .	38
3.4 Zonal flows and geodesic acoustic modes . . . . .	41
3.4.1 Zonal flows . . . . .	41
3.4.2 Geodesic acoustic mode . . . . .	42
3.4.3 GAM properties and state of GAM research . . . . .	44

<b>4</b>	<b>ASDEX Upgrade tokamak</b>	<b>47</b>
4.1	Details and operation . . . . .	47
4.2	Heating systems . . . . .	50
4.3	Important diagnostics . . . . .	52
4.4	Plasma configuration . . . . .	55
<b>5</b>	<b>Doppler reflectometry</b>	<b>59</b>
5.1	Wave propagation and reflectometry . . . . .	59
5.2	ASDEX Upgrade V-band Doppler reflectometers . . . . .	67
<b>6</b>	<b>Data analysis</b>	<b>71</b>
6.1	Determining Doppler shift and amplitude . . . . .	71
6.1.1	Density profile reconstruction . . . . .	72
6.1.2	Beam tracing code TORBEAM . . . . .	73
6.1.3	Doppler shift measurements . . . . .	75
6.2	GAM detection . . . . .	77
6.3	Comparison of sliding window FFT and MUSIC techniques . . . . .	79
6.4	Cross-correlation techniques . . . . .	81
6.4.1	Spatio-temporal cross-correlation . . . . .	81
6.4.2	Two-point correlation method . . . . .	83
<b>7</b>	<b>GAM frequency scaling</b>	<b>85</b>
7.1	Description of experiments . . . . .	85
7.2	Comparison to existing models . . . . .	89
7.2.1	Comparison with Winsor's basic scaling . . . . .	90
7.2.2	Comparison with Conway's heuristic model . . . . .	91
7.2.3	Comparison with Angelino's fluid model . . . . .	94
7.2.4	Comparison with Sugama and Watanabe's gyrokinetic model . . . . .	96
7.2.5	Comparison with Gao's gyrokinetic model . . . . .	97
7.3	Further influences on the GAM frequency . . . . .	98
7.4	Discussion . . . . .	100
<b>8</b>	<b>GAM amplitude scaling</b>	<b>103</b>
8.1	GAM amplitude scaling with $\kappa_b$ and $q$ . . . . .	104
8.2	GAM drive . . . . .	107
8.3	GAM damping . . . . .	109

---

8.3.1	Collisionless damping for negligible $k_r$ . . . . .	110
8.3.2	Collisionless damping with finite orbit width effects . . . . .	111
8.3.3	Comparison of the collisionless damping rates . . . . .	112
8.3.4	Collisional damping . . . . .	113
8.4	Discussion . . . . .	115
<b>9</b>	<b>GAM structure and propagation</b> . . . . .	<b>117</b>
9.1	Description of experiments . . . . .	117
9.2	GAM structure . . . . .	119
9.2.1	Multiple eigenmode GAMs . . . . .	120
9.2.2	Continuum GAM . . . . .	122
9.2.3	Single eigenmode GAM . . . . .	126
9.2.4	Width of GAM region . . . . .	131
9.3	GAM propagation . . . . .	131
9.3.1	Cross-correlation tilt and cross-phase derivative . . . . .	132
9.3.2	Two-point correlation method . . . . .	136
9.4	Magnetic GAM signature and structure . . . . .	137
9.5	Discussion . . . . .	142
<b>10</b>	<b>Summary and conclusion</b> . . . . .	<b>145</b>
	<b>Bibliography</b> . . . . .	<b>151</b>
	<b>Acknowledgements</b> . . . . .	<b>159</b>
	<b>Curriculum Vitae</b> . . . . .	<b>161</b>
	<b>Eidesstattliche Versicherung</b> . . . . .	<b>163</b>



# List of abbreviations and symbols

$A$	amplitude of reflectometer signal
$A_D$	Doppler shift amplitude
$A_{\text{GAM}}$	GAM amplitude
ASDEX Upgrade	tokamak in Garching, Germany (Axially Sym. Divertor EXp.)
AUG	ASDEX Upgrade
$a$	(horizontal) minor plasma radius
$B$	magnetic field
$B_t$	toroidal magnetic field
$B_\theta$	poloidal magnetic field
$\mathbf{B}_0$	background magnetic field vector
$b$	vertical minor plasma radius
CLISTE	interpretive equilibrium code
CXRS	charge exchange recombination spectroscopy
$c$	vacuum light speed
$c_s$	sound velocity
D-T reaction	fusion reaction between deuterium and tritium
DIII-D	tokamak in San Diego, USA
$E$	electric field strength
$E_r$	radial electric field strength
ECE	electron cyclotron emission
ECRH	electron cyclotron resonance heating
ELM	edge-localised mode
ETG mode	electron temperature gradient mode, plasma instability
$e$	elementary charge
FFT	fast Fourier transform
$f$	frequency
$f_D$	Doppler shift frequency
$f_{\text{GAM}}$	geodesic acoustic mode frequency
$f_{Ny}$	Nyquist frequency
$f_{\text{ref}}$	reference frequency
$f_s$	sampling frequency

---

$f_{\text{scale}}$	GAM frequency as predicted by frequency scaling models
$G$	scale factor, ratio between measured $\omega_{\text{GAM}}$ and $c_s/R_0$
GAM	geodesic acoustic mode
GENE	non-linear gyrokinetic plasma turbulence code
H-mode	high confinement mode of plasma operation
$I$	in-phase reflectometer signal
$I_p$	plasma current
IQ detector	refl. component generating in-phase and quadrature signals
ICRH	ion cyclotron resonance heating
ITER	planned tokamak in Cadarache, France
ITG mode	ion temperature gradient mode, plasma instability
<b><math>J</math></b>	electrical current
JET	tokamak in Culham, UK (Joint European Torus)
$k$	wavenumber
$k_0$	wavenumber of launched microwave radiation
$k_r$	radial wavenumber
$k_{\parallel}$	wavenumber parallel to $\mathbf{B}_0$
$k_{\perp}$	wavenumber perpendicular to $\mathbf{B}_0$
$L_r$	radial turbulence correlation length
L-H transition	transition between L-mode and H-mode confinement states
L-mode	low confinement mode of plasma operation
LCFS	last closed flux surface
LSN	lower single null, standard divertor plasma configuration
MHD	magnetohydrodynamics
MUSIC	multiple signal classification method
$m$	poloidal mode number
$m_B$	Bragg backscattering order
$m_e$	electron mass
$m_i$	ion mass
$m_p$	particle mass
$N$	refractive index
NBI	neutral beam injection (for heating and current drive)
$n$	toroidal mode number
$n_e$	electron density
O-mode	ordinary mode wave polarisation
ODW	orbit drift width
$P_{XY}$	cross-correlation between two signals $x$ and $y$
$p$	plasma or fluid pressure
PSL	passive stabilising loop
$Q$	quadrature reflectometer signal
$q$	(local) safety factor
$q_p$	electric charge of a particle
$q_{95}$	safety factor at 95% of minor radius $a$

---

$R$	radial distance from machine axis
$R_0$	major plasma radius
$Re$	Reynolds number
$\mathcal{R}$	Reynolds stress
$\mathbf{R}_c$	plasma curvature radius
$r$	radial coordinate
$S$	power spectrum of a time series
$S_l$	local frequency and wavenumber spectrum
SOL	scrape-off layer
SWFFT	sliding window fast Fourier transform signal analysis method
$s_\kappa$	radial gradient of the plasma elongation
$T$	particle temperature
$T_e$	electron temperature
$T_i$	ion temperature
TCV	tokamak in Lausanne, Switzerland
TEM	trapped electron mode, plasma instability
TEXTOR	former tokamak in Jülich, Germany
TORBEAM	a beam tracing code for toroidal geometry
$t$	time
USN	upper single null, divertor plasma configuration
$u_{\parallel}$	turbulence velocity parallel to $\mathbf{B}_0$
$u_{\perp}$	turbulence velocity perpendicular to $\mathbf{B}_0$
$\mathbf{u}$	turbulence or fluid velocity
V-band	microwave frequency band from 50–75 GHz
$v_{\text{ph}}$	phase velocity
$v_r$	radial (propagation) velocity
$v_{T_i}$	ion thermal velocity
$v_{\theta}$	poloidal plasma velocity
$v_{\perp}$	particle velocity perpendicular to the magnetic field
$\mathbf{v}$	particle velocity
$\mathbf{v}_{\text{dia}}$	diamagnetic drift velocity
$\mathbf{v}_{\mathbf{E} \times \mathbf{B}}$	background plasma $\mathbf{E} \times \mathbf{B}$ velocity
$W_{\parallel}$	kinetic energy of a particle parallel to $\mathbf{B}_0$
$W_{\perp}$	kinetic energy of a particle perpendicular to $\mathbf{B}_0$
W-band	microwave frequency band from 75–110 GHz
X-mode	extraordinary mode wave polarisation
$Z$	number of protons in a nucleus
$Z_{\text{eff}}$	effective charge
ZF	zonal flow
$\beta_N$	normalised ratio between thermal and magnetic pressure
$\gamma$	damping rate
$\gamma_{\text{coll}}$	collisional damping rate
$\gamma_{\text{c.less}}$	collisionless Landau damping rate

---

$\gamma_i$	ion specific heat ratio
$\gamma_{\text{LODW}}$	collisionless damping rate in large orbit drift width limit
$\gamma_{\text{SW}}$	collisionless damping rate from Sugama-Watanabe model
$\Delta$	Shafranov shift
$\Delta'$	Shafranov shift gradient
$\Delta_{\text{GAM}}$	radial width of GAM region
$\epsilon$	inverse aspect ratio
$\epsilon_0$	vacuum permittivity
$\theta_0$	launch angle in Doppler reflectometer
$\kappa$	local plasma elongation
$\kappa_b$	boundary plasma elongation
$\lambda_r$	radial wavelength of the GAM
$\mu$	dynamic viscosity
$\nu$	kinematic viscosity
$\nu_i$	ion collisionality
$\rho$	gyro radius of a particle
$\rho_e$	electron Larmor radius
$\rho_i$	ion Larmor radius
$\rho_m$	mass density of a fluid/plasma
$\rho_s$	ion Larmor radius at electron temperature (drift scale)
$\rho_{\text{pol}}$	normalised poloidal flux radius
$\tau$	ratio between electron and ion temperature, $T_e/T_i$
$\tau_l$	time lag
$\tau_E$	energy confinement time
$\Phi$	plasma potential
$\phi$	phase of reflectometer signal
$\Psi$	poloidal magnetic flux
$\Omega$	vorticity
$\omega$	angular frequency
$\omega_0$	angular frequency of launched microwave radiation
$\omega_c$	electron cyclotron frequency
$\omega_{ci}$	ion cyclotron frequency
$\omega_D$	angular Doppler shift frequency
$\omega_{\text{GAM}}$	angular eigenfrequency of the geodesic acoustic mode
$\omega_p$	plasma frequency

# Chapter 1

## Introduction

As the world-wide energy consumption continues to rise, as fossil resources such as coal, oil or natural gas continue to dwindle, and as the excessive emission of long-lived greenhouse gases threatens to have a significant impact on the world's climate, the search for alternative energy sources has become more important than ever. Renewable energy sources, which include solar, wind and hydro-electric power, are strongly dependent on suitable weather and geographic conditions. Nuclear fission, while capable of providing large amounts of energy from comparably few resources, has disadvantages in the potentially catastrophic environmental consequences of a reactor malfunction and the still unsolved questions of the longterm storage and disposal of its radioactive waste products.

A promising alternative has emerged in the concept of a nuclear fusion reactor, which would provide energy that is released from fusion reactions between hydrogen isotopes, similar to the processes in the sun. Such a reactor would have no significant carbon footprint and would use fuel resources which are less limited than those of today's power plants. While nuclear fusion does not have radioactive by-products, it still leaves some radioactive waste, such as the steel that is used as structural material. The radioactive decay time of those waste products is orders of magnitude below fission waste. In addition, there is no danger of an unstoppable radioactive meltdown.

The most advanced among multiple approaches to designing such a fusion reactor is the tokamak, a ring-shaped chamber in which a high-temperature plasma is magnetically confined. If the particle density, temperature and energy confinement of the plasma can be raised to a sufficient level, the conditions are favourable for

fusion reactions to occur, and the energy output could be used as a power source. Due to the extremely high necessary temperatures—higher even than those in the sun—direct contact of the energetic plasma particles with the wall of the reaction chamber must be avoided.

However, transport of particles across the magnetic field lines, from within the confined plasma radially outwards in the direction of the wall, occurs. While a certain amount of radial transport was anticipated as an effect of classical diffusion and particle collisions, the actual amount of transport in fusion experiments is significantly larger. Plasma turbulence has been identified as the source of this so-called anomalous transport. Therefore, a thorough understanding of the turbulent processes in fusion plasmas, especially those which can moderate the turbulence level and thus help to improve energy confinement, is needed for the development of predictive models and the design of future fusion reactors.

One of the processes that is connected to the moderation of turbulence is the geodesic acoustic mode (GAM). It is a radially localised oscillating zonal flow, which is found near the edge of the confined plasma. A flow oscillation like the GAM can reduce the radial correlation length of the turbulence through the shearing of turbulence structures. The GAM is itself driven by the broadband turbulence and thus also serves as a sink for turbulent energy. In addition, GAM activity has been observed prior to the transition of plasmas into the so-called high-confinement regime (or H-mode), a state which is characterised by a reduced turbulence level and steeper density and temperature gradients. The improved energy confinement of the H-mode is instrumental in making fusion a reality, however the transition mechanism is still not fully understood, making the investigation of GAMs and their possible role in the transition important. GAMs, while first theoretically described in 1968, have come into the focus of experimental research in the past decade, the results of which have in turn driven new theoretical and computational research on the subject.

In order to make experimental observations of turbulence processes such as the GAM, a suitable diagnostic with sufficient temporal and spatial resolution is necessary. Additionally, it must be capable of measuring velocity fluctuations inside the high-temperature plasma, ideally without disturbing it. One such diagnostic technique that meets these requirements is Doppler reflectometry, which uses backscattered microwave radiation to measure the velocity of density fluctuations. In the past decade, Doppler reflectometry has been successfully employed at multiple fusion

experiments to measure GAMs.

This thesis presents results obtained from Doppler reflectometry measurements in experiments that were performed on the ASDEX Upgrade tokamak. To understand the role that the GAM plays in the complex interaction between plasma gradients, turbulence and flows, the moderation of turbulence through shear flows and the transition to the H-mode regime, all of which are important for the design and operation of the next generations of fusion experiments, its fundamental properties must be thoroughly researched. Therefore, this thesis focuses on the following main goals:

- *Characterising the GAM frequency scaling behaviour as a function of plasma geometry and comparing it to theoretical and empirical models (Ch. 7):*

The frequency of the geodesic acoustic mode determines the influence that the GAM can have on the plasma shearing rate and thus on the reduction of the radial correlation length of the turbulence. Building on prior results, which showed decreased GAM frequency in highly elongated plasmas, the GAM is measured in a range of different geometrical conditions. The results confirm the strong influence that plasma shaping can have on the GAM frequency, and it is found that, while some of the current models successfully predict the general trends which can be observed experimentally, the GAM frequency is subject to a wide range of influences and a comprehensive model is yet to be developed.

- *Investigating the behaviour of the GAM amplitude during variation of the plasma geometry, and relating it to collisional and collisionless GAM damping rates as predicted by multiple models (Ch. 8):*

The GAM may only play a significant role in the moderation of turbulence if its amplitude is sufficiently large to cause displacements comparable to the turbulent structure size, therefore an understanding of its scaling under different plasma conditions is needed. The GAM amplitude is shown to be impacted by variations of the plasma boundary elongation and safety factor. In a comparison of multiple models for the GAM damping rate, it is shown that for typical ASDEX Upgrade parameters both collisionless and collisional damping, the latter of which is often not considered, may play a significant role in determining the GAM amplitude.

- *Identifying the structure and radial propagation of the GAM (Ch. 9):*

In order to better understand the interaction of the GAM with the plasma turbulence, it is necessary to determine in which radial region the GAM appears, what its structure is, and how these parameters are influenced by other plasma parameters. In previous experiments, GAMs have been observed to both extend radially at a constant frequency (eigenmode), and with frequencies that vary radially (continuum). In the results presented in this thesis, three different GAM structures are identified, and transitions between these states are observed, connecting previously disparate results. Radial GAM propagation, measured with correlation Doppler reflectometry, is only observed under specific conditions, while the magnetic signature of the GAM is identified for the first time at ASDEX Upgrade.

The thesis closes with a summary of the most important findings and an outlook for future work on the subject.

# Chapter 2

## Nuclear fusion and basic plasma physics

Before the specific focus of this thesis can be addressed, it is necessary to introduce the concepts of plasma physics, nuclear fusion and magnetic confinement devices such as tokamaks. A thorough overview of these topics would of course exceed the scope of this work, but can be found, for example, in Refs. [1] and [2].

### 2.1 Introduction to nuclear fusion

While nuclear power is often associated with the process of nuclear fission, where a heavy atomic nucleus such as plutonium is split into two lighter nuclei, it is also possible to release energy via nuclear fusion, where two atoms are fused together into a heavier nucleus, as long as the initial nuclei are light enough. Nuclear fission has successfully served as an energy source for multiple decades. Once a fission reactor is started, the chained reaction sustains itself and serves as a continuous power source. One of the main disadvantages of nuclear fission is the fact that this chain reaction can be difficult to stop when necessary, leading to dangerous consequences. A further significant problem is the radioactive waste that is produced by fission reactors.

Nuclear fusion, on the other hand, has neither of these problems. In using low-mass elements in its reactions, such as hydrogen or helium, there are no long-lived radioactive atoms left behind from the fuel. A fusion reactor is also significantly easier to shut down, in fact one of the main challenges of current fusion research is

to get to the point where a reaction can sustain itself at all. That it can be done becomes apparent by looking at the sun, which provides earth with energy from the proton-proton chain reaction, where hydrogen atoms fuse into helium nuclei within several steps [3].

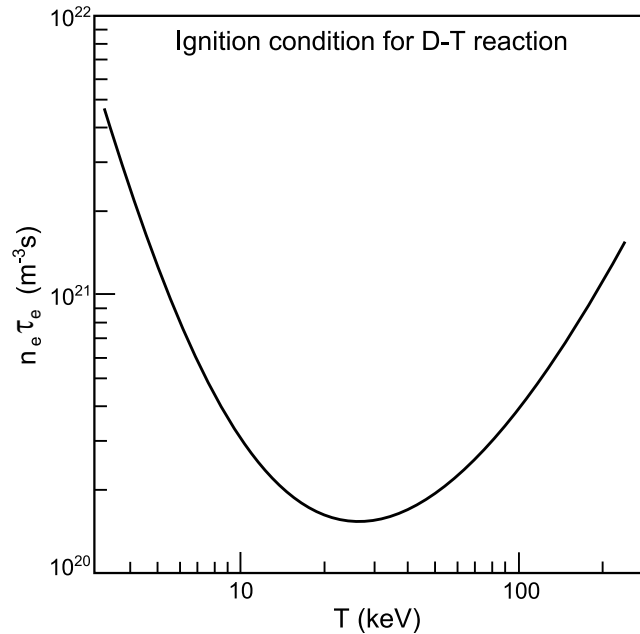
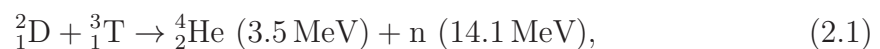


Figure 2.1: Threshold value for the product of density  $n$  and energy confinement time  $\tau_E$  as a function of temperature  $T$  which must be crossed to reach ignition in a fusion reactor, for the D-T reaction. Adapted from Ref. [4].

There are multiple possible reactions between low-mass atoms that could theoretically be used as a source for fusion energy. Most promising is the reaction between the hydrogen isotopes deuterium and tritium (the D-T reaction):



where n is an energetic neutron. The reaction rate depends on the particle temperature  $T$  and the particle number density  $n$  of the fuel (i.e. the deuterium and tritium nuclei). In order to make fusion a viable energy source, more energy needs to be released than is needed to sustain the reaction or lost to the surroundings. Figure 2.1 shows the threshold value for the product of density  $n$  and the energy confinement time  $\tau_E$ , which describes for how long energy is retained in the system, as a function of  $T$  for the D-T reaction. By exceeding this threshold, which is lower for the D-T reaction than for other suitable reaction candidates such as deuterium-deuterium or

deuterium-helium, the fusion reaction can become self-sustaining. Since  $\tau_E$  itself is partially determined by the temperature, this threshold is more often expressed in terms of the so-called triple product  $nT\tau_E$ . The necessity of exceeding this threshold is known as the Lawson criterion, which takes the following form for the D-T reaction:

$$nT\tau_E \geq 10^{21} \frac{\text{keV s}}{\text{m}^3}. \quad (2.2)$$

In the sun, nuclear fusion works because of the enormous gravitational forces on the particles. These forces create an environment of very high density and long energy confinement together with high temperatures. On Earth, the Lawson criterion needs to be achieved by a different approach.

## 2.2 Magnetic confinement fusion using tokamaks

In all approaches to nuclear fusion, the temperatures which are necessary for the reactions to take place at a sufficient rate are so high that the gas will be ionised and enters the plasma state. This plasma, which consists of energetic charged particles, needs to be contained within a limited space, in order to ensure that the necessary density and energy confinement thresholds can be surpassed. At the same time, any direct contact of a plasma at the necessary temperatures with common materials that might be used to build a kind of reaction chamber would be very destructive. Therefore, the use of strong magnetic fields to contain the plasma, known as the magnetic confinement approach to fusion, has become the largest and most promising field of research.

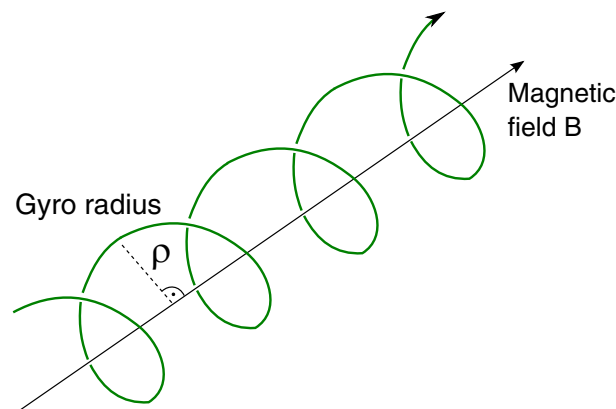


Figure 2.2: Charged particles in a magnetic field gyrate around the field line.

When a particle with charge  $q_p$  moves with velocity  $\mathbf{v}$  in a magnetic field  $\mathbf{B}$ , it becomes subject to the Lorentz force  $\mathbf{F}_L$ :

$$\mathbf{F}_L = q_p \mathbf{v} \times \mathbf{B}. \quad (2.3)$$

This force leads to a gyration around the magnetic field line, shown in Fig. 2.2, at the frequency  $\omega_c$  and a radius  $\rho$ :

$$\omega_c = \frac{q_p B}{m_p}, \quad \rho = \frac{v_\perp}{\omega_c}. \quad (2.4)$$

The gyro frequency and gyro radius are different for plasma electrons and ions, due to their dependence on particle mass  $m_p$  and charge  $q_p$ . Here,  $v_\perp$  is the particle velocity perpendicular to the magnetic field.

In the history of magnetic confinement fusion, many different designs have been proposed and tested [1]. The earliest fusion devices used a linear arrangement and the magnetic mirror effect in order to keep the plasma confined. However, due to large and unavoidable losses at the edges, it was necessary to adopt designs with closed magnetic field lines, i.e. designs that bend the field lines into a circular shape, allowing the plasma to be confined within a toroidal chamber.

In early toroidal designs the closed field lines were created exclusively by magnetic coils wrapped around the plasma, creating a toroidal field  $B_t$ . When moving away from the central axis of the torus, the strength of the magnetic field would decrease as an inverse function of the radius. Due to the gyro motion around the field lines, particles would alternate between regions of stronger and weaker magnetic field, leading to changes in the gyro radius (Eq. 2.4) and therefore a resulting drift motion that would vertically separate electrons and ions. The resulting vertical electric field  $\mathbf{E}_v$  affects the charged particles via the Coulomb force, leading in the presence of a magnetic field to the so-called  $E \times B$  drift:

$$\mathbf{v}_{E \times B} = \frac{\mathbf{E}_v \times \mathbf{B}_t}{B^2}. \quad (2.5)$$

In this case, the  $E \times B$  drift would drive all particles, independent of charge, towards the outer wall of the confinement chamber. To avoid this effect, the next iteration of toroidal designs needed to impose an additional poloidal magnetic field  $B_\theta$  on top of the toroidal field  $B_t$ , in order to introduce helically twisted field lines. This way,

electrons and ions would no longer drift apart vertically.

There are two competing approaches to the generation of the poloidal magnetic field. In the stellarator category of fusion devices, the magnetic field is completely created by external magnetic coils. Fusion devices of the tokamak category create the poloidal field by inducing a toroidal plasma current  $I_p$ . Both approaches have their disadvantages. To drive the toroidal current in tokamaks, a large solenoid in the centre of the torus is usually employed. However, the current can only be driven for a limited amount of time, leading to pulsed operation. For a stellarator, on the other hand, the coil design needs to be much more complicated. Due to the requirements for particle confinement and plasma stability, very precise calculation and manufacturing is important. Only with technical advances in the last decades has the stellarator concept become a promising alternative to the tokamak.

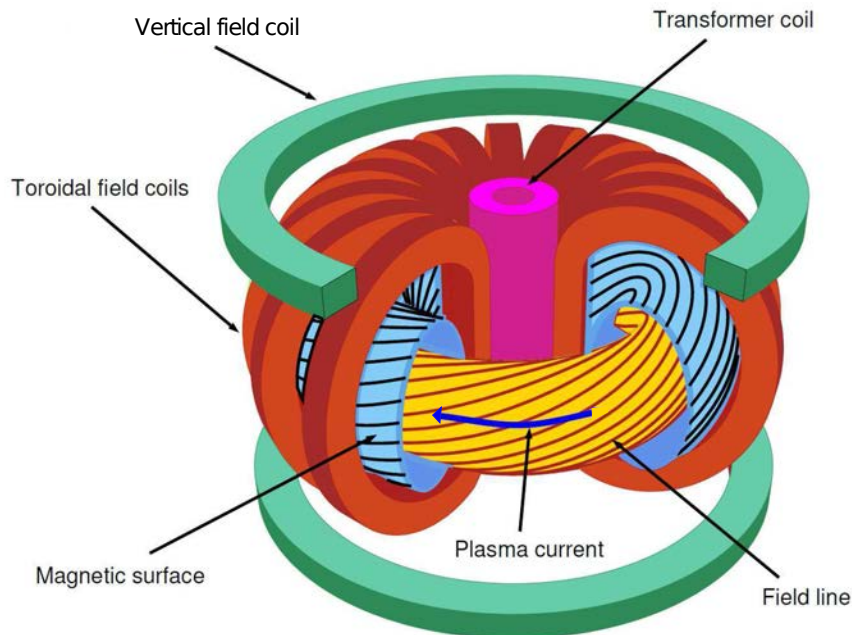


Figure 2.3: Basic layout of a tokamak: a plasma current (blue) is driven by a central solenoid (pink). Together with the toroidal (red) and vertical (green) field coils, it creates a set of nested flux surfaces with helically twisted field lines. Adapted from Ref. [5].

Figure 2.3 shows the basic layout of a tokamak, as well as its magnetic field lines. The central solenoid drives the plasma current  $I_p$ , which itself creates a poloidal magnetic field  $B_\theta$ . The ring of toroidal field coils creates the toroidal field  $B_t$ . The combination of both fields leads to the closed and helically twisted field lines, which

form a set of nested flux surfaces. The vertical field coils are necessary for further stabilisation and position control of the plasma. Chapter 4 gives a more detailed discussion of the tokamak design and operation.

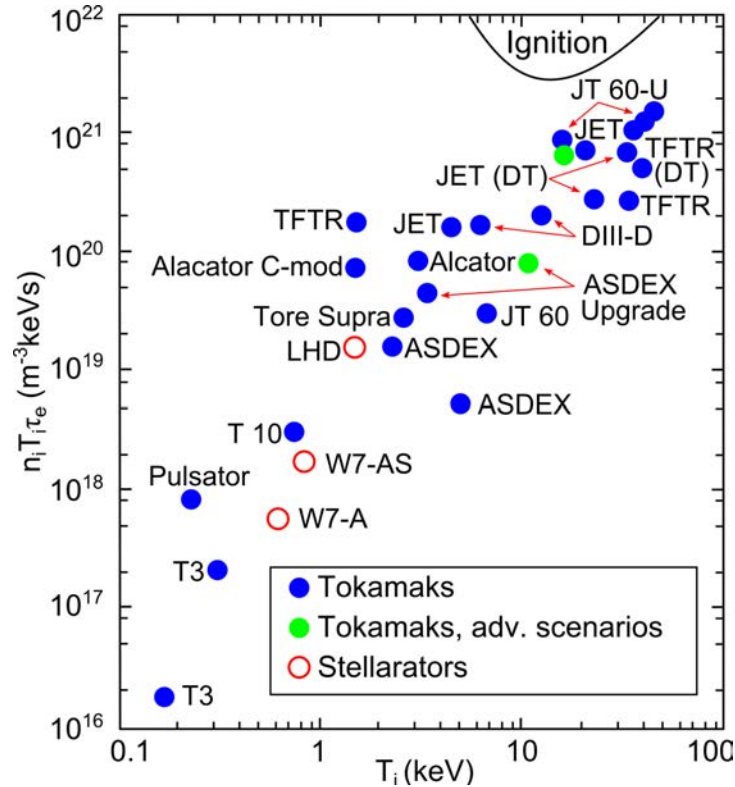


Figure 2.4: Progress of tokamaks and stellarators towards achieving the Lawson criterion. Adapted from Ref. [6].

Tokamaks have been used in fusion research since the 1950s. Over the decades, continuous progress has been made towards achieving the Lawson criterion, as shown in Fig. 2.4. From one generation of tokamak to the next, the size of the devices has continuously grown. With larger plasma radius, the ratio of stored energy (proportional to plasma volume) to energy loss (proportional to plasma surface) becomes more favourable. ASDEX Upgrade, the tokamak on which the experiments for this thesis were performed, falls into the range of medium-sized tokamaks. While it is too small to achieve breakeven, like all tokamaks currently in operation, it is valuable for studies relating to many of the remaining challenges in fusion, such as turbulent transport (see Ch. 3). Additionally, results from devices such as ASDEX Upgrade have significant influence on the design of the next generation of fusion devices. This includes the ITER project, which is currently under construction

in France, and is expected to be the first tokamak to fulfill the Lawson criterion. Nuclear fusion below the breakeven level has been achieved at JET and TFTR.

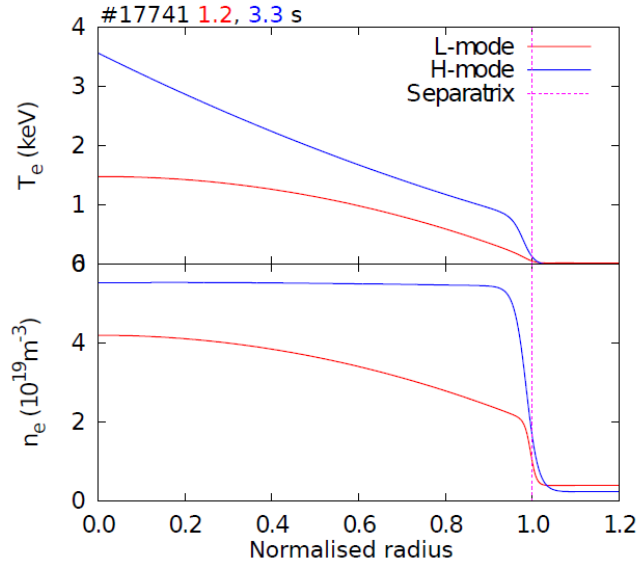


Figure 2.5: Radial profiles of plasma electron temperature  $T_e$  and density  $n_e$  in L-mode (red) and H-mode (blue) for ASDEX Upgrade discharge #17741. Reproduced from Ref. [7].

One of the most important steps towards making fusion a reality was made with the discovery of the high confinement mode (H-mode) on the ASDEX tokamak, the predecessor of ASDEX Upgrade [8]. It was discovered that the input of sufficient heating power into the plasma would, once a certain threshold value was crossed, lead to the formation of a transport barrier at the plasma edge. The larger plasma pressure gradient due to this transport barrier strongly increases temperature and density in the plasma core, and therefore the confined energy. This process is described as a transition from the regular, low confinement mode (L-mode) to the high confinement mode. Figure 2.5 shows typical radial ASDEX Upgrade profiles of the plasma electron temperature  $T_e$  and density  $n_e$  as a function of the normalised radius, before and after the L-H transition. One of the key features of the H-mode is the suppression of plasma edge turbulence. While the transition can be reliably achieved in experiments on many tokamaks, it is not yet fully understood. Next generation devices such as ITER, and any future fusion power plants, will depend on operating in H-mode in order to produce sufficient power. Therefore, it is important to develop a better and predictive physical understanding of the transition and

the edge turbulence phenomena that have been found to possibly be connected to it, such as the geodesic acoustic mode [9,10]. As discussed in the following chapter, geodesic acoustic modes are an inherent part of plasma turbulence in tokamaks, and need to be understood in detail in order to explain turbulent transport phenomena.

# Chapter 3

## Turbulence and geodesic acoustic modes in fusion plasmas

This chapter introduces the basic concepts of turbulence, with a focus on turbulence in magnetically confined fusion plasmas such as in tokamaks. Section 3.1 serves as an overview of the important turbulence properties. Section 3.2 presents some of the most important linear instabilities that lead to the development of turbulence. Shear flows and their role in turbulence suppression are the subject of Sec. 3.3. And finally, Sec. 3.4 introduces zonal flows and geodesic acoustic modes.

### 3.1 Turbulence

As outlined in the introduction to this thesis, the confinement of particles and energy within the plasma is very important in order to fulfill the Lawson criterion and make fusion a viable energy source. Turbulence is thought to be responsible for a major part of transport of particles and energy [11,12], and thus a thorough understanding of the turbulent processes is necessary.

#### 3.1.1 Introduction to turbulence

Turbulence is a phenomenon that is often encountered whenever flows of gases or fluids are involved and are subjected to external forces. A very common example of this is the turbulence that can be experienced during air travel. The transition from a laminar flow to fully developed turbulence, as shown in Fig. 3.1, is not yet completely understood.

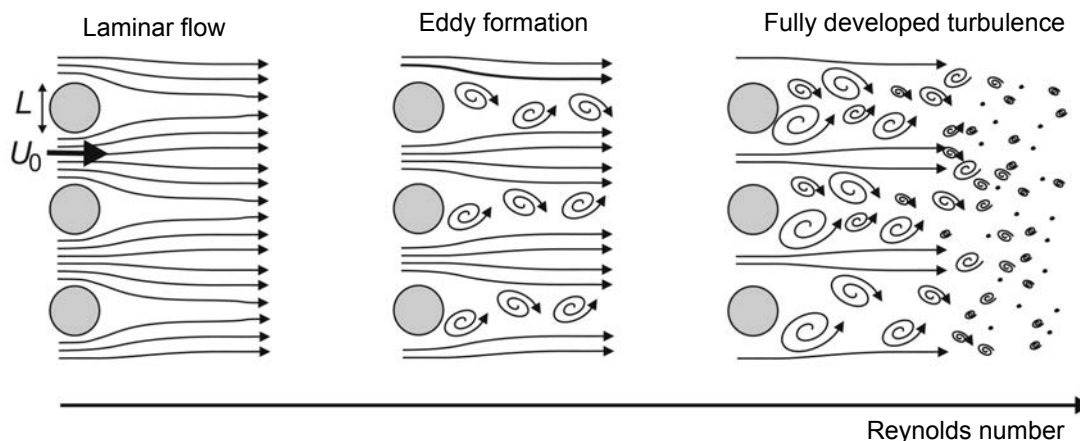


Figure 3.1: Transition of a neutral fluid from laminar flow to fully developed turbulence for increasing Reynolds number  $Re$ . Adapted from Ref. [3].

The Navier-Stokes equation is used to describe the motion of neutral incompressible fluids ( $\nabla \cdot \mathbf{u} = 0$ ) and the role of turbulence:

$$\rho_m \frac{d\mathbf{u}}{dt} = -\nabla p + \mu \Delta \mathbf{u} + \mathbf{F}. \quad (3.1)$$

The convective derivative  $d/dt = \partial/\partial t + \mathbf{u} \cdot \nabla$  of the fluid velocity  $\mathbf{u}$  for a fluid with mass density  $\rho_m$  is driven by the external forces acting on the fluid: the pressure gradient  $\nabla p$ , the friction force  $\mu \Delta \mathbf{u}$  (where  $\mu$  is the dynamic viscosity) and further forces  $\mathbf{F}$ , such as gravity. The Navier-Stokes equation is often brought into a dimensionless form through the introduction of a characteristic length scale  $L_c$ , characteristic time scale  $T_c$  and characteristic velocity  $u_0 = L_c/T_c$ . The resulting equation for dimensionless quantities (denoted by a prime), neglecting the additional forces  $\mathbf{F}$ , is the following:

$$\frac{d\mathbf{u}'}{dt'} = -\nabla' p' + \frac{1}{Re} \Delta' \mathbf{u}'. \quad (3.2)$$

$Re$  is known as the Reynolds number. It is calculated from the characteristic scales and can also be defined in terms of the kinematic viscosity  $\nu = \mu/\rho_m$ :

$$Re = \frac{\rho_m L_c^2}{\mu T_c} = \frac{L_c u_0}{\nu}. \quad (3.3)$$

It describes the degree of turbulence in the system, and is the ratio between the non-linear term responsible for the turbulence generation and the viscous force on the liquid that leads to dissipative damping. When the Reynolds number increases,

as shown in Fig. 3.1, the viscous damping lessens and the fluid transitions through vortex streets from a state of laminar flow into fully developed turbulence. The advantage of the dimensionless form of the Navier-Stokes equation is that it shows how two systems can be considered dimensionally similar if their Reynolds numbers are the same, even if the underlying characteristic scales are different.

While the underlying turbulent processes are of a random and continuously fluctuating nature, it is possible to treat turbulence with a statistical approach. The important characteristics and statistical moments of the turbulence are stationary and can be measured in experiments.

### 3.1.2 Turbulence in tokamaks

For plasma turbulence, the general observations from the previous section hold, however, the situation is more complicated than in neutral fluids. Generally, a plasma contains two fluids (electrons and ions) that can interact with each other, and electromagnetic forces can no longer be neglected.

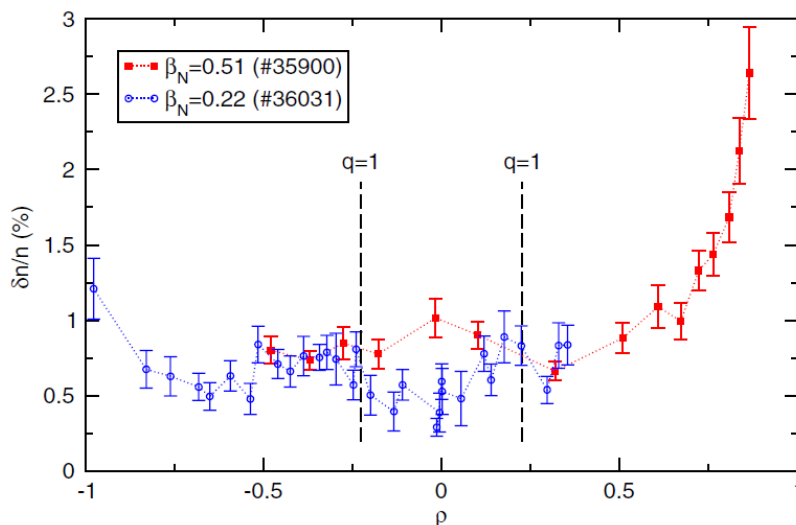


Figure 3.2: Relative density fluctuation amplitude as a function of the normalised plasma radius  $\rho$ , where negative values represent the high-field side, for two discharges from the Tore Supra tokamak with different  $\beta_N$ . From Ref. [13].

Furthermore, due to the magnetic field line geometry, a tokamak plasma usually consists of nested flux surfaces. Within each flux surfaces the particles can move freely, leading to much faster movement along the magnetic field lines than

perpendicular to them. Because of this decoupling of parallel and perpendicular processes, plasma turbulence can be considered as nearly two-dimensional, instead of the isotropic three-dimensional fluid of the previous section.

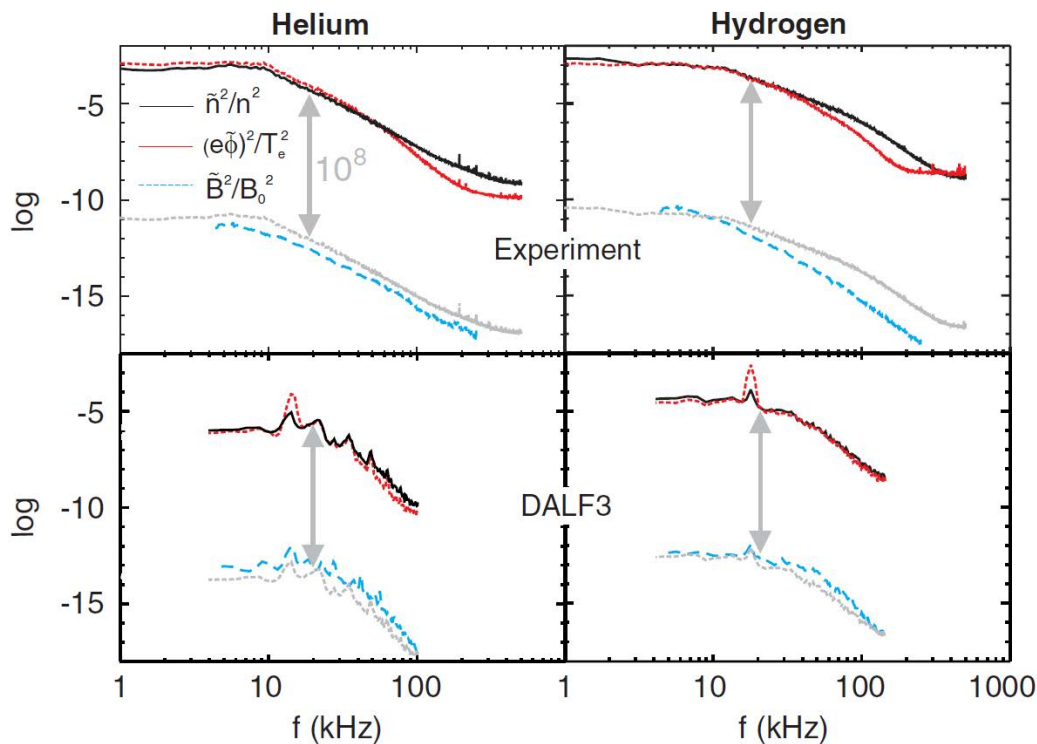


Figure 3.3: Comparison of plasma density (black) and potential (red) fluctuation power spectra against magnetic fluctuation power spectra (blue) in hydrogen and helium plasmas. Top: experimental results from the TJ-K stellarator. Bottom: numerical results from DALF3 calculations. The grey arrows mark a factor of ten orders of magnitude. From Ref. [16].

To get a full understanding of turbulent processes and the important turbulent transport, fluctuations in multiple plasma parameters need to be considered: the magnetic field  $B$ , electron and ion temperatures  $T_e$  and  $T_i$ , the plasma density  $n_e$  and the plasma potential  $\Phi$ . Both the amplitude of these fluctuations and their cross-phases can be important. The relative fluctuation level, i.e. the root mean square of a fluctuating quantity divided by its average value, describes the impact that turbulence has on a plasma quantity. Figure 3.2 shows measurements of the relative density fluctuation level  $\tilde{n}/n$  in the Tore Supra tokamak, which is shown to increase rapidly towards the plasma edge [13]. Measurements from the tokamaks TEXT, TFTR or DIII-D show values of 1% or less for  $\tilde{n}/n$  in the core and up to

10–20% in the edge [11, 14, 15].

Plasma turbulence can be separated into electromagnetic and electrostatic turbulence. In the first case, fluctuations in the plasma potential and density as well as in the magnetic field are considered. In the electrostatic case, the magnetic field is assumed to remain constant, so that turbulent  $\tilde{E} \times B$  drifts are only determined by fluctuations of the electric field (or the potential  $\Phi$ , since  $E = -\nabla\Phi$ ). Experimental results indicate that magnetic fluctuations are often comparatively small and play no important role in most fusion experiments [11, 16]. Figure 3.3 shows both experimental results from the stellarator TJ-K as well as numerical results using the drift-Alfvén turbulence code DALF3 [17], where magnetic fluctuations were found confirmed to be multiple orders of magnitude smaller than density or potential fluctuations. Therefore, the electrostatic approach is usually sufficient to describe turbulent processes.

### 3.1.3 Turbulence spectra

One approach to treating turbulence in a statistical manner is to consider the system in terms of scales. Fig. 3.1, for example, shows the formation of turbulent eddies of different sizes. In a fusion plasma, turbulence can range from very small localised structures up to large-scale flows that affect the entire plasma. Therefore, it is important to not only know how much turbulence energy is present within any scale, but also to understand how the turbulent structures evolve and how the energy is transferred between the different scales. The transfer of energy from larger scales to smaller scales, e.g. the break-up of a large eddy into many smaller eddies, is known as a direct cascade. Energy transfer in the opposite direction is called an inverse cascade. Depending on the nature of the turbulent system, the mechanisms of energy transfer between the scales can differ substantially.

A well-known theory for the description of turbulence in a three-dimensional, homogeneous and isotropic fluid was proposed by Kolmogorov [18, 19]. It assumes that a direct cascade transfers energy from the large scales to the smaller scales, which can be described in terms of an energy transfer rate. In Kolmogorov’s theory, turbulent energy is put into the system at a so-called injection scale, with wavenumber  $k_{\text{inj}}$ , and is transferred to smaller and smaller scales, as pictured in Fig. 3.4 (a). At small scales, where the viscosity plays a more important role, the energy is dissipated into heat. The wavenumber range between injection and dissipation

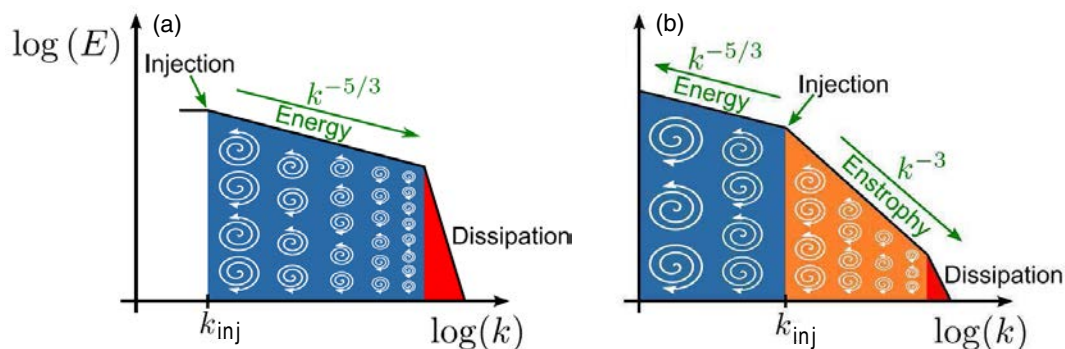


Figure 3.4: (a) Spectral energy for turbulence in a neutral three-dimensional fluid with direct energy cascade. (b) Spectral energy for turbulence in a neutral two-dimensional fluid with inverse energy and direct enstrophy cascade. Adapted from Ref. [20].

scales, where no external energy enters the system, is known as the inertial range. Kolmogorov's theory predicts that the turbulence is self-similar and that spectral energy in this range is proportional to  $k^{-5/3}$ .

As mentioned above, a magnetically confined plasma is in many important aspects a two-dimensional system, for which Kolmogorov's theory does not apply. Kraichnan [21, 22] describes the differences that are found for ideal 2D turbulence which does not allow for vorticity stretching. As pictured in Fig. 3.4 (b), there are now two cascades originating from the injection scale  $k_{\text{inj}}$ . Energy, unlike for 3D turbulence, is now transferred in an inverse cascade from the injection scale to larger scales. There is also a direct enstrophy cascade towards smaller scales and the dissipative range. Enstrophy is the mean squared vorticity and is conserved in 2D turbulence, where the vorticity is defined as  $\Omega = \nabla \times \mathbf{u}$ . This is often referred to as a dual cascade, with two inertial ranges where the energy is proportional to  $k^{-5/3}$  and  $k^{-3}$ , respectively.

For plasma turbulence, the situation is of course more complicated. Electromagnetic forces play a role, and several of the assumptions between Kolmogorov's and Kraichnan's models are violated. While it is similar to a two-dimensional system, three-dimensional effects still play a role in plasma turbulence. Furthermore, the turbulence is not necessarily self-similar. And maybe most importantly, gradients in plasma density or temperature lead to energy input into the system at a wide range of scales, instead of a distinct injection scale. Thus, some deviations from the dual cascade model are to be expected.

### 3.1.4 Energy flow and interactions

This section aims to give an overview of the various energy sources, sinks and energy transfer mechanisms that can be encountered in a magnetically confined fusion experiment, which are schematically shown in Fig. 3.5.

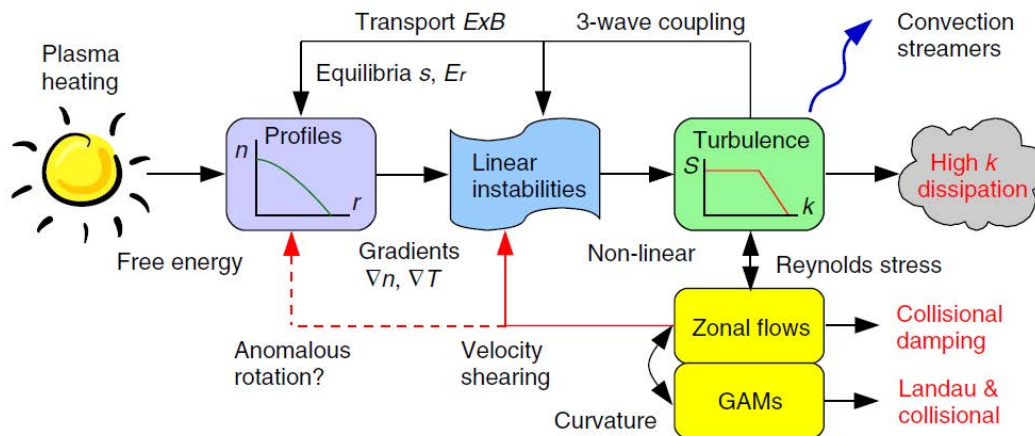


Figure 3.5: Schematic overview of the energy flow in a turbulent system. Interactions between different components of the system and dissipation mechanisms are also shown. From Ref. [23].

External energy is introduced to the system via plasma heating, which is described in more detail in Sec. 4.2. This leads to the formation of radially varying density and temperature profiles. The main source of energy input into the various linear instabilities which can occur in the system are the gradients in density, temperature and pressure. Section 3.2 will introduce the most important of these instabilities. The saturated instabilities drive broadband turbulence through non-linear coupling. As described in Sec. 3.1.3, dual cascades will lead both to viscous dissipation of energy at small scales, but also to energy transfer into larger scales such as zonal flows or geodesic acoustic modes (GAMs), which are the subject of this work. When the scales reach the order of the plasma size, they can affect both the growth rate of the linear instabilities, and the overall plasma equilibrium that is responsible for the plasma profiles and gradients. Via the Reynolds stress, the turbulence can also lead to the formation of radially localised zonal flows. Both static zonal flows and the oscillating geodesic acoustic modes are very important turbulence phenomena, as they can take energy out of the broadband turbulence, and can be dissipated through collisional and Landau damping. They can also regu-

late the turbulence through velocity shearing. A more detailed description of zonal flows and geodesic acoustic modes is given in Sec. 3.4.

## 3.2 Linear instabilities

This section describes the mechanism of drift wave turbulence, which is responsible for turbulent transport of heat and particles, as well as a number of related linear instabilities. These are exponentially growing modes as predicted by the linearised two-fluid equations. As outlined in the previous section, these modes can interact with other components of a turbulent systems, such as zonal flows.

### 3.2.1 Drift waves

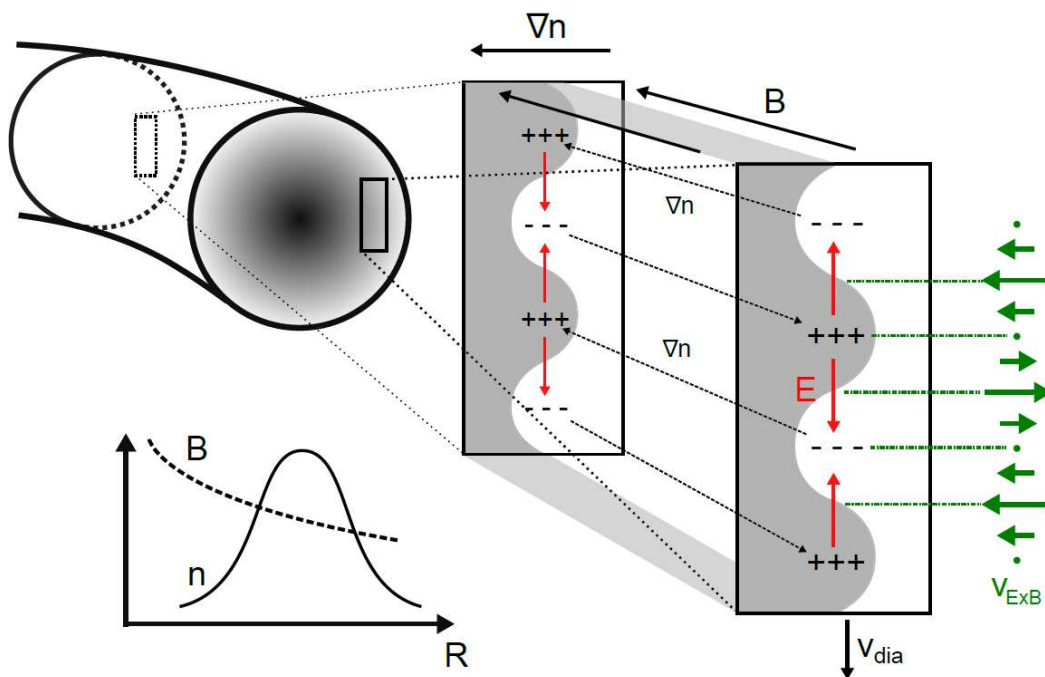


Figure 3.6: Right: Illustration of the drift wave mechanism for adiabatic electrons: a density perturbation  $\tilde{n}$  parallel to the field lines causes electrons to move along the density gradient. This results in potential and electric field perturbations that are in phase with  $\tilde{n}$ . The resulting  $E \times B$  drifts are only destabilising when density and potential fluctuations are out of phase. Top left: Sketch of the torus segment. Bottom left: radial profiles of magnetic field strength and plasma density. The density is peaked in the plasma centre while the magnetic field decreases with the major radius. Modeled after Ref. [24].

The drift wave instability is an important three-dimensional phenomenon. Fig. 3.6 depicts the situation in a toroidal plasma. Shown is a slab of plasma that is separated into a region of higher density and a region of lower density, marked by colour. This is a simplified model of a typical density profile, which is peaked in the centre and gradually decreases towards the edge. A periodic density fluctuation  $\tilde{n}$  perturbs the plasma, not only perpendicular to the field lines but also in the parallel direction (albeit on a longer scale:  $k_{\perp} \gg k_{\parallel} > 0$ ). This creates a parallel density gradient along the field lines, which leads to particle motion in order to restore the equilibrium state. Because of their lower mass, the electrons will move toward the low-density region much faster than the ions. This results in a negatively charged region of low density, as well as a positive region of higher density that is left behind in the wake of the electrons, i.e. a perturbation of the plasma potential. An electric field is created between neighbouring regions of positive and negative charge, resulting in  $\tilde{E} \times B$  drifts. The phase difference between the density and potential fluctuations determines whether this leads to an instability or not. In the ideal case of adiabatic electrons, the response is instantaneous and the phase difference is zero. The drift velocities point in opposite directions at every knot of the fluctuation, so the density perturbation will merely move in the direction of the electron diamagnetic drift [3]. In realistic experimental conditions, plasma resistivity and other factors will lead to a non-adiabatic electron response. This introduces a finite phase difference between density and potential fluctuations that can cause the drift wave to grow and become unstable.

### 3.2.2 Core turbulence instabilities

While the drift wave is driven by strong density gradients in the edge, turbulence further towards the plasma core is more often influenced by the temperature gradients. The ion temperature gradient mode (ITG mode) is an instability that is believed to be a contributor to turbulent transport [25, 26]. It is illustrated in Fig. 3.7.

The ITG mode can be compared to the Rayleigh-Taylor instability, which is encountered in neutral fluids with a heavy fluid layer on top of a lighter fluid. In the case of a plasma, these layers are replaced by higher and lower ion temperature regions. The ion (and electron) pressure profile in a tokamak is typically peaked in the centre and decreases gradually towards the edge. In the plasma core, temperature gradients are usually stronger than density gradients. Due to the curvature and

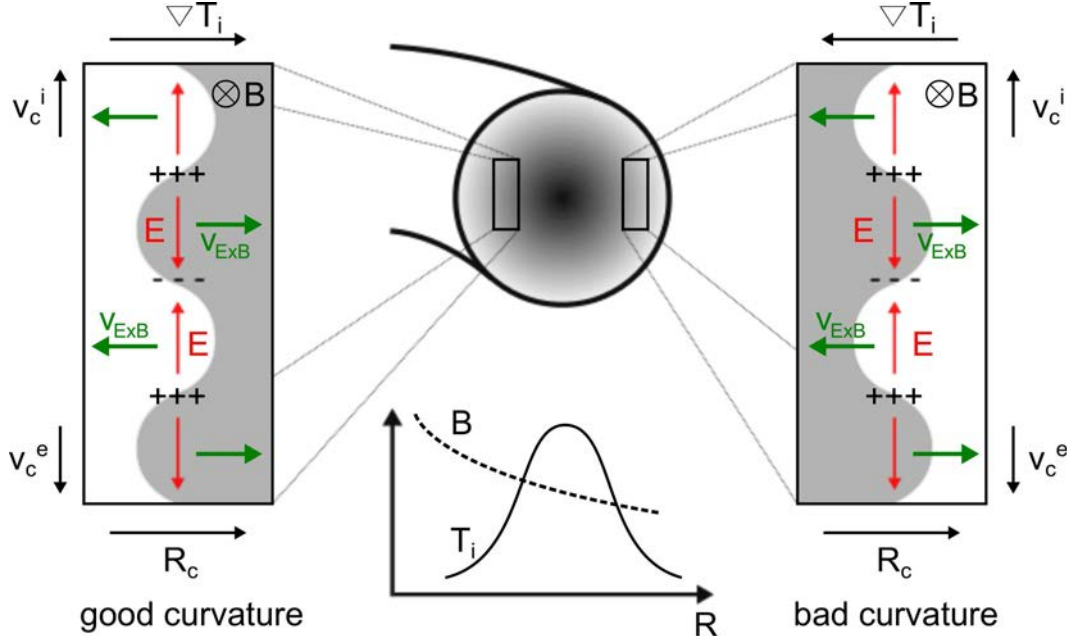


Figure 3.7: Illustration of the ITG instability: an ion temperature perturbation  $\tilde{T}_i$  causes the local curvature drift velocity of ions to change. This results in density and potential perturbations causing radial  $E \times B$  drifts. On the tokamak high-field side (left) these drifts are oriented in the opposite direction from the initial temperature perturbation and stabilise the plasma, however on the tokamak low-field side (right) the perturbation grows further. The overall mode is unstable once a certain critical gradient is exceeded.

$\nabla B$  drifts, ions and electrons move in opposite directions (particle charge  $q_p = \pm e$ ), normally along lines of equal pressure (i.e. temperature, if the density is assumed to be locally constant) [3]:

$$\mathbf{v}_{C,\nabla B} = (2W_{\parallel} + W_{\perp}) \frac{\mathbf{R}_c \times \mathbf{B}}{q_p R_c^2 B^2}. \quad (3.4)$$

Here,  $\mathbf{R}_c$  is the plasma curvature radius,  $W_{\parallel}$  and  $W_{\perp}$  are the kinetic particle energies in parallel and perpendicular directions. In the presence of a  $T_i$  perturbation the drift velocity depends on kinetic energy, and ions from the high-temperature regions drift faster than those from the low-temperature regions. Therefore, positive charge will accumulate above the hotter regions, and negative charge above colder regions. This perturbation of the plasma potential creates an electric field and an  $\tilde{E} \times B$  drift in the radial direction. Depending on the position within the plasma, this can have a stabilising or a destabilising effect. On the inside of the torus, the curvature vector

and the  $T_i$  gradient point in the same direction, which leads to drifts pushing the high-temperature plasma back towards the centre and the low-temperature plasma towards the edge, so that the perturbation is dampened. Therefore, this region is said to have good curvature. On the outside of the torus, the opposite effect appears: the  $E \times B$  drifts amplify the temperature perturbations because  $\mathbf{R}_c$  and  $\nabla T_i$  are opposed. This is known as bad curvature. In a toroidal device with helical field lines, particles will traverse regions of both good and bad curvature, leading to alternating amplification and dampening of such perturbations.

The ITG mode rotates at low velocity in the ion diamagnetic drift direction, which is also indicated in Fig. 3.7. It exhibits the so-called critical gradient behaviour, i.e. the mode is overall stable as long as the normalised ion temperature gradient  $R|\nabla T_i|/T_i$  is below a critical value. Only if that value is exceeded the ITG becomes unstable. The typical scale length for ITG modes falls in the range of  $k_\perp \rho_i < 1$ , i.e. the wavelength is larger than the ion Larmor radius  $\rho_i = \sqrt{m_i T_i}/(q_p B)$ . Experimental turbulence measurements indicate that fluctuations at these scales are responsible for the majority of turbulent transport.

A second, very similar type of turbulence is the electron temperature gradient mode (ETG mode) [27]. The basic principle is the same as for the ITG mode, except that it is the electron behaviour that is important. Again, a critical gradient has to be exceeded for the ETG mode to become unstable. The rotation of the ETG mode is in the electron diamagnetic direction, i.e. opposite to the ITG mode (although in some cases these directions can reverse and the modes are difficult to tell apart). ETG modes are related to fluctuations at much smaller scales,  $k_\perp \rho_e \approx 1$ , or  $k_\perp \rho_i \gg 1$ . Some studies have argued that ETG modes can significantly contribute to electron heat transport [28,29], however they were found to give only small transport contributions in ASDEX Upgrade L-mode discharges [30].

A third linear instability that appears in toroidal plasmas is the trapped electron mode (TEM mode) [31, 32]. Particles can be magnetically trapped on the plasma low-field side in a tokamak. These particles exhibit toroidal precession, which can have a destabilising effect on density or electron temperature fluctuations. TEM modes appear at intermediate scales, i.e.  $k_\perp \rho_s \approx 1$ , with  $\rho_s = \sqrt{m_i T_e}/(eB)$ . They usually propagate in the electron diamagnetic direction. ITG and TEM turbulence often occur simultaneously and cannot be completely separated [33]. However, there are instances in which one mode is stable while the other is unstable.

Other instabilities, such as kinetic ballooning modes or microtearing modes have

also been studied and found to play a role under specific circumstances. Generally, ITG and TEM modes are easier to observe experimentally than ETG modes. This is because of their lower perpendicular wavenumber ranges, which are easier to access for many diagnostics. Measurements of ETG turbulence require high precision, as the overall turbulence level for high  $k$  is much lower (cf. Fig. 3.4).

As introduced in Sec. 3.1.4, these instabilities are both related to the drive of large-scale zonal flows, and can in turn be regulated by them via velocity shearing [34–36]. It is important to note that any experimental measurement in a plasma will only capture a steady state, in which the growth of these instabilities and their dissipation are already in balance.

### 3.3 Shear flows and turbulence suppression

Now that some of the important turbulent instabilities have been introduced, it is important to understand the mechanisms by which turbulence can be suppressed, and thus plasma confinement can be increased.

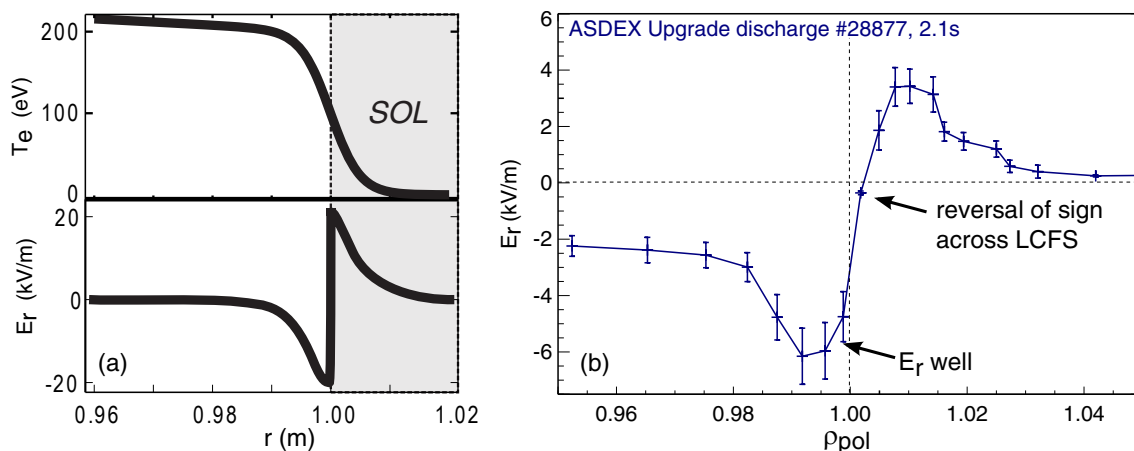


Figure 3.8: (a) Illustration of plasma temperature and radial electric field profiles in the edge of tokamak plasmas, with sudden reversal of  $E_r$  across the last closed flux surface, from Ref. [37]. (b) Radial profile of  $E_r$  in ASDEX Upgrade L-mode discharge #28877 at 2.1 s, measured using Doppler reflectometry, showing the expected  $E_r$  well and the strong  $E_r$  shear region.

It is believed that radially sheared plasma velocity, due to  $E \times B$  flows driven by a sheared radial electric field  $E'_r = \partial E_r / \partial r$ , is an important contributor to non-linear stabilisation and the suppression of turbulence. The radial electric field in the

edge region of tokamak plasmas shows strong variation, as shown in Fig. 3.8. Inside of the last closed flux surface (see Sec. 4.4),  $E_r$  is negative and determined by the radial pressure gradient  $\partial p/\partial r$ :

$$E_r^{\text{edge}} \approx \frac{1}{en} \frac{\partial p}{\partial r}. \quad (3.5)$$

In the scrape-off layer (SOL) outside of the last closed flux surface, parallel currents to the divertor target plates affect the radial electric field so that it changes sign and is determined by the plasma potential gradient, which is proportional to the temperature gradient [37]:

$$E_r^{\text{SOL}} = -\frac{\partial \Phi}{\partial r} \propto -\frac{\partial T_e}{\partial r}. \quad (3.6)$$

The region of strongly negative radial electric field around the  $E_r$  minimum is known as the  $E_r$  well. Strong  $E_r$  shear is found on both sides of the well, in particular at the last closed flux surface where the sign of the field reverses.

The so-called shear decorrelation mechanism, which describes how  $E_r$  shear can suppress turbulence, was proposed by Biglari, Diamond and Terry [38], and features the following criterion (known as the BDT criterion):

$$\left| \frac{E_r'}{B_t} \right| > \frac{\Delta \omega_t}{k_\perp L_r}. \quad (3.7)$$

Here,  $B_t$  is the toroidal magnetic field,  $\Delta \omega_t$  the turbulence decorrelation frequency and  $L_r$  the radial turbulence correlation length. For large  $E_r$  shear (independent of its sign), but also for large turbulent structures, the shear decorrelation will play an important role. Experimental measurements and simulations in plasmas and two-dimensional fluids confirm this model [39–41].

Figure 3.9 illustrates the mechanism with the example of a single turbulent eddy. In the first figure there is no velocity shear, the turbulent eddy is simply moved in the direction of the plasma background velocity  $u_y$ . The second figure shows an intermediate state, in which the radial electric field (and therefore the plasma velocity) is weakly sheared. This leads to tilting and stretching of the turbulent eddy, however, not to a change in its radial correlation length  $L_r$ . This illustrates the case in which  $E_r$  shear is present, but the BDT criterion is not yet fulfilled, and the eddy would decay before it could be stretched further. The last figure shows a

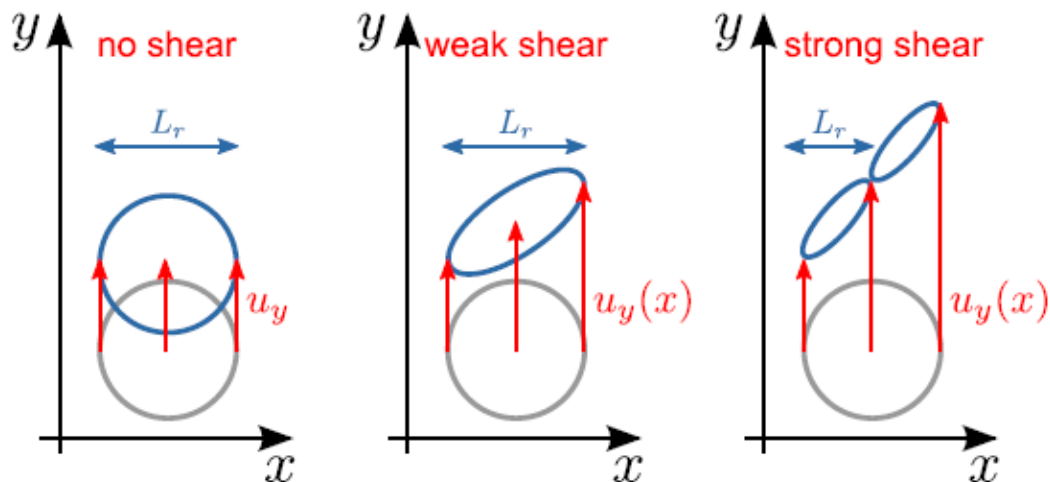


Figure 3.9: Schematic illustration of the turbulence decorrelation mechanism. Left: no velocity shear, eddy is not affected. Centre: weak shear, eddy is tilted and stretched, correlation length  $L_r$  remains constant. Right: strong shear, the eddy breaks into two eddies with smaller  $L_r$ . From Ref. [20].

case of strong velocity shear where the BDT criterion is initially fulfilled and the single large turbulent eddy is torn apart into two smaller eddies. While the shear remains at the same strength afterwards, the turbulence correlation length has been decreased enough so that  $|E'_r/B_t|$  is again below the threshold of  $\Delta\omega_t/(k_\perp L_r)$ .

The magnetic shear across the decorrelation region must also be taken into account. In combination with the velocity shear it can play a stabilising role by preventing the coupling of unstable modes that could otherwise develop. Magnetic shear also plays a role in determining the critical gradient values for the core instabilities that were introduced above. Experiments with regions of zero velocity shear and reversed magnetic shear have shown decreased electron turbulence, i.e. suppression of TEM and ETG modes [42–44].

The radial electric field and its shear have been proposed as instrumental in the transition of plasmas from low- to high-confinement regimes (L-H transition). On top of the static background shear flows, oscillations in the radial electric field and the related zonal flows and geodesic acoustic modes have been the subject of much recent investigation.

## 3.4 Zonal flows and geodesic acoustic modes

As outlined in the previous section, shear flows can regulate turbulence and thus impact plasma confinement. The name zonal flows (ZFs) is used to describe large scale shear flows that are both driven by the turbulence, but can also suppress it. They are homogeneous on flux surfaces and have approximately zero mean frequency. A related phenomenon are oscillating zonal flows which are known as geodesic acoustic modes (GAMs). Zonal flows and particularly GAMs are the main focus of this thesis.

### 3.4.1 Zonal flows

Zonal flows are toroidally and poloidally symmetrical shear flows (i.e. their toroidal and poloidal mode numbers are  $m = n = 0$ ). ZFs cannot be driven by the free energy from density or temperature gradients, and thus can also not contribute to radial transport [45]. This makes them particularly relevant for improved plasma confinement. While ZFs are homogeneous on the entire flux surface, they are strongly radially localised, i.e.  $k_r \neq 0$ . Figure 3.10 serves as an illustration.

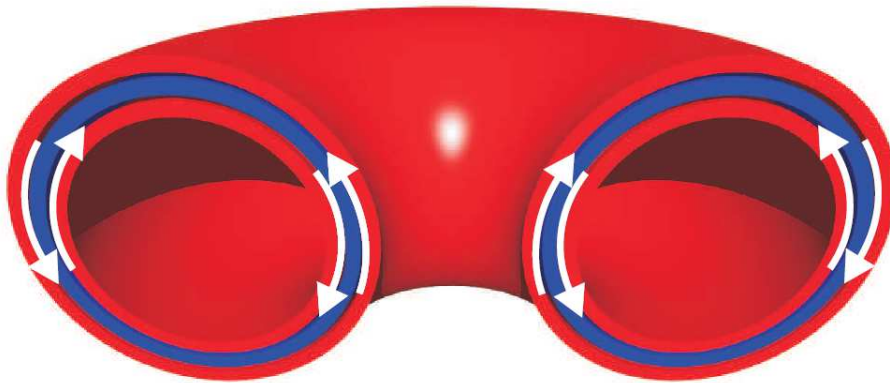


Figure 3.10: Illustration of the zonal flow mechanism: homogeneous potential perturbations on neighbouring flux surfaces (marked by red and blue) create a potential gradient, leading to a poloidal  $E \times B$  flow (white arrows). From Ref. [46].

Section 3.1.3 introduced the concept of the dual cascade for plasma turbulence. Energy is non-linearly driven from turbulence at the smaller scales towards the larger scales. Thus, zonal flows take their energy from the small-scale turbulent instabilities that were introduced in Sec. 3.2. A simple picture for the energy transfer can be obtained by considering a small eddy next to a shear flow. The flow will tilt and

stretch the eddy, thus decreasing its rotational velocity because of the conservation of its circulation (assuming an incompressible fluid). Additionally, the stretching of the rotating eddy parallel to the shear flow strengthens the flow itself [47].

This picture can be expressed mathematically in terms of the Reynolds stress  $\mathcal{R} = \langle \tilde{v}_r \tilde{v}_\theta \rangle$ , which is the temporally averaged product of poloidal and radial velocity fluctuations:

$$\frac{\partial}{\partial t} \langle v_\theta \rangle = - \left\langle \frac{\partial}{\partial r} (\tilde{v}_r \tilde{v}_\theta) \right\rangle. \quad (3.8)$$

This relation follows from the momentum balance equation of incompressible fluids [48]. Tilted eddies in a sheared velocity field lead to a strong radial derivative of the Reynolds stress, which in turn drives the zonal flow velocity  $v_\theta$ .

It is important to note that the turbulence and the ZFs are part of a self-regulated system. While the ZFs decorrelate the turbulence, they are also driven by it. This leads to a predator-prey system, in which the turbulence amplitude and shear velocity of the ZF can alternately rise and fall in a limit cycle oscillation. The level of the turbulent amplitude is ultimately determined by the ZF damping rate [45]. A side-effect of ZFs is the so-called Dimits shift [49], which increases the critical gradient above which instabilities, like ITG modes, become unstable (see Sec. 3.2).

### 3.4.2 Geodesic acoustic mode

The geodesic acoustic mode (GAM), first described by Winsor *et al.* in 1968 [50], is an oscillating zonal flow. It oscillates with a frequency that is proportional to the sound velocity  $c_s$  divided by the major radius  $R$  of the tokamak. For GAMs in the edge region of a medium-sized tokamak like ASDEX Upgrade (see Ch. 4), this usually leads to frequencies of the order of 10–20 kHz.

Like the stationary zonal flow, the potential perturbation of the geodesic acoustic mode (which leads to perturbations in the electric field via  $E = -\nabla\Phi$ ) has an axisymmetric  $m = n = 0$  structure. The density component of the GAM has the toroidal mode number  $n = 0$ , however the poloidal mode number is  $m = 1$ .

This can be understood by considering the physical mechanism of the GAM: an electric field perturbation  $\tilde{E}$  causes a perpendicular flow perturbation  $\tilde{\mathbf{u}}_\perp = (\tilde{\mathbf{E}} \times \mathbf{B})/B^2$ . Due to the fact that the magnetic field is not constant on a flux surface, but depends on the major radius  $R$ , this causes a density accumulation  $\tilde{n} \propto -\nabla \cdot \tilde{\mathbf{u}}_\perp$ . The density perturbation causes a radial current  $\tilde{\mathbf{J}} \propto (\mathbf{B} \times \nabla \tilde{n})/B^2$

which moves charge radially to counteract (and reverse) the initial  $\tilde{E}$ , leading to an oscillation at the GAM frequency.

Winsor *et al.* [50] derived the GAM from an ideal magnetohydrodynamic (MHD) model. It assumes that the GAM is electrostatic and causes small periodic perturbations of the form  $x(t) = x_0 + \tilde{x}(t)$ , with  $\tilde{x}(t) \propto \exp(-i\omega t)$ , where  $x$  stands for the mass density  $\rho_m$ , plasma velocity  $\mathbf{u}$ , plasma current  $\mathbf{J}$ , pressure  $p$  and plasma potential  $\Phi$ . A general wavelike equation (here for  $\rho_m$ ) is then derived from the linearised MHD equations:

$$\omega^2 \int |\tilde{\rho}_m|^2 J dS = \frac{\gamma p_0}{\rho_{m,0}} \left[ \frac{\left| \int \tilde{\rho}_m \frac{\mathbf{B}_0 \times \nabla \Psi \cdot \nabla B_0^2}{B_0^4} J dS \right|^2}{\int \frac{|\nabla \Psi|^2}{B_0^2} J dS} + \int \frac{|\mathbf{B}_0 \cdot \nabla \tilde{\rho}_m|^2}{B_0^2} J dS \right]. \quad (3.9)$$

$\Psi$  is the poloidal magnetic flux which represents a radial coordinate that labels the nested magnetic surfaces.  $J$  is the Jacobian of the chosen coordinate system,  $dS = d\xi d\zeta$  is the surface element of a flux surface with constant  $\Psi$ . The first term in the bracket is associated with the geodesic curvature of the flux surface. In a system where the magnetic field strength is constant over the flux surface, this term vanishes and only the second term, which represents sound wave propagation along the field lines, remains. The squared GAM frequency  $\omega^2$  in this equation is real and positive, so the mode is stable. However, non-ideal effects could lead to the excitation of instabilities at the GAM frequency.

By introducing a simple model for the magnetic field as a function of radius and safety factor  $q$  (see Sec. 4.4) and using the assumption of large aspect ratio (i.e.  $R_0 \gg a$ ), a Fourier expansion of Eq. 3.9 can be used to derive the GAM frequency:

$$\omega_{\text{GAM}} = \frac{c_s}{R_0} \sqrt{2 + \frac{1}{q^2}}. \quad (3.10)$$

$c_s = \sqrt{(T_e + \gamma_i T_i)/m_i}$  is the sound velocity,  $m_i$  is the ion mass of the plasma and  $\gamma_i$  the ion specific heat ratio (typically of the order of 1). This prediction for  $\omega_{\text{GAM}}$  neglects a number of geometrical and kinetic factors that should have an impact on GAM properties. A much more detailed discussion and investigation of these factors can be found in Ch. 7.

Further shortcomings of Winsor's model are the lack of any electromagnetic

components and its description of the GAM as a continuum function with varying frequency on each flux surface, depending on plasma temperature and safety factor. It does not describe the radial structure of the GAM or its possible propagation. Experimental measurements of radial structure and propagation will be studied in detail in Ch. 9.

### 3.4.3 GAM properties and state of GAM research

This section is intended to give a compact overview of the different areas of GAM research in magnetic confinement devices, along with some of the basic GAM properties. GAMs have been observed experimentally, studied in numerical simulations and have been the focus of theoretical research. While the opposite situation is usually the case, in GAM research experimental results have often been the driving force for subsequent numerical and theoretical investigations.

A number of reviews have been published on turbulence, zonal flow physics and GAMs [23, 34, 45, 51–54]. GAMs have been detected in almost all fusion devices that have investigated them. Experimental measurements of GAMs have been made with a wide variety of plasma diagnostics (cf. Ch. 4.3). This includes Langmuir probes ( $\tilde{\Phi}$ ) [55, 56], heavy ion beam probes ( $\tilde{\Phi}$ ) [57, 58], beam emission spectroscopy ( $\tilde{\nu}$ ) [59], Doppler reflectometry ( $\tilde{\nu}$ ) [60, 61], correlation reflectometry ( $\tilde{\nu}$ ) [62, 63] and correlation electron cyclotron emission ( $\tilde{T}_e$ ) [64] systems.

To confirm that modes detected near the characteristic frequency  $\omega_{\text{GAM}}$  from Eq. 3.10 are in fact geodesic acoustic modes, the axisymmetry has been studied on a number of devices [58, 59, 63]. Confirmations were found for both the expected  $m = n = 0$  structure of the potential fluctuations [55], as well as the asymmetric  $m = 1$  density fluctuations [62]. Recent studies at TCV have also confirmed the magnetic component of the GAM as an  $n = 0$  and  $m = 2$  structure [64].

The GAM frequency scaling has been the subject of a number studies. Figure 3.11 shows a comparison of experimentally measured GAM frequencies from multiple devices to the simple  $\omega_{\text{GAM}} \approx c_s/R_0$  prediction from Winsor, neglecting the influence of the safety factor  $q$  [51]. Results from ASDEX Upgrade showed that safety factor  $q$ , and especially plasma elongation  $\kappa$  in plasma devices with a divertor geometry, may play a significant role in determining the GAM frequency [60, 65]. This observation was confirmed by measurements on other devices [66–69]. Theoretical efforts have tried to predict the influence of other geometric influences (such

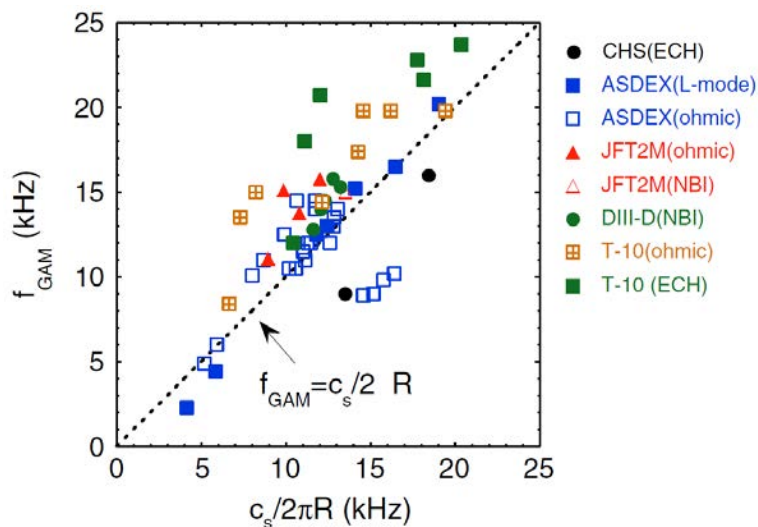


Figure 3.11: Multi-device comparison of measured GAM frequency to theoretical prediction  $f_{\text{GAM}} = c_s/(2\pi R)$ . From Ref. [51].

as inverse aspect ratio  $\epsilon$  or Shafranov shift gradient  $\Delta'$ ) [70–73], plasma impurity content [74], pressure anisotropy [75] or toroidal rotation [76, 77]. An ASDEX Upgrade study comparing some of these GAM frequency scaling models to Doppler measurements was first published in Ref. [78], and is found in more detail in Ch. 7 of this thesis.

The steady-state GAM amplitude has also been studied on multiple devices [66, 69, 79]. It is determined by the balance between the non-linear drive from the gradient-driven turbulence or from zonal flows coupling to the pressure sideband, damping due to collisional and collisionless processes and the energy transfer between various scales. Drive and damping of the GAM are thought to be responsible for the conditions in which GAMs are observed. In general, the GAM is only seen in the edge region of tokamaks, where  $E_r$  shear is strong and the safety factor  $q$  is relatively high. In the core, where  $q$  is lower, large collisionless Landau damping (which is proportional to  $\exp(-q^2)$ ) suppresses the GAM. Experiments at ASDEX Upgrade [79] and DIII-D [66] have confirmed scaling of the GAM amplitude depending on  $q$  and plasma elongation, but also on plasma configuration (e.g. limiter or divertor). GAMs have to date not been observed anywhere after the transition from L- to H-mode. The decreased background turbulence level in the plasma edge during H-mode discharges is likely to be too low to drive the GAM. There are also no observations of GAMs in the scrape-off layer, since they can only exist on closed

flux surfaces. A thorough investigation of drive and damping of GAMs, based on recent ASDEX Upgrade experiments [78], is found in Ch. 8.

The GAM has often been shown to exhibit an eigenmode-like structure, with a nearly constant frequency over several centimetres in the radial direction [58, 64, 65] (unlike the GAM continuum predicted by Winsor's fluid model). A simple approach to describe the GAM as an eigenmode with a finite radial width was proposed by Itoh *et al.* [80]. Multiple GAMs may co-exist, leading to a step-like variation of the GAM frequency. Split peaks, i.e. two neighbouring GAMs of different eigenfrequencies co-existing at the same radial positions, have also been observed [63, 65, 81]. However, the radial precision of the diagnostics must be taken into account, as insufficient resolution may lead to the simultaneous measurement of neighbouring GAMs which then appear to occur at the same radial location. Transition from this eigenmode structure to a continuum GAM have been observed in TCV during an increase of the safety factor [82], and in DIII-D after going from L-mode to an Ohmic regime [81]. Radial propagation of the GAM has been observed on multiple devices, both in radially outward and inward directions [56, 64, 83, 84], which may also contribute to split peak measurements.

The GAM has been observed to exhibit intermittent behaviour, i.e. burst-like modulation of the amplitude [60, 63]. Simultaneous measurements of the broadband turbulence level indicate that this modulation is related to interactions between the GAM and the broadband turbulence or the stationary zonal flow. Interactions between GAM and turbulence have subsequently been studied on multiple devices using bicoherence analysis [61, 84, 85], as well as between multiple co-existing GAMs [83].

Observations from ASDEX Upgrade have indicated that flow shearing due to GAMs is involved in a limit-cycle oscillation with the turbulence level prior to the L-H transition [9, 10]. Experimental results from other devices, however, have shown that the GAM decreases before the L-H transition [86, 87], or only occurs in some specific transitions [88]. Future research is necessary to understand the nature of its role in the transition [89].

# Chapter 4

## ASDEX Upgrade tokamak

The experimental work for this thesis has been performed on the ASDEX Upgrade (AUG) tokamak. This chapter introduces the device and gives an overview of the machine parameters and operation, the AUG heating systems and a sample of diagnostics important for this thesis, as well as different plasma configurations and plasma shaping.

### 4.1 Details and operation

ASDEX Upgrade is a medium-sized tokamak, operated by the Max Planck Institute for Plasma Physics (IPP) in Garching near Munich. It is named after its predecessor ASDEX (Axially Symmetric Divertor EXperiment), and has been in operation since 1991 [90]. Its design is similar to that of ITER, but with a smaller major and minor radius of 1.65 m and 0.5 m, respectively. Table 4.1 gives an overview of the technical parameters of AUG as well as its operational space. Figure 4.1 shows a poloidal cross-section of the tokamak, i.e. a vertical cut through one side of the ring-shaped vessel, along with typical flux surfaces of a plasma in divertor configuration. This configuration is produced by a set of magnetic coils, and introduces a point of zero poloidal magnetic field, the so-called X-point, typically below the bulk plasma. The last closed flux surface, called the separatrix in the divertor configuration, has no direct connection to the vessel walls, but connects to a special target surface (the divertor) which is distant from the plasma core. This way, particles that are transported radially across the separatrix do not interact with the vessel walls close to the plasma, and the level of plasma impurities can be strongly reduced.

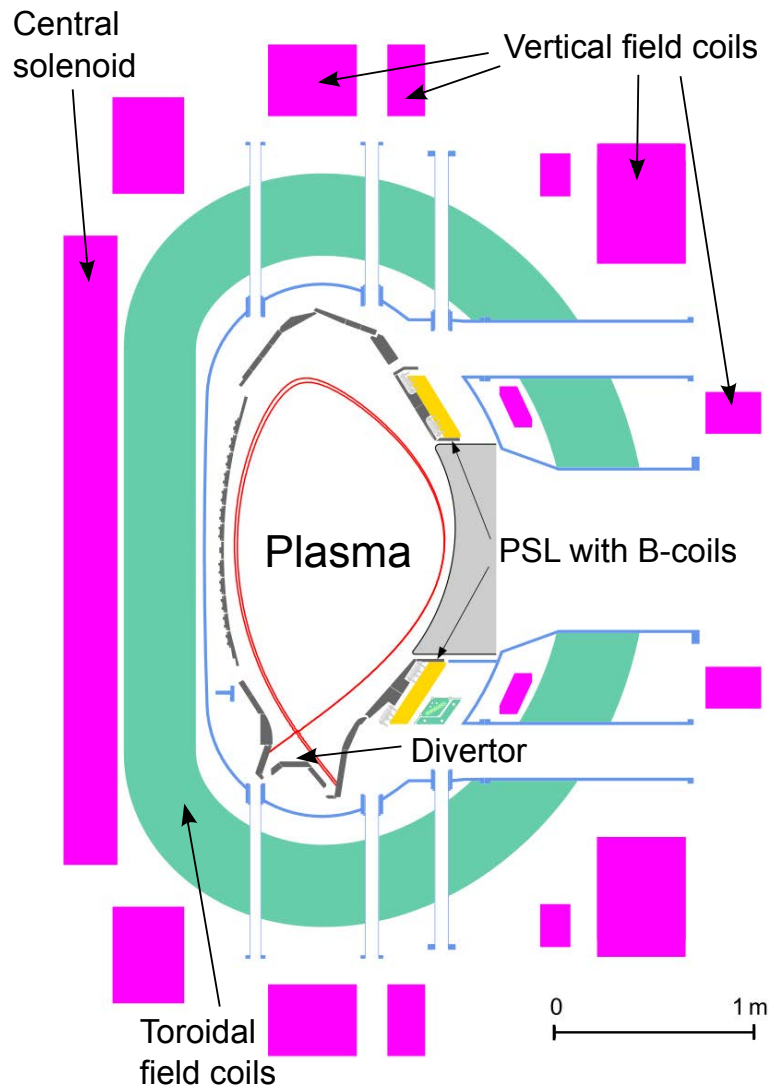


Figure 4.1: Poloidal cross-section of the ASDEX Upgrade tokamak. Shown are the structure of the vacuum chamber and the divertor, a typical plasma shape in X-point geometry, access ports and a number of magnetic field coils. These include the central solenoid, vertical and toroidal field coils, as well as magnetic perturbation coils (B-coils).

Total height	9 m
Total radius	5 m
Weight	800 t
First wall material	Tungsten
Max. magnetic field	3.1 T
Plasma current	0.4–1.6 MA
Max. pulse length	10 s
Time between pulses	15–20 min
Ohmic heating	1 MW
NBI heating power	max. 20 MW (with D)
ICRH power	max. 7.2 MW (30–40 MHz)
ECRH power	4 MW (105 or 140 GHz)
Major radius	1.65 m
Minor radius	0.5 m
Plasma volume	14 m <sup>3</sup>
Plasma surface	42 m <sup>3</sup>
Vert. elongation	1.6–1.8
Triangularity	< 0.5
Plasma gas	D, H, He
Core $n_e$	1–12 × 10 <sup>19</sup> m <sup>-3</sup>
Core $n_e$ with pellets	up to 16 × 10 <sup>19</sup> m <sup>-3</sup>
Core temperature	5–20 keV

Table 4.1: ASDEX Upgrade parameters and operational space

For ASDEX Upgrade, this is of particular importance because the machine uses tungsten as wall material. While tungsten offers high thermal shock resistance and low rates of sputtering and erosion, it also has much stronger radiation losses than other potential wall materials such as beryllium or carbon fiber composites. ASDEX Upgrade has used full-tungsten tiles for its first wall since 2007 [91,92], the divertor plates were changed from tungsten-coated carbon tiles to full-tungsten tiles in 2014 [93]. Impurities created near the divertor target surfaces, which are impacted by high particle and heat fluxes, can be effectively reduced by turbomolecular pumps and cryopumps before reentering the plasma. To off-set this loss of particles, the plasma needs to be refueled by one of several methods. A gas fuelling system uses a set of valves to inject deuterium, hydrogen or helium gas into the vessel, while

a pellet injection system shoots solid pellets of frozen deuterium into the plasma centre [94]. The latter system allows AUG to reach high core plasma density.

Figure 4.1 also shows the set of field coils which are used to create the AUG magnetic field and plasma shape. The central solenoid is used to break down the plasma by inducing a toroidal electric field and to drive the toroidal plasma current  $I_p$ . The toroidal magnetic field is created by a set of D-shaped coils outside the vacuum vessel. The vertical and radial plasma position, as well as the plasma shape, are controlled by another set of magnetic field coils, allowing for a wide range of configurations (see Sec. 4.4). The divertor configuration is generated by a set of poloidal field coils. Additionally, multiple saddle coils were installed inside the AUG vessel at various toroidal positions, in order to generate non-axisymmetric magnetic perturbations. These have been shown to be beneficial for the suppression of edge-localised modes (ELMs) [95].

AUG can be operated in L-mode and H-mode. Since GAMs are only observed in L-mode discharges or during the transition from L- to H-mode, no data from H-mode discharges will be presented in this work. The current research topics at ASDEX Upgrade cover a wide range and include turbulence studies, divertor studies and ITER scenario development among many others.

## 4.2 Heating systems

Plasma heating is necessary to reach fusion-relevant temperatures, and to compensate for plasma heat losses. The plasma is Ohmically heated by the current running through it. However, as the electron temperature  $T_e$  increases, the plasma resistivity decreases proportional to  $T_e^{-3/2}$ , thus limiting the effectiveness of Ohmic heating. Therefore, three different external heating systems are in operation at AUG, with an overall heating power of up to 30 MW. Figure 4.2 presents a top-down view of the machine and its 16 sectors, along with the location of the various heating systems.

External heating systems use either the injection of high-energy particle beams, or the absorption of electromagnetic radiation to transfer energy to the plasma. The neutral beam injection (NBI) system at AUG uses energetic neutral deuterium or hydrogen atoms to heat the plasma, which are not affected by the magnetic field. They are ionised through charge exchange in the plasma, creating a population of fast ions. These fast ions transfer both energy and toroidal momentum to the

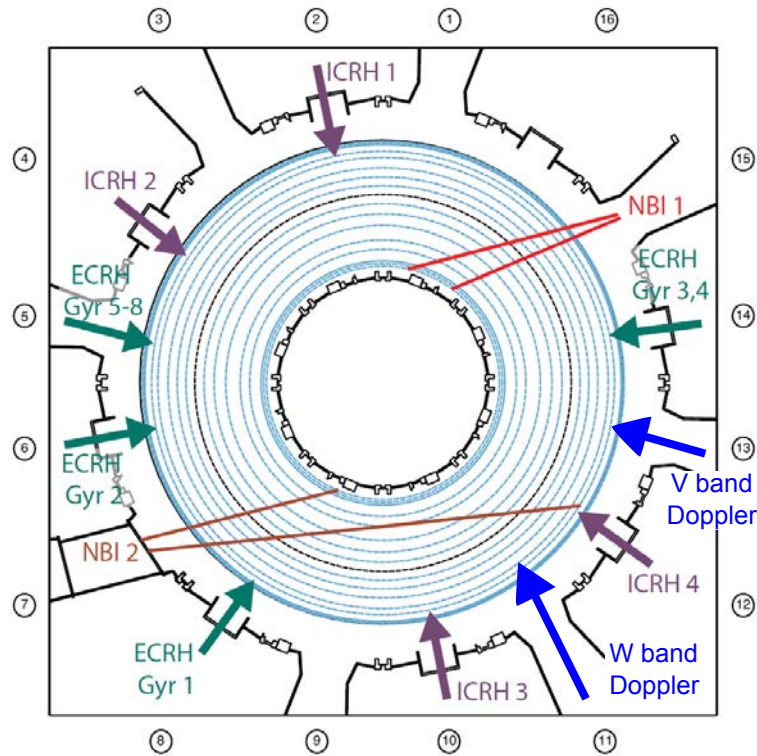


Figure 4.2: Location of heating systems (NBI, ECRH and ICRH) in ASDEX Upgrade, shown from top view. Also pictured are the locations of the V-band (Sector 13) and W-band (Sector 11) Doppler reflectometers. Adapted from Ref. [96].

thermal ions, thus driving toroidal rotation [97]. To create the neutral beam, ionised deuterium is first accelerated and then neutralised in a gas cell, leftover ions are deflected before entering the plasma. The ASDEX Upgrade NBI system consists of two injectors, called NBI 1 and NBI 2 [98]. Both injectors have four ion sources and can provide up to 10 MW of heating power each in deuterium. The ion sources are directed either radially, tangentially or can be used for off-axis toroidal current drive.

The electron cyclotron resonance heating (ECRH) system uses electromagnetic microwaves to heat the plasma. While the electric field of these waves can be used to accelerate plasma ions and electrons, the more efficient heating mechanism is resonant absorption. The location of absorption for waves of a given frequency is determined by plasma density, magnetic field and wave polarisation. More details on this can be found in Sec. 5.1 or in Ref. [99]. ASDEX Upgrade has multiple ECRH systems, the location of which can be seen in Fig. 4.2 [100]. ECRH 1 was the

first system, consisting of four gyrotrons capable of delivering 140 GHz radiation for a duration of up to 2 s and 400 kW power each. Since the 2016 experimental campaign, it is no longer in operation and has been supplanted by the second system, ECRH 2, also consisting of four gyrotrons. There are two fixed-frequency gyrotrons, and two gyrotrons which can be tuned between 105 and 140 GHz radiation. Each gyrotron can emit radiation at a power of up to 1.0 MW and for a duration of up to 10 seconds. These frequencies correspond to the second harmonic of the electron cyclotron frequency for typical magnetic field strengths of 2.0 and 2.5 T. Movable mirrors can be used for vertical and toroidal shifting of the power deposition location. A benefit of ECR heating of the core plasma is the suppressive effect that it has on the accumulation of tungsten impurities [101]. A third ECRH system with similar technical specifications to ECRH 2 is expected to replace ECRH 1 within the next years.

A similar approach to ECRH is ion cyclotron resonance heating, or ICRH. It uses electromagnetic waves at a much lower frequency (30–120 MHz). There are four ICRH antenna systems on AUG, launching from inside the vacuum vessel with a power of up to 2 MW each, for a maximum power of 7.2 MW [102].

### 4.3 Important diagnostics

This section is intended to give an overview over some of the main AUG diagnostics, many of which provide necessary data for the analyses presented in this thesis. Plasma diagnostics are of great importance for the operation of a fusion experiment. They not only enable researchers to understand the physical processes within the plasma, but they are also indispensable for the control of various plasma parameters. Due to the necessary fusion conditions, e.g. extremely high temperatures, direct physical access to the plasma core region is all but impossible for diagnostics. However, many other methods of diagnosing the plasma have been developed and reliably used.

ASDEX Upgrade is an extremely well-diagnosed tokamak, with a large number of diagnostics providing detailed measurements of many of the important plasma parameters, such as electron density, electron and ion temperatures, magnetic field strength, plasma rotation, fast particle population, impurity densities, and many more. A full range of radial profiles are available for many of these quantities.

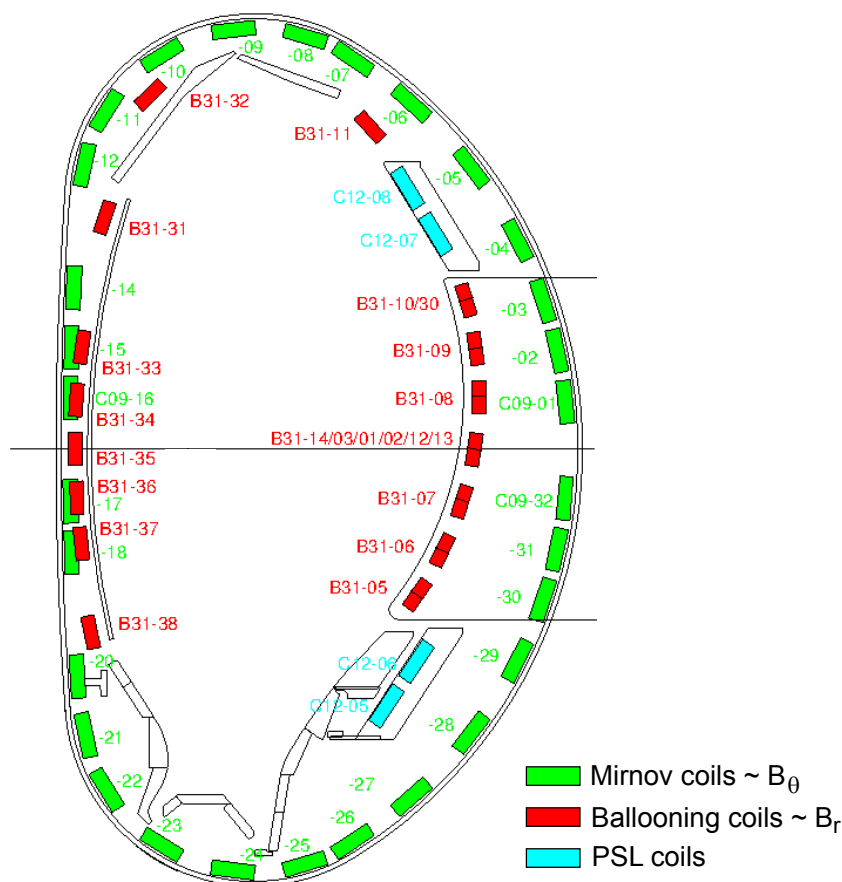


Figure 4.3: Location of Mirnov coils in ASDEX Upgrade, shown in a poloidal cross-section. Green: a poloidal ring of Mirnov coils measuring  $B_\theta$ . Red: a set of Mirnov coils measuring  $B_r$ . Blue: a set of coils located on the passive stabilising loop (PSL).

Plasma diagnostics can be divided into passive diagnostics, which depend on emissions from the plasma, and active diagnostics which probe the plasma with electromagnetic waves, lasers or particle beams. For any active diagnostic, the effect of the diagnostic technique on the plasma itself must be considered. Passive diagnostics at AUG include among others:

- Electron cyclotron emission (ECE): this system uses the radiation which is emitted from plasma electrons that gyrate around the magnetic field lines at harmonics of the electron cyclotron frequency. The electron temperature  $T_e$  can be calculated from the intensity of the ECE radiation. Since the ECE frequency depends on the magnetic field strength  $B$ , which varies radially as  $B(R) \propto 1/R$ , the ECE diagnostic can be used to calculate a radial  $T_e$  profile. AUG also has a two-dimensional ECE-imaging system in operation [103].

- Mirnov coils: changes in the magnetic field within the plasma, due to magnetic fluctuations, will induce a current in a conductor loop within the vessel, leading to a measurable voltage  $V \propto \partial B / \partial t$ . The amplitude of this voltage measures how quick the magnetic field changes. AUG has a large number of magnetic coils capable of measuring changes in the poloidal and radial magnetic field at various toroidal and poloidal locations. Figure 4.3 shows, among others, one poloidal ring consisting of 30 Mirnov coils measuring the poloidal magnetic field.

Active diagnostics allow the study of a wide range of AUG parameters:

- Charge exchange recombination spectroscopy (CXRS): the CXRS diagnostic can be used to measure the ion temperature  $T_i$ , plasma rotation and impurity density of low- $Z$  ions. The main problem for these ions is the fact that they are fully ionised in a hot fusion plasma, and will not emit any characteristic radiation. By injecting a neutral H or D beam, any ionised impurities in the plasma can gain an electron through charge exchange and hence there will be emission of light.  $T_i$  can be calculated from the Doppler broadening of the impurity line radiation. The plasma rotation will Doppler shift the entire spectrum, and the impurity density can be determined from the intensity of the radiation. At AUG, a suite of charge exchange systems exist for measurements in both the plasma edge and core [104].
- Thomson scattering: this diagnostic uses high power pulsed laser beams. The laser beams are scattered in the plasma, mainly from interactions with electrons, and the scattered radiation spectrum can be used to determine both the electron temperature and the density.  $T_e$  is related to the Doppler broadening of the laser line, similar to the determination of  $T_i$  from CXRS, while the density  $n_e$  is proportional to the intensity of the scattered radiation. High power and short pulses are necessary to provide reliable separation of signal from background noise. At AUG, two multichannel Thomson scattering systems using Nd-YAG lasers are in operation, with one system measuring in the plasma core and the other at the plasma edge [105].
- Interferometry: using the fact that a laser beam (of correct polarisation) which travels through a plasma will experience a phase shift depending on the electron density, interferometry is another way of calculating radial density pro-

files. There are two such multichannel systems at AUG, one using a deuterium cyanide laser, the other using a CO<sub>2</sub> and helium neon laser [106,107]. For each line of sight, the phase of the signal which is detected after passing through the plasma once is compared to a reference and is used to calculate a line-integrated density  $\bar{n}_e$ . Radial density profiles can be determined by deconvolution, i.e. Abel inversion.

- Lithium beam impact excitation spectroscopy: this diagnostic injects neutral lithium ions into the plasma. The radiation that is emitted from excitation due to collisions with plasma particles can be used to determine the electron density. Since the lithium beam is strongly attenuated as  $n_e$  increases, this diagnostic can typically only be used to provide  $n_e$  profiles in the plasma edge and scrape-off layer. The AUG lithium beam system measures the electron density close to the midplane and is equipped with a second optical head that provides CXRS measurements from interactions between the lithium beam and low- $Z$  impurities at the edge [108,109].

Another important diagnostic for edge density measurements in AUG is the multichannel profile microwave reflectometer, for more details see Sec. 5.1. It is one among many turbulence diagnostics which are currently available at ASDEX Upgrade. These include the multichannel Doppler reflectometry systems, which are the main diagnostic used for experiments in this work, a poloidal correlation reflectometer, the correlation ECE and  $n_e - T$  cross-phase systems, Langmuir probes for edge and scrape-off layer measurements. The lithium beam diagnostic is also used for turbulence studies. New diagnostics, such as a phased-array antenna system are under development.

## 4.4 Plasma configuration

The design of a tokamak in general, and ASDEX Upgrade in particular, allows for a range of distinct plasma configurations in which it can be operated. By varying the current through the various vertical field coils, seen in Fig. 4.1, the plasma position can be changed vertically or radially. Divertor configurations with an X-point, as introduced above, can be created, and the shape of the plasma can be influenced. The standard configuration for AUG plasmas is the lower single null (LSN) configuration. In this configuration, the plasma consists of a set of nested

elliptical flux surfaces, in which the magnetic field lines lie and on each of which plasma quantities such as the density or temperature are constant. These nested flux surfaces are centred around the so-called magnetic axis and enclosed by the separatrix. This is the last closed flux surface (LCFS), which has an X-point (i.e. a point of zero poloidal magnetic field) at the bottom. The region outside the separatrix is called the scrape-off layer (SOL). The field line geometry on a given flux surface is described by the safety factor  $q$ :

$$q = \frac{m}{n} \approx \frac{rB_t}{RB_\theta}. \quad (4.1)$$

Here,  $m$  and  $n$  describe the number of toroidal and poloidal turns that a field line takes before it is closed.  $r$  and  $R$  are minor and major radius, respectively, and the indices  $t$  and  $\theta$  refer to the toroidal and poloidal components of the magnetic field. The safety factor goes to infinity as the separatrix is approached, and is not defined in the scrape-off layer. Due to this, the edge safety factor  $q_{95}$  at 95% of the minor radius is often used to characterise the plasma. Since many plasma quantities are constant on flux surfaces, it is common to use the normalised poloidal flux radius  $\rho_{\text{pol}}$  instead of an absolute radial coordinate when creating spatial profiles. It is defined as

$$\rho_{\text{pol}} = \sqrt{\frac{\Psi - \Psi_{\text{ax}}}{\Psi_{\text{sep}} - \Psi_{\text{ax}}}}. \quad (4.2)$$

with the enclosed poloidal magnetic flux  $\Psi$ , the magnetic flux at the axis  $\Psi_{\text{ax}}$  and the magnetic flow at the separatrix  $\Psi_{\text{sep}}$ . Via this definition,  $\rho_{\text{pol}}$  goes from zero at the magnetic axis to one at the separatrix.

In addition to the typical LSN configuration, ASDEX Upgrade plasmas can also have two X-points at the top and bottom (double null configuration), or just one X-point at the top (upper single null or USN). By changing coil currents during a discharge, the plasma shape can even change from one of these configurations to the other. Similarly, ASDEX Upgrade can be operated in the limiter configuration, which consists only of nested flux surfaces without an X-point. In this configuration, excess particles and energy will not be transported to the divertor, but impact on the vessel walls instead, making it only suitable for low power L-mode studies without large energy losses. All of these configurations are shown in Fig. 4.4. Modified limiter and divertor configurations were used to study the geometry dependence of geodesic acoustic mode properties for this thesis.

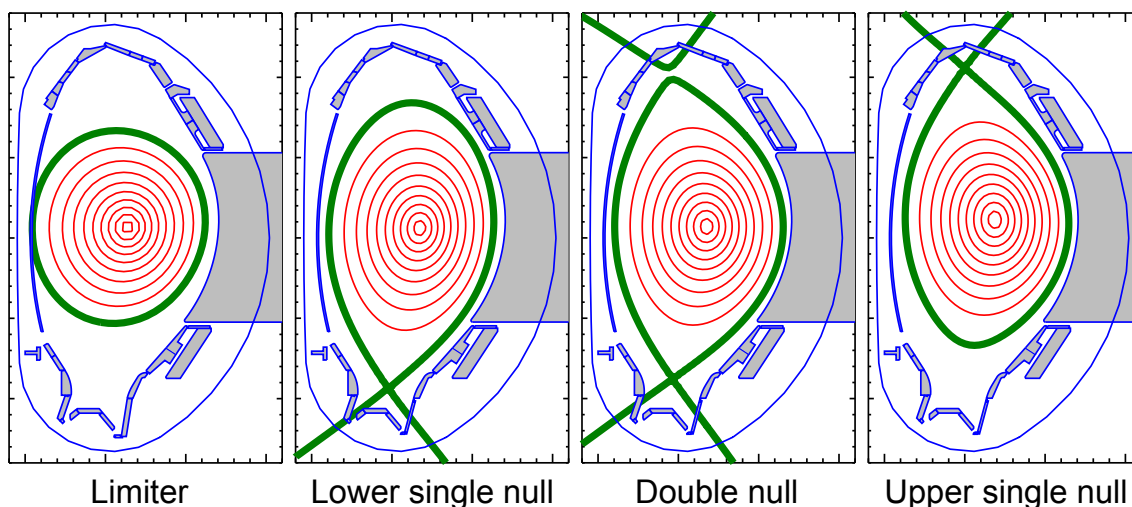


Figure 4.4: Overview of the available plasma configurations in ASDEX Upgrade. From left to right: limiter, lower single null (LSN), double null and upper single null (USN). The last closed flux surface or separatrix is shown in green.

The shape of the plasma (or any flux surface within the plasma) can be characterised by a number of geometrical quantities, in addition to the safety factor  $q$ . The elongation  $\kappa$  describes the ratio between the vertical and horizontal minor plasma radii  $b$  and  $a$ . While the local  $\kappa$  is a function of the radius (or rather,  $\rho_{\text{pol}}$ ), the boundary elongation  $\kappa_b$  at the LCFS is often used to characterise the plasma shape. Another factor beyond the elongation is the plasma triangularity  $\delta$ . Due to the possibly asymmetric shape, a lower triangularity  $\delta_l$  and an upper triangularity  $\delta_u$  can be defined:

$$\delta_{l,u} = \frac{R_{\text{out}} + R_{\text{in}} - 2R_{u,l}}{2a}. \quad (4.3)$$

The different major radii  $R$  in this formula mark the flux surface positions furthest towards the machine top ( $R_u$ ), bottom ( $R_l$ ), centre ( $R_{\text{in}}$ ) and away from the centre ( $R_{\text{out}}$ ). The ratio  $\epsilon = r/R$  is known as the inverse aspect ratio. The radial distance of the centre of a flux surface with minor radius  $r$  from the centre of the innermost flux surface is known as the Shafranov shift  $\Delta(r)$ . Figure 4.5 shows profiles of some of these quantities for an example AUG discharge, mapped to  $\rho_{\text{pol}}$ .

Another way in which the plasma configuration can be influenced at ASDEX Upgrade is by choosing the magnetic field line helicity. The direction of the current through the central solenoid determines the direction of the induced plasma current  $I_p$ , and hence of the poloidal magnetic field  $B_\theta$ . Similarly, the direction of the

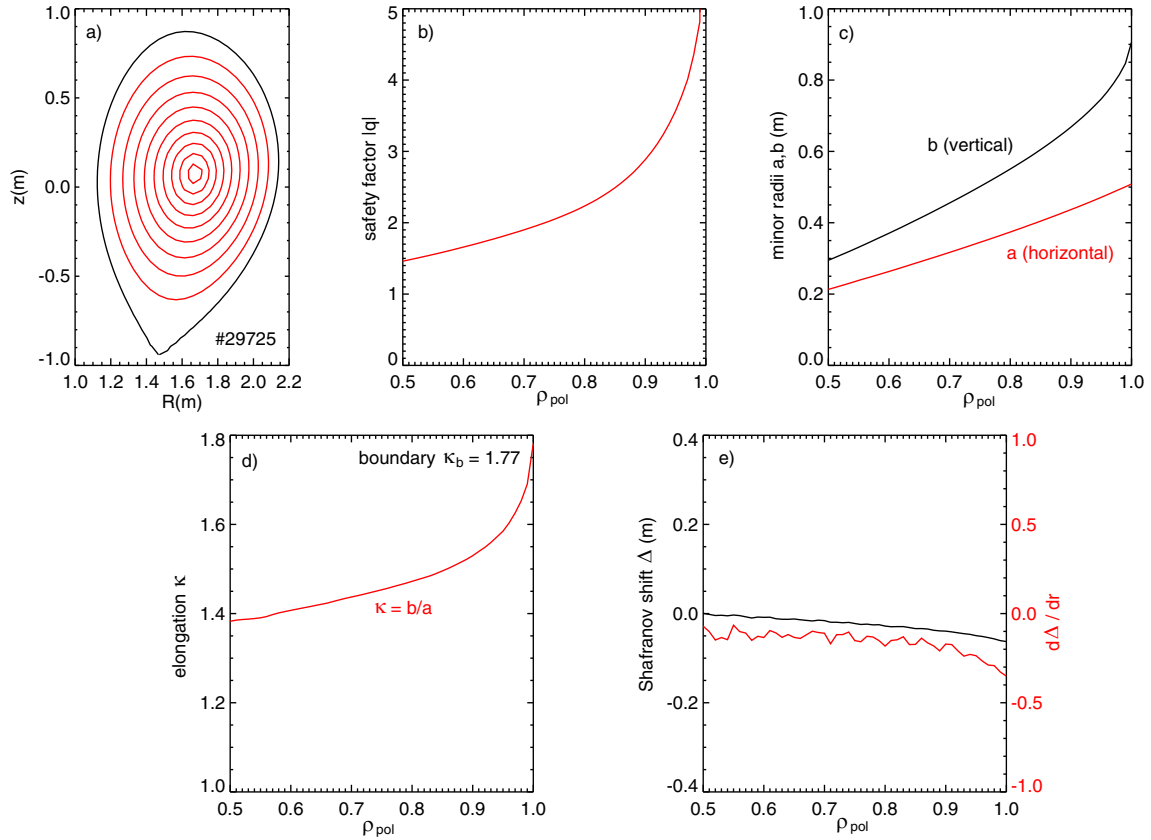


Figure 4.5: Radial profiles of characteristic plasma shape parameters from ASDEX Upgrade discharge #29725. a) Poloidal cross-section of discharge in LSN configuration. b) Safety factor  $q$ . c) horizontal and vertical minor radii  $a$  and  $b$ . d) elongation  $\kappa = b/a$ , with  $\kappa_b = 1.77$ . e) Shafranov shift  $\Delta$  and gradient  $\Delta' = d\Delta/dr$ .

toroidal magnetic field  $B_t$  can be chosen. The preferred configuration at ASDEX Upgrade uses positive  $I_p$  (i.e. counter-clockwise if viewed from above) and negative  $B_t$ , leading to left-hand helicity of the magnetic field. In this configuration, the field lines at the lower divertor have a small angle of incidence, which spreads the particle and heat flux to a wider area, and the neutral beam injection is mainly directed in the direction of the current, which yields advantages for plasma heating.

# Chapter 5

## Doppler reflectometry

This chapter introduces the Doppler reflectometry technique. In contrast to conventional reflectometry, where a microwave beam enters the plasma at normal incidence with respect to the magnetic field and is used to measure the electron density profile, Doppler reflectometry uses a deliberate oblique incidence angle and is used to measure the plasma velocity and radial electric field profile [110, 111]. Thus, it is of interest for the study of velocity fluctuations such as the geodesic acoustic mode. Section 5.1 starts with a compact introduction to the propagation of microwaves in plasma and the principle of Doppler reflectometry. Section 5.2 outlines the ASDEX Upgrade V-band Doppler reflectometer diagnostics. The determination of Doppler shift and turbulence amplitude from the raw data are discussed in the following chapter.

### 5.1 Wave propagation and reflectometry

The propagation of microwaves in a plasma depends on the properties of the plasma, the presence of a magnetic field  $\mathbf{B}$ , as well as the polarisation of the microwaves relative to  $\mathbf{B}$ . An electromagnetic wave  $\mathbf{X}(\mathbf{r}, t)$  with wavevector  $\mathbf{k}$  and angular frequency  $\omega$  can be written as

$$\mathbf{X}(\mathbf{r}, t) = \mathbf{X}_0 \exp(i(\mathbf{k} \cdot \mathbf{r} - \omega t)). \quad (5.1)$$

In general, the absorption and reflection of waves depends on the refractive index

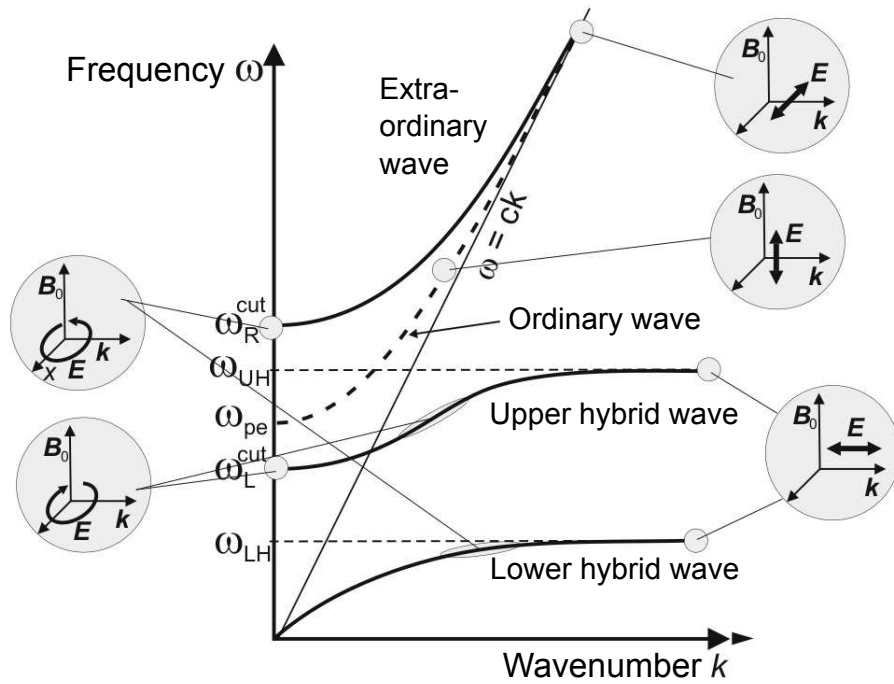


Figure 5.1: Dispersion relation diagram for electromagnetic waves in a cold magnetised plasma, such as in a fusion confinement device, with propagation perpendicular to the magnetic field ( $\mathbf{k} \perp \mathbf{B}_0$ ). Adapted from Ref. [3]

$N$  of the plasma, which is defined as follows:

$$N = \frac{c}{v_{\text{ph}}} = \frac{ck}{\omega}. \quad (5.2)$$

$v_{\text{ph}} = \omega/k$  is the phase velocity of the wave, i.e. the velocity at which a point of constant phase moves along the wave.  $c$  is the vacuum speed of light. If the refractive index approaches infinity, the energy of the wave is absorbed. This is called a resonance, and is used for microwave heating such as ECRH (see Ch. 4.2). In the case of  $N = 0$ , the wave is at a so-called cutoff. Instead of propagating further into the plasma, the wave is reflected. The refractive index can also be defined as the vector quantity  $\mathbf{N} = (c/\omega) \mathbf{k}$ , from which different refractive indices  $N_{\perp}$  and  $N_{\parallel}$  perpendicular or parallel to the magnetic field in a plasma can be obtained.

In a magnetised plasma, the cutoff condition depends on the orientation of the oscillating electric field vector  $\mathbf{E}$  of the incident wave. If  $\mathbf{E}$  is parallel to the background magnetic field  $\mathbf{B}_0$ , which is called the O-mode (ordinary mode), then the situation is identical to a wave in an unmagnetised plasma. For normal incidence,

the following equation can be derived:

$$N^2 = 1 - \frac{\omega_p^2}{\omega^2}. \quad (5.3)$$

The cutoff condition  $N = 0$  is fulfilled when the local plasma frequency  $\omega_p$  equals the wave frequency:

$$\omega_O^{\text{cut}} = \omega_p = \sqrt{\frac{n_e e^2}{\epsilon_0 m_e}}. \quad (5.4)$$

Therefore, the cutoff location for O-mode waves is determined purely by the plasma density. For X-mode (extraordinary mode) waves, where  $\mathbf{E}$  is perpendicular to  $\mathbf{B}_0$ , the cutoff depends on the background magnetic field as well as the plasma density. In the case of normal incidence, two cutoffs  $\omega_L^{\text{cut}}$  and  $\omega_R^{\text{cut}}$  can be derived from the dispersion relation

$$N^2 = \frac{(\omega^2 - (\omega_L^{\text{cut}})^2)(\omega^2 - (\omega_R^{\text{cut}})^2)}{(\omega^2 - \omega_{\text{UH}}^2)(\omega^2 - \omega_{\text{LH}}^2)}. \quad (5.5)$$

$\omega_L^{\text{cut}}$  and  $\omega_R^{\text{cut}}$  are named after the fact that the X-mode wave is left- and right-hand polarised at the cutoff, respectively. They are defined as follows:

$$\omega_L^{\text{cut}} = \frac{1}{2} \left( \sqrt{\omega_c^2 + 4\omega_p^2} - \omega_c \right), \quad (5.6)$$

$$\omega_R^{\text{cut}} = \frac{1}{2} \left( \sqrt{\omega_c^2 + 4\omega_p^2} + \omega_c \right), \quad (5.7)$$

$$\text{with } \omega_c = \frac{eB}{m_e}. \quad (5.8)$$

$\omega_c$  is the electron cyclotron frequency. The upper and lower hybrid resonances  $\omega_{\text{UH}}$  and  $\omega_{\text{LH}}$  are important for plasma heating schemes:

$$\omega_{\text{UH}} = \sqrt{\omega_c^2 + \omega_p^2}, \quad (5.9)$$

$$\omega_{\text{LH}} \approx \sqrt{\omega_c \omega_{ci}}, \quad \text{with ion cyclotron frequency } \omega_{ci} = \frac{q_p B}{m_i}. \quad (5.10)$$

Figure 5.1 illustrates the dispersion relation for electromagnetic waves in a cold magnetised plasma. O-mode waves can penetrate the plasma until the density is high enough to fulfill the cutoff condition  $\omega = \omega_p$ , while for X-mode waves the cutoff will be further outside, since  $\omega_R^{\text{cut}} > \omega_p$ . For reflectometer applications, choosing between O- and X-mode allows probing different radial regions of the plasma. Figure 5.2 shows typical radial profiles of O- and X-mode cutoffs in a low density L-mode

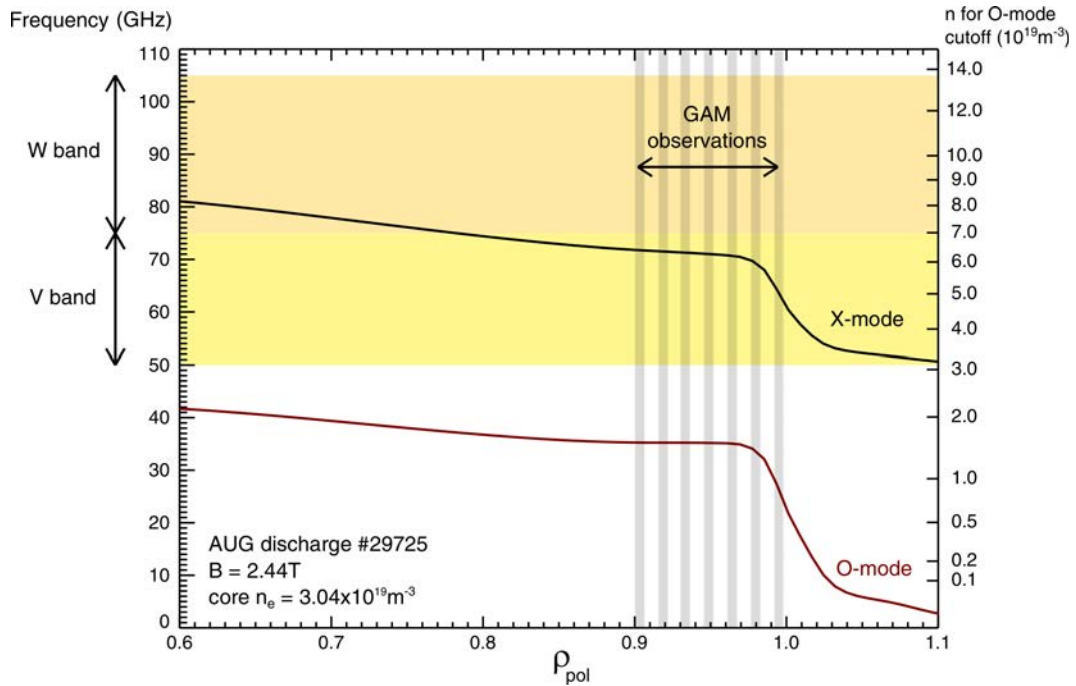


Figure 5.2: Radial profiles of O-mode and upper X-mode cutoffs in a low-density L-mode discharge. The right axis displays the corresponding electron density for the O-mode cutoff condition. Due to the low core density, reflectometry measurements in the plasma edge (the region in which GAMs are seen is highlighted) are only possible using V-band systems in X-mode polarisation.

ASDEX Upgrade plasma. In this case, the core density is so low that the O-mode cutoff condition is not fulfilled. Studies of the low density plasma edge region, where GAMs are expected (cf. Sec. 3.4.3), are therefore usually performed using X-mode microwaves in the V-band (50–75 GHz). At higher densities it is possible to use O-mode polarisation or the W-band (75–110 GHz) in X-mode.

In a simple reflectometer, as schematically pictured in Fig. 5.3, microwaves are launched from an antenna at a specific frequency. They enter the plasma at normal incidence and propagate until they reach the cutoff layer. The cutoff density is determined by the frequency of the launched wave, therefore higher launching frequencies result in a longer path through the plasma. A receiving antenna measures the reflected microwave. From the measured phase differences for various launching frequencies, a radial profile of the electron density can be reconstructed, assuming that the plasma is stable during the frequency sweep. A more detailed description of the technique and the ASDEX Upgrade reflectometer systems can be found in Ref. [112]. The diagnostic can also be used for the study of turbulence properties,

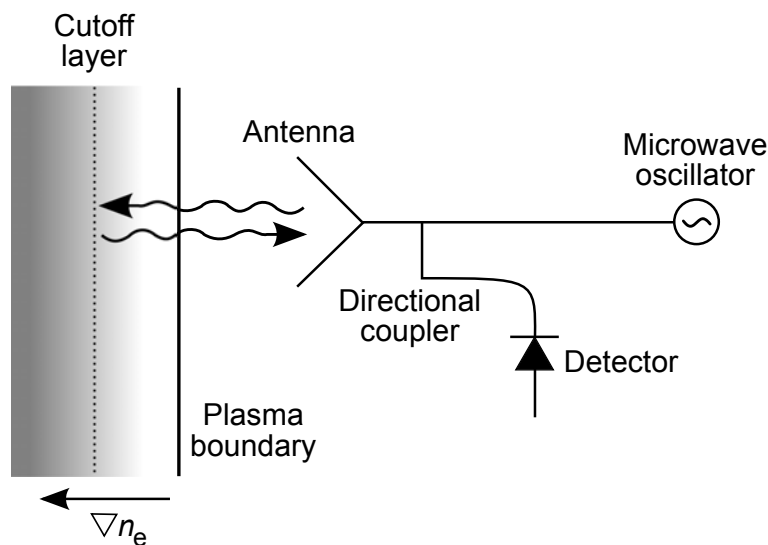


Figure 5.3: Illustration of a simple reflectometer: a microwave beam, created by an oscillator, is emitted from an antenna and enters the plasma at normal incidence. It is reflected at the cutoff layer and exits the plasma in the opposite direction. The incoming beam goes through a directional coupler and is measured by a detector.

such as correlation lengths [113].

The main difference in the case of a Doppler reflectometer system is the introduction of an oblique launching angle  $\theta_0$ , as pictured in Fig. 5.4. This has multiple effects: first, the cutoff condition changes. Unlike the case of normal incidence, the wave is no longer reflected when  $N = 0$  is fulfilled. Instead, it gradually changes direction due to refraction, as soon as it enters the plasma, and will be reflected at a point with  $N^2 > \sin^2 \theta_0$  (or  $N^2 = \sin^2 \theta_0$ , in a slab approximation of the plasma edge). Secondly, the reflected beam will now exit the plasma at a different position, instead of being directed back towards the emitting antenna. The effect of the launching angle  $\theta_0$  and the plasma geometry on the beam path and cutoff location is illustrated in the ray tracing [114] simulations of Fig. 5.5 for simplified slab and circular models and identical launching frequencies.

Due to the fact that the cutoff layer is not smooth, but instead corrugated by turbulent structures, scattering will occur in the forward and backward directions. This can be described in terms of coherent microwave scattering, where conservation of energy and momentum apply. It is expressed by the following equations, where incident microwave radiation with wave vector  $\mathbf{k}_i$  and frequency  $\omega_i$  is scattered by a

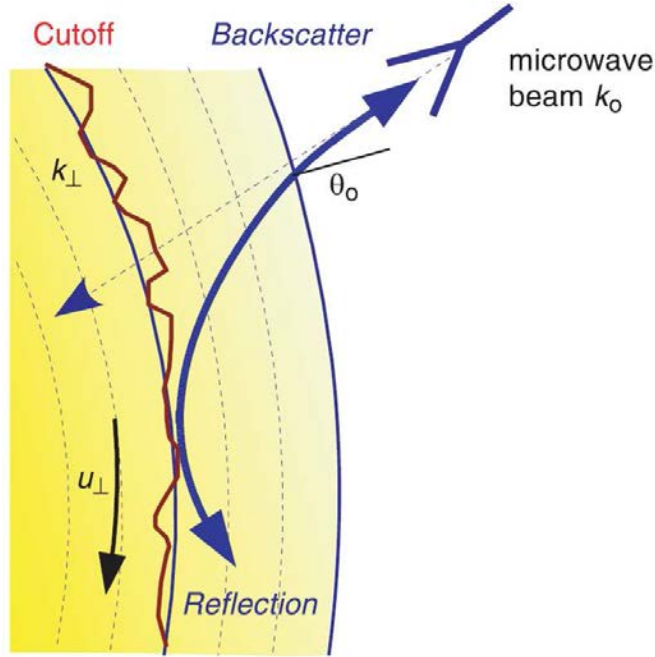


Figure 5.4: Schematic illustration of a Doppler reflectometer diagnostic: a microwave beam with wavenumber  $k_0$  is launched at the plasma with an angle  $\theta_0$ . It is reflected at the cutoff layer, where turbulent structures with wavenumber  $k_{\perp}$ , traveling at velocity  $u_{\perp}$ , lead to backscattering towards the antenna. Adapted from Ref. [9].

coherent plasma fluctuation  $(\mathbf{k}, \omega)$  and continues as a scattered microwave  $(\mathbf{k}_s, \omega_s)$ :

$$\mathbf{k}_s = \mathbf{k} + \mathbf{k}_i, \quad (5.11)$$

$$\omega_s = \omega + \omega_i. \quad (5.12)$$

Of interest for Doppler reflectometry is the backscattered radiation that returns to the emitting antenna location, i.e. when  $|\mathbf{k}_i| = |\mathbf{k}_s| = k_0$ . In slab geometry, the wavenumbers (parallel to the surface), are then defined as:

$$k_i = k_0 \sin \theta_0, \quad k_s = -k_i = -k_0 \sin \theta_0. \quad (5.13)$$

Therefore, from Eq. 5.11 the following relation for Bragg backscattering at Bragg order  $m_B$  is derived:

$$m_B k = -2k_0 \sin \theta_0 \quad \text{for } m_B = -1, \quad (5.14)$$

$$\Rightarrow k = 2k_0 \sin \theta_0. \quad (5.15)$$

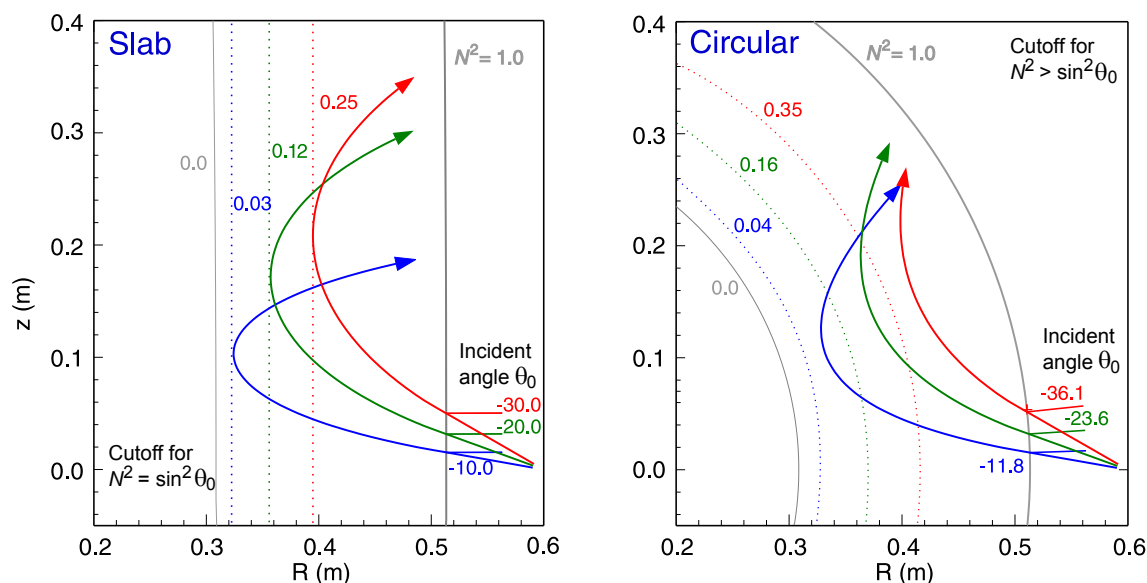


Figure 5.5: Comparison of microwave ray tracing for oblique incidence. Dotted lines mark constant values of  $\sin \theta_0$  for the corresponding three incident angles. The microwave frequency and the parabolic density profile are constant throughout all traces. Left: in slab geometry, the cutoff is exactly at  $N^2 = \sin^2 \theta_0$ . Right: in circular geometry (note the changed angles of incidence due to the curved plasma surface), the cutoff is shifted outwards to  $N^2 > \sin^2 \theta_0$ .

This equation illustrates that Doppler reflectometry is a wavenumber-selective diagnostic. For a given launch angle  $\theta_0$  and emitted wavenumber  $k_0$ , only backscattered radiation from structures with a specific  $k$  will be detected. Diagnostic setups with a variable tilt launch angle allow for measurements within a range of the  $k$ -spectrum.

The influence of the Doppler effect on this diagnostic technique comes due to the fact that the plasma, and hence also the turbulent structures at the cutoff layer, are in motion. This motion with a turbulence velocity  $\mathbf{u}$  introduces a Doppler shift  $\omega_D$  in the backscattered beam:

$$\omega_D = \mathbf{k} \cdot \mathbf{u} = k_{\perp} u_{\perp} + k_{\parallel} u_{\parallel} + k_r u_r. \quad (5.16)$$

The turbulence wavenumber components parallel and perpendicular to the magnetic fields are typically very different in magnetically confined plasmas. This is due to the faster parallel mobility, which in turn leads to density fluctuations that are stretched out along the magnetic field lines with  $k_{\parallel} \ll k_{\perp}$ . The radial wavenumber of the incident wave approaches zero at the cutoff location,  $k_r \rightarrow 0$ , so contributions

from  $k_r$  are expected to be small and symmetrical. Therefore, the Doppler shift is mainly determined by the contribution of the perpendicular turbulent velocity  $u_\perp$  [111]:

$$\omega_D \approx k_\perp u_\perp. \quad (5.17)$$

Inserting this into Eq. 5.15, under the assumption that  $k \approx k_\perp$  at the cutoff layer for antennas aligned to the field lines, yields the following relation in slab geometry:

$$\omega_D = 2u_\perp k_0 \sin \theta_0. \quad (5.18)$$

For known incident angle and wavenumber, this equation allows the measurement of the perpendicular turbulent velocity through the Doppler shift of the backscattered radiation. It is important to note that these equations are correct in the slab geometry where the cutoff condition  $N^2 = \sin^2 \theta_0$  applies, as mentioned above. Figure 5.5 illustrates that when curved plasma geometry is taken into account, the scattering location, where the refractive index  $N$  takes its minimal value, is further displaced towards the plasma edge. In this case the cutoff location and the refractive index can be calculated using ray tracing equations. The generalised form of Eq. 5.18 gives the following relation between Doppler shift,  $u_\perp$  and  $N_\perp$ :

$$\omega_D = u_\perp 2k_0 N_\perp. \quad (5.19)$$

If one wants to use the measured Doppler shift in order to investigate flow phenomena such as the GAM, or the radial electric field  $E_r$ , it is important to note that  $u_\perp$  consists of two components:

$$u_\perp = v_{E \times B} + v_{\text{ph}}. \quad (5.20)$$

$v_{\text{ph}}$  is the phase velocity of the density fluctuations, i.e. the velocity of the turbulence in the frame of the plasma.  $v_{E \times B}$  is the background plasma velocity relative to the laboratory frame. From Doppler measurements alone, it is impossible to determine the magnitude of each contribution, and whether one term is dominant. If it can be shown that the  $E \times B$ -velocity is significantly larger than  $v_{\text{ph}}$ , then the Doppler shift can be used directly to measure  $E_r$  (since the magnetic field is known). There are multiple indications that this condition is in fact fulfilled in typical ASDEX Upgrade plasma edge conditions. Recent comparisons of electric field profile measurements from Doppler reflectometry and charge exchange recombina-

tion spectroscopy (CXRS) show good agreement in the edge region, which would only be the case for negligible  $v_{\text{ph}}$  [115]. Comparisons between ball pen probe and Doppler results at ASDEX Upgrade lead to the same conclusion [116]. Similar observations have also been made with CXRS and Doppler comparisons on the Tore Supra tokamak [117] and the W7-AS stellarator [111, 118]. Probe and beam emission spectroscopy measurements on DIII-D [119] and TJ-II [120] also confirm the dominance of  $v_{E \times B}$ .

Additionally, simulations with the linear gyrokinetic GS2 code and the non-linear gyrokinetic GENE code give further indications that the turbulent phase velocity is expected to be on the order of a few 100 m/s in the plasma edge (for typical probe values of  $k_{\perp}$ ), which is significantly below the background  $E \times B$  velocity [121]. Thus,  $u_{\perp} \approx v_{E \times B}$  can be assumed, and  $E_r$  can be determined from Doppler shift measurements.

Another factor specifically relevant to the study of geodesic acoustic modes is the fact that GAM velocity fluctuations  $\tilde{v}_{E \times B}$  can be obtained from  $u_{\perp}$ , regardless of whether  $v_{\text{ph}}$  is significant or not, since only the magnitude and frequency of the oscillations is of relevance. Fluctuations in  $v_{\text{ph}}$  itself, which could theoretically influence the measured Doppler shift, are not expected at the GAM frequency [60].

## 5.2 ASDEX Upgrade V-band Doppler reflectometers

Multiple Doppler reflectometry systems are currently in operation on the ASDEX Upgrade tokamak. Figure 5.6 shows a poloidal cross-section of the vacuum vessel with a typical lower single null plasma shape and the various reflectometer lines of sight. Two reflectometer systems operating in V-band (50–75 GHz) are connected to bistatic antenna pairs (i.e. two separate antennas in close proximity for launching and for receiving the microwave radiation) positioned above and below the midplane. The upper antennas are positioned at a fixed downward tilt of  $33.8^{\circ}$  with respect to the midplane and are optimised for O-mode polarisation. The lower antenna pair is fixed at  $42.5^{\circ}$  upward and is optimised for X-mode polarisation [122]. The antennas are also respectively turned by  $-3.1$  and  $+2.2^{\circ}$  in the toroidal direction in order to align with the field inclination in the plasma edge for typical left-hand helicity configuration (see Sec. 4.4) and  $q_{95} = 4$ . They are located on the tokamak low-

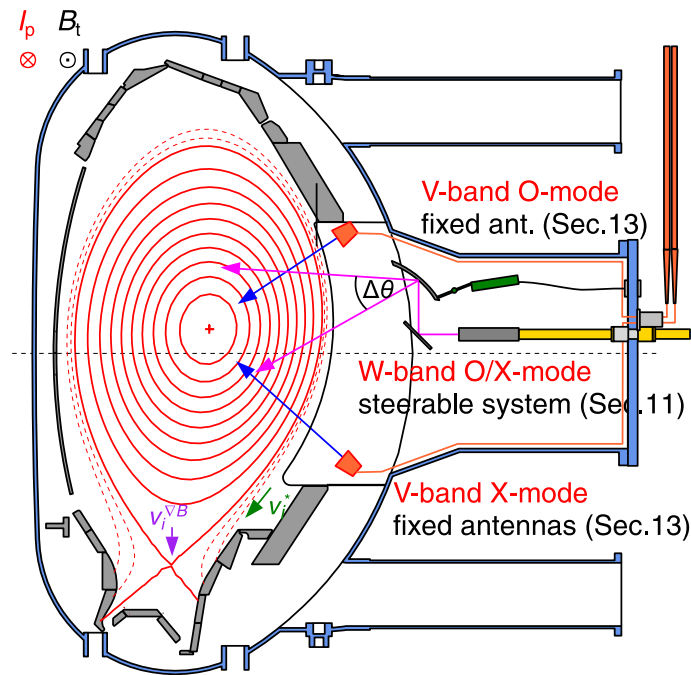


Figure 5.6: Schematic cross-section of ASDEX Upgrade during a divertor discharge, highlighting the measurement locations of the Doppler reflectometer systems.

field-side in sector 13 of ASDEX Upgrade, see also Fig. 4.2. Due to the fixed tilt, the probed wavenumbers are in a narrow range around approximately  $9\text{--}12\text{ cm}^{-1}$  for X-mode measurements, with the variation depending on launch frequency and plasma shape.

In order to improve the radial range available to Doppler measurements, and to make a dynamic selection of the wavenumber possible, a W-band system (75–104 GHz) with an adjustable line of sight was installed in sector 11 on the low-field-side [123]. The antennas of the W-band system were later upgraded, allowing the tilt angle with respect to the plasma surface to be changed via a remote steerable mirror [124]. For the study of GAMs the V-band systems are predominantly used because, as seen in Fig. 5.2, they cover the plasma edge in typical AUG discharge conditions, while even the X-mode W-band cutoffs are too far inside.

The two V-band systems, which are built identically [6], use a heterodyne receiver system with IQ detection, which has several advantages over a simple homodyne receiver. In a homodyne system, the received signal of frequency  $\omega_0 + \Delta\omega$  is mixed with the emitted reference frequency  $\omega_0$  and down-converted to zero frequency. Due to the  $1/f$  noise characteristic of the mixer, the sensitivity around zero frequency

suffers. In a heterodyne system, both the source signal ( $\omega_0$ ) and the backscattered signal ( $\omega_0 + \Delta\omega$ ) are mixed with a local oscillator signal at frequency  $\omega_{LO}$ . This moves the mixed signal to a frequency range with less inherent noise, and thus higher dynamic range. The mixer is then followed by an IQ detector to give access to the sign of the phase. Instead of just directly mixing (down-converted) reference and signal, the reference is split and additionally shifted by  $90^\circ$  and mixed with the signal. The two mixed signals are called in-phase (I) and quadrature (Q) signal:

$$I = A \cos \phi, \quad (5.21)$$

$$Q = A \sin \phi, \quad (5.22)$$

with amplitude  $A = \sqrt{I^2 + Q^2}$  and phase  $\phi = \arctan(Q/I)$ . Thus, while more expensive than a homodyne setup, using a heterodyne system is important in order to determine the sign of the Doppler shift.

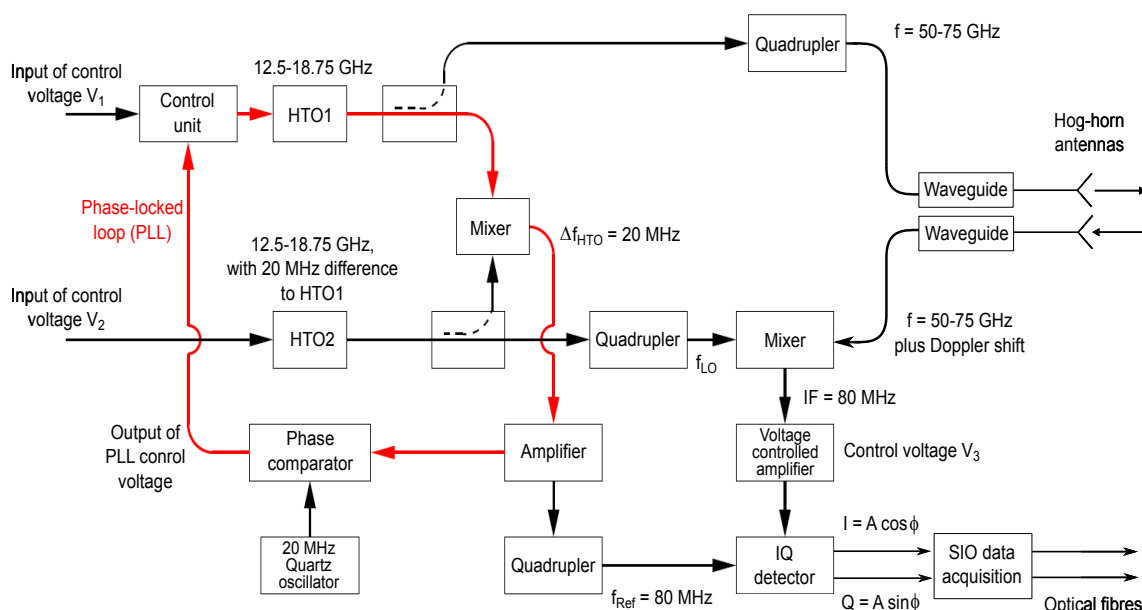


Figure 5.7: Circuit diagram of the ASDEX Upgrade V-band reflectometer. The phase-locked loop, responsible for keeping the frequency difference  $\Delta_{HTO}$  between HTO1 and HTO2 constant, is highlighted in red.

Figure 5.2 shows the circuit diagram of the AUG V-band Doppler reflectometers. As necessary for a heterodyne system, there are two hyper-abrupt varactor tuned

oscillators (microwave transmitter HTO1 and local oscillator HTO2) with a tunable frequency range from 12.5–18.75 GHz. They are kept at a constant frequency difference  $\Delta F = 20$  MHz, using a phase-locked loop with a 20 MHz quartz oscillator as reference. A set of frequency quadruplers are used to bring the microwaves to the V-band range of 50–75 GHz and the frequency difference to 80 MHz. The signal is launched into the plasma and the backscattered radiation is caught by the receiving antenna and down-converted to the intermediate frequency (IF) of 80 MHz by mixing with the HTO2 signal. An IQ detector converts this signal and the reference into in-phase and quadrature signals which are passed to the data acquisition system.

There are three control voltage inputs for setting the desired launch frequency and the IF amplifier gain. The analog control voltages are set by a waveform generator, using 12-bit digital-to-analog converters (DACs). The frequency pattern is programmed remotely prior to the discharge, and usually consists of multiple steps at different launch frequencies, allowing for radial sweeps of the plasma. The interval between frequency steps can be as small as 1 ms. The pre-programmed pattern will run multiple times until the end of the discharge, lasting for 7 s. The measured analog I and Q signals are filtered at 7 MHz in order to eliminate aliasing effects. They are then digitised using 12-bit analog-to-digital converters (ADCs) with a sampling rate of 20 MHz. A sufficiently high sampling rate is fundamental for the study of high-frequency oscillations such as the GAM. The step length in the frequency stepping setup needs to be chosen carefully. It has to be long enough to ensure sufficient raw data to reduce statistical errors for reliable results, however a higher number of steps will increase the available radial range and resolution. Additionally, it must be noted that the plasma conditions are often not stable over multiple seconds, and meaningful radial profiles can only be measured over the span of hundreds of milliseconds or less.

The bistatic antennas in sector 13 are connected to the reflectometers by a series of waveguides (rectangular fundamental and circular oversized) and mitre bends. The antennas are pairs of pyramid-shaped hog-horns with elliptic focusing mirrors. They were designed for maximum antenna pattern overlap and can be considered as a monostatic system. A more detailed description of the setup of the V-band antennas and the data acquisition system is given by Klänge [6]. The two V-band reflectometers can also be connected to the same antenna pair by using directional couplers. This way, simultaneous measurements in either O- or X-mode are possible. This setup is necessary for radial correlation measurements [5, 125].

# Chapter 6

## Data analysis

This chapter introduces the techniques which were employed for the analyses of the experimental ASDEX Upgrade data in the following chapters. Section 6.1 describes how the Doppler shift, which corresponds to the perpendicular plasma velocity, is extracted from the raw Doppler reflectometer data. Subsequently, Sec. 6.2 describes how the geodesic acoustic mode is identified and its frequency and amplitude are determined from the time series of the Doppler shift. Section 6.3 introduces an alternate approach to GAM identification and compares it to the conventional method. Finally, in Sec. 6.4, two cross-correlation methods are introduced which are used to study the radial GAM correlation and propagation.

### 6.1 Determining Doppler shift and amplitude

In order to interpret the data from Doppler reflectometry measurements in any meaningful way, it is important to reconstruct the measurement location. Only then can radial profiles of plasma velocity and radial electric field be made, and the data can be brought into context with measurements from other diagnostics. The safety factor  $q$  and the local plasma temperatures  $T_e$  and  $T_i$  for example, which play a major role in the properties of the geodesic acoustic mode, vary greatly over very short radial distances in the plasma edge region. Similarly, correlation measurements depend on knowing the radial position of both channels and the separation between them. Equations 5.4 and 5.7 show that the cutoff conditions for microwaves in the plasma are determined by the density (for O- and X-mode) and magnetic field (for X-mode) profiles in the plasma. When both profiles are known, a beam or ray

tracing code can be used to determine the exact cutoff location. The magnetic field profile for any plasma discharge in ASDEX Upgrade is obtained from the so-called magnetic equilibrium reconstruction using edge magnetic coil measurements [126]. Electron density profiles are measured by multiple diagnostics. The following section introduces them and their application to Doppler reflectometry measurements in more detail.

### 6.1.1 Density profile reconstruction

The electron density  $n_e$  is one of the key plasma parameters and can be measured by number of diagnostics. While any single diagnostic is not sufficient to cover the full radial range in sufficient resolution, a density profile can be reconstructed from a combination of edge and core diagnostics. The most important diagnostics for density profile reconstruction are the Thomson scattering system, the DCN/CO<sub>2</sub> laser interferometer system and the lithium beam diagnostic, which were introduced in Sec. 4.3, as well as the conventional frequency-modulated continuous-wave (FMCW) reflectometer, which was mentioned in Sec. 5.1.

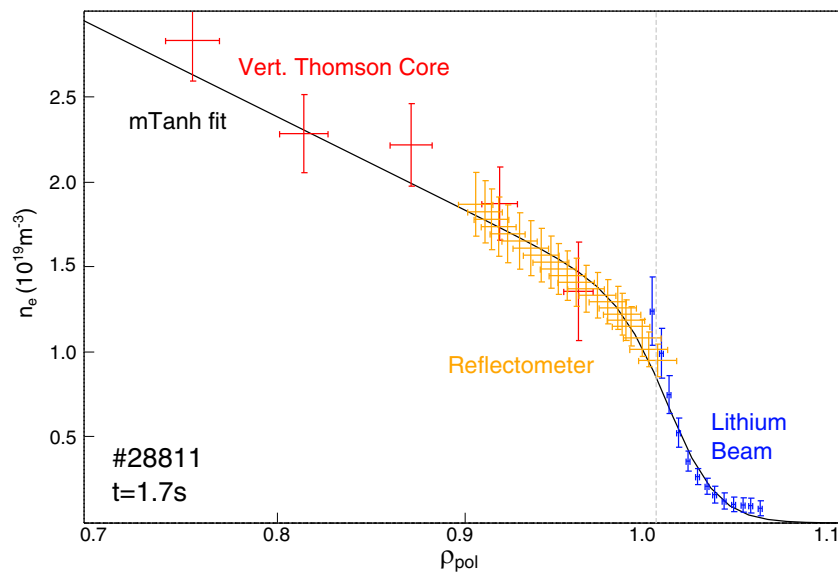


Figure 6.1: Reconstructed density profile for AUG L-mode discharge #28811,  $t = 1.7$  s. Data from the profile reflectometer, lithium beam and vertical Thomson scattering (core) systems were used.

Figure 6.1 shows a density profile for a typical ASDEX Upgrade L-mode discharge that was reconstructed from reflectometry, lithium beam and core Thomson

scattering data. The edge region shows good agreement between reflectometry and lithium beam diagnostics. In order to use the beam tracing code, it is important to fit a smooth, monotonic profile. The profile is fitted as a modified hyperbolic tangent function:

$$\text{mTanh}(z) = B + A(1 + \alpha z)\text{Tanh}(z) \quad (6.1)$$

Here,  $z$  is the radial position relative to the inflection point of the curve, and  $A$ ,  $B$ , and  $\alpha$  are fitted parameters depending on the slope in the gradient and the density level in the pedestal and scrape-off layer. A constraint for the modified function is that the density goes to zero in the scrape-off layer region. Experimental data from a variety of tokamak plasmas has shown that a modified hyperbolic tangent function is a good fit for the edge region [127], especially in H-mode discharges. But also for ohmic and L-mode discharges in the divertor configuration, AUG experiments have reliably shown good fit results using the modified Tanh.

### 6.1.2 Beam tracing code TORBEAM

A simple way to estimate the Doppler measurement location would be to calculate the intersection between the Doppler antenna lines of sight and the cutoff surfaces, based on the  $n_e$  and  $B$  profiles. However, as mentioned in Sec. 5.1, in realistic plasma conditions the beam will be subject to refraction and gradually change direction as it travels through the plasma. In ASDEX Upgrade, the three-dimensional beam tracing code TORBEAM is used for such calculations [114]. It specifically takes refractive processes into account, making it suitable for Doppler reflectometry calculations. As inputs TORBEAM uses the magnetic equilibrium and the reconstructed density profile from the previous section. The launched beam is modelled as a Gaussian beam with beam width and divergence equivalent to those measured for the ASDEX Upgrade Doppler antennas [6].

Figure 6.2 shows example beam traces from TORBEAM, for a lower single null low-density discharge. In this case, microwaves in X-mode polarisation are launched from the lower antenna, which sits in the limiter shadow (cf. Fig. 5.6), at frequencies of 57 and 68.5 GHz. The beam travels in a straight line while it is outside the plasma, but once it enters it deviates due to refraction before reaching its turning point. At higher launch frequency the path through the plasma is longer and the refractive effects are stronger. The location of the turning point will be further outside than the cutoff that is calculated for straight or oblique incidence on a slab geometry

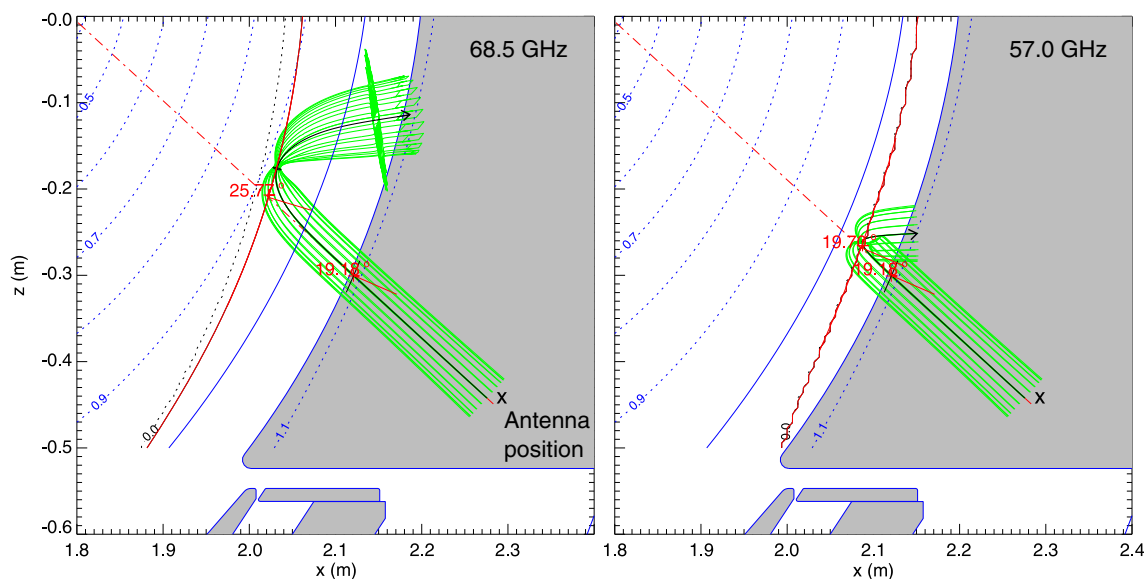


Figure 6.2: 2D projection of beam traces for X-mode microwave radiation in AUG discharge #29725, computed with TORBEAM. Blue lines indicate flux surfaces, red lines X-mode cutoff surfaces. Frequencies are 68.5 (left) and 57.0 GHz (right)

plasma, as shown in Fig. 5.5. While the effects of refraction are small for V-band X-mode microwaves, due to cutoffs close to the plasma edge, they are much stronger for O-mode polarisation. The exact cutoff position is calculated at the point at which the refractive index  $N^2$  is minimised. The location of the X-mode cutoff is shown as a red line in Fig. 6.2, while the flux surfaces are shown in blue (the solid blue line marks the last closed flux surface). While a full-wave simulation of the beam might provide even more reliable results, it requires large computational effort and might run multiple hours, as opposed to a TORBEAM calculation that requires only a few seconds. Comparisons between beam tracing and full-wave simulation have confirmed the accuracy of TORBEAM in determining the cutoff position [121].

Alongside the exact cutoff location (both in terms of Euclidean coordinates, as well as normalised poloidal flux radius  $\rho_{\text{pol}}$ ), TORBEAM also provides  $k_{\perp}$  and  $k_{\parallel}$  along the ray path. From the value of  $k_{\perp}$  at the cutoff position and the measured Doppler shift  $\omega_D$ , the perpendicular velocity  $u_{\perp}$  at this position can be calculated via Eq. 5.17.

### 6.1.3 Doppler shift measurements

The previous sections outlined how measurement location and turbulence wavenumber can be obtained. The Doppler reflectometer itself, however, is used to measure the frequency shift in the received IQ signal.

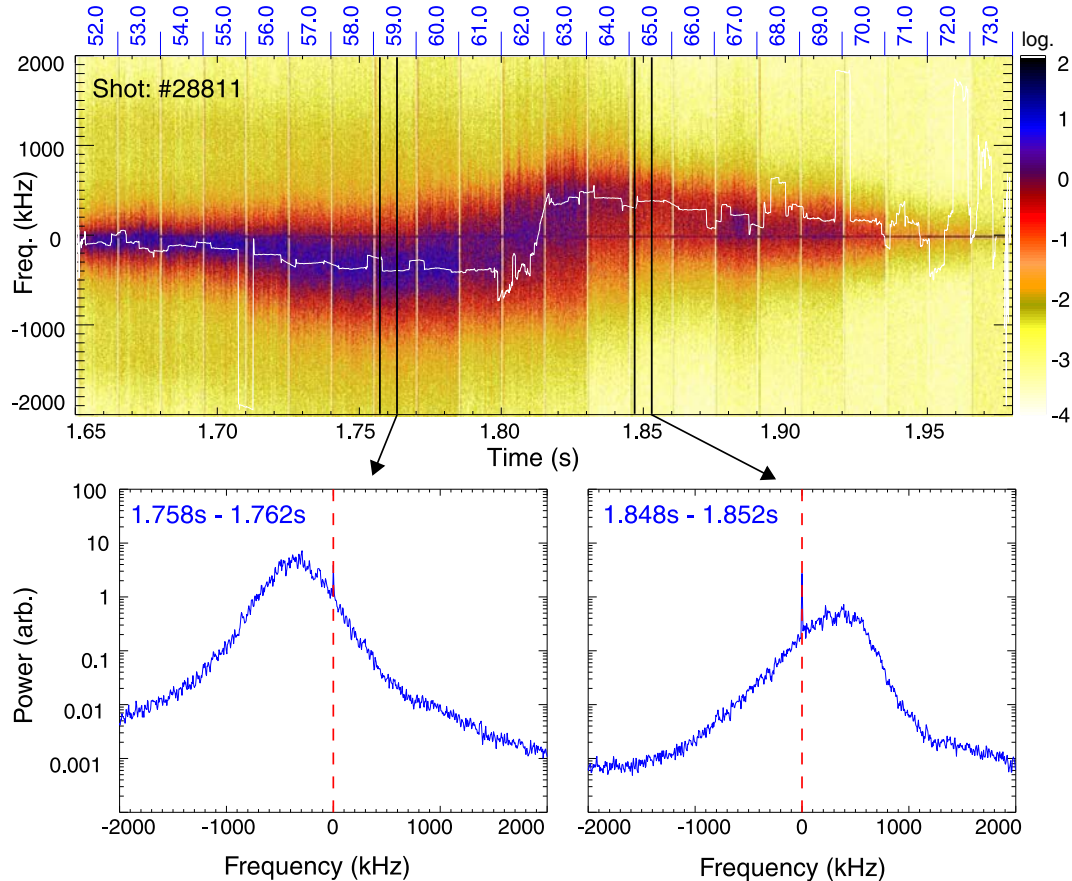


Figure 6.3: Top: spectrogram of raw X-mode Doppler reflectometer data from AUG discharge #28811,  $t = 1.65\text{--}1.98\text{ s}$ , for one radial sweep (52–73 GHz, 15 ms per step, as indicated above the upper figure) in a low-density L-mode plasma. The white line marks the weighted mean of the asymmetric component of the power spectrum. Bottom: Averaged power spectra with discernible Doppler shift, measured in the scrape-off layer (left, at 59 GHz) and inside the  $E_r$  well (right, at 65 GHz).

Figure 6.3 shows an example power spectrum of the complex Doppler signal  $I + iQ = A\exp(i\phi)$  during a typical V-band frequency sweep. Here, the launch frequency is increased stepwise from 52 to 73 GHz, in 1 GHz increments every 15 ms. In low-density L-mode conditions, the V-band range covers both the scrape-off layer as well as the  $E_r$  well and the gradient region in which GAMs are typically present.

The dynamic range of the spectrum is four orders of magnitude above the noise floor of the electronics. From the spectrogram and the two example spectra it can be seen how the Doppler shift  $f_D$  changes sign in this region. This corresponds to a change in rotation direction and radial electric field, which is very typical for the edge region. The configuration of plasma current  $I_p$ , toroidal magnetic field  $B_t$  as well as the antenna position, i.e. above or below the midplane, have to be known in order to determine the direction of rotation. For the standard left-hand helicity configuration with negative  $B_t$  and positive  $I_p$ , and use of the X-mode antenna pair (below the midplane, see Fig. 5.6), a positive  $f_D$  corresponds to rotation in the electron diamagnetic drift direction and a negative Doppler shift corresponds to the ion diamagnetic drift direction. In the example from Fig. 6.3, the  $E \times B$  drift points in the electron direction inside the separatrix and in the ion direction in the SOL. Both example spectra also show strong but very narrow peaks at the zero frequency component due to the carrier signal. In some cases a symmetric peak is found around the zero component, which is due to direct reflection.

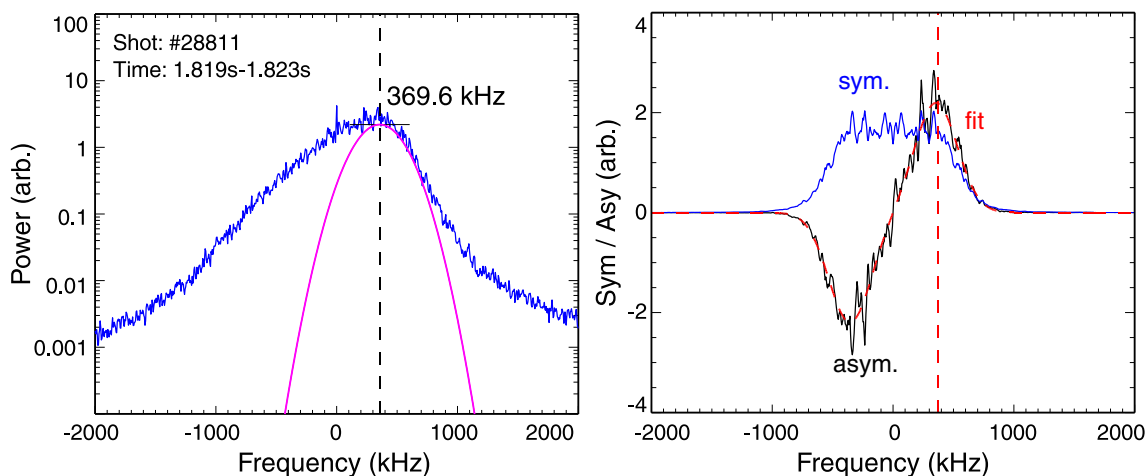


Figure 6.4: Left: Frequency spectrum at  $E_r$  minimum (63 GHz) during AUG discharge #28811, cf. Fig. 6.3, with  $m_B = -1$  Doppler peak at  $f_D = 369.6$  kHz. Right: Anti-symmetric (black) and symmetric (blue) part of the same frequency spectrum, with best double Gaussian fit to the anti-symmetric component (red).

There are multiple ways of obtaining  $f_D$  from a frequency spectrum. The most straightforward method is the calculation of the weighted mean  $\langle f \rangle$ , or centre of

gravity, of the spectrum  $S(f)$ :

$$\langle f \rangle = \frac{\int_{-\infty}^{\infty} f S(f) df}{\int_{-\infty}^{\infty} S(f) df}. \quad (6.2)$$

In cases of low direct reflection and a distinct Doppler peak, the weighted mean will give a good estimate of  $f_D$ . However, for a stronger  $m_B = 0$  component, i.e. a strong direct reflection, the weighted mean value will lie between zero and the actual peak, thus it can only be used to determine the sign of the Doppler shift. A different method of estimating  $f_D$  is the fitting of a Gaussian curve to the Doppler spectrum. If the  $m_B = -1$  component is sufficiently separated from a possible  $m_B = 0$  reflection, a simple Gaussian fit will yield Doppler shift  $f_D$  and Doppler peak amplitude  $A_D$ . However, for cases with a  $m_B = 0$  component, the most reliable estimate of  $f_D$  is obtained by fitting a Gaussian only to the asymmetric part of the spectrum, as shown in Fig. 6.4. By separating the spectrum into symmetric and asymmetric components, the influence of the symmetric  $m_B = 0$  peak as well as narrow carrier signal peak is minimised, and a reliable fit to the asymmetric  $m_B = -1$  peak can be obtained.

Generally, Doppler measurements in the AUG edge during L-mode discharges show little direct reflection, as seen from the beam traces in Fig. 6.2. However, antenna sidelobes exist at an angle of  $\pm 15^\circ$  from the tilted antenna, with a strength of about  $-25$  dB [121]. These sidelobes can enter the plasma at close to normal incidence and be reflected back to the antenna, which only has a noticeable effect if the main signal is weak. From experience of AUG edge measurements, the weighted mean is sufficient in order to determine  $f_D$ . For studies of velocity oscillations in particular, such as the GAM, the frequency of fluctuations around the mean Doppler shift is often more important than the exact value of  $f_D$ . Therefore, the weighted mean method is usually employed in all GAM analyses presented in this thesis. Radial profiles of  $u_\perp$  and  $E_r$  were created using fits to the whole or asymmetric power spectra.

## 6.2 GAM detection

The extraction of the GAM properties from the raw Doppler reflectometer signal is a multi-step process, as shown in Fig. 6.5. First, the Doppler shift frequency  $f_D$

and amplitude  $A_D$  are calculated from the IQ signal. The perpendicular velocity  $u_{\perp}$  can then be calculated from  $f_D$  and the refractive index  $N$  at the cutoff location, according to Eq. 5.19.

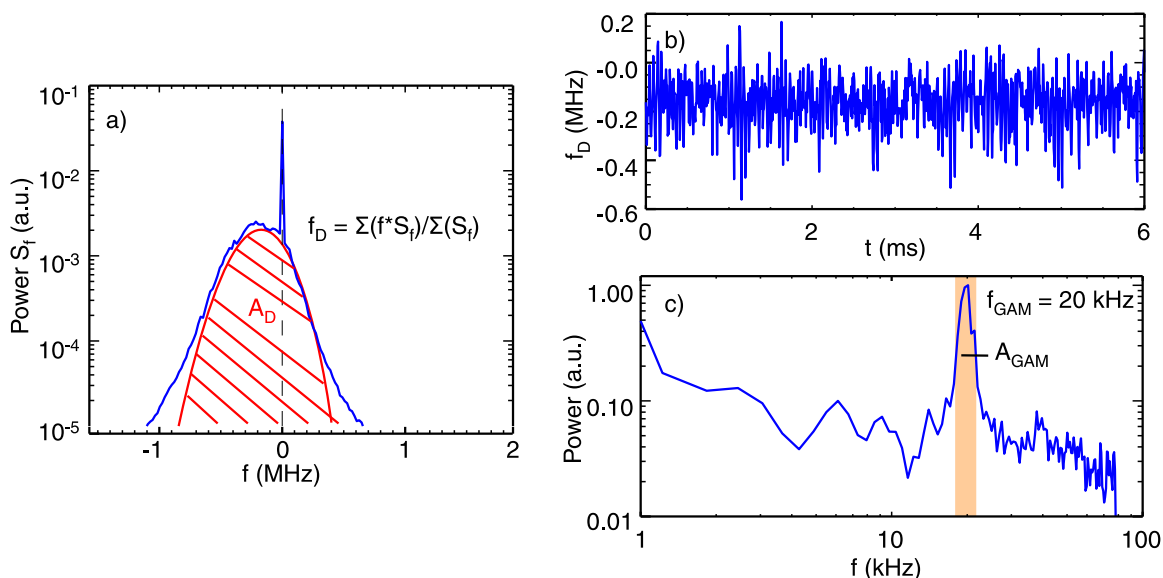


Figure 6.5: Illustration of the GAM detection from reflectometer data. a) Power spectrum calculated from a window of the raw data, exhibiting a clear Doppler shift. b) Time series of the determined Doppler shift frequency (proportional to the flow velocity). c) Power spectrum of the  $f_D$  time series, showing a strong GAM peak at 20 kHz.

The relative turbulence amplitude  $\delta n^2$  at the probed  $k_{\perp}$  is proportional to  $A_D$ . In order to measure GAMs, it is necessary to have a high-resolution time series  $f_D(t)$ . Therefore,  $f_D$  and  $A_D$  are calculated from a small window of the complete IQ signal, which slides forward in time. Finally, an average power spectrum is calculated from  $f_D(t)$ . GAMs appear as distinct peaks in this frequency spectrum, usually in the range of 5–25 kHz for AUG L-mode discharge conditions.

The conventional way to determine the Doppler shift from the raw IQ signal, as outlined in the previous section, is by calculating the power spectrum  $S_f(f)$  with a Fast Fourier Transform (FFT) algorithm and computing a weighted mean:  $f_D = \Sigma f \cdot S_f(f) / \Sigma S_f(f)$ . Typically the original data window (10–15 ms at 20 MHz sampling rate) is split into sub-windows of 256 points (or 12.8  $\mu\text{s}$ ), with 50% overlap, for this calculation. The resulting time series  $f_D(t)$  has therefore a sampling frequency of approximately  $f_s = 156$  kHz. The  $A_D(t)$  time series is computed from the area under the Doppler-shifted spectral peak.

An FFT is then once again used to calculate the average power spectrum from the  $f_D(t)$  time series, up to the Nyquist frequency  $f_{Ny} = f_s/2 = 78$  kHz, which is well-suited for the study of GAMs at AUG. The GAM peak can be quite distinct from the background, as seen in Fig. 6.5, however in some situations the GAM is not strong enough to be clearly identified. Other frequency detection methods may be used instead of the sliding window FFT approach in order to improve the separation of GAM signal from background noise. One such example is the MUSIC algorithm, which is introduced in Sec. 6.3.

The amplitude of the GAM is also obtained from the power spectrum of the  $f_D(t)$  time series. The GAM peak at frequency  $f_{GAM}$  is typically distinct from the background, as seen in the highlighted area of Fig. 6.5 (c). The amplitude is calculated as the peak-to-peak velocity by integrating over the GAM spectral peak [79]:

$$A_{GAM} = \frac{4\pi}{k_{\perp}} \sqrt{\sum_{f_1}^{f_2} S(f_D)} \frac{4}{1.5}, \quad (6.3)$$

where  $f_1, f_2 \approx f_{GAM} \pm 0.6$  kHz. The factor  $4/1.5$  accounts for the Hanning bell-window that is applied to minimise spectral leakage. The perpendicular wavenumber  $k_{\perp}$  is calculated using beam tracing and is typically of the order of 9–10  $\text{cm}^{-1}$  in ASDEX Upgrade Doppler measurements.

### 6.3 Comparison of sliding window FFT and MUSIC techniques

An alternative approach to using a sliding FFT is the Multiple Signal Classification (MUSIC) method [129], which has recently been proposed for Doppler shift estimation [130]. This algorithm assumes that a complex signal  $x(t)$ , i.e. the complex IQ signal that is measured with the Doppler reflectometer, consists of a finite number  $F$  of coherent frequency components  $f_k$  and an incoherent noise part  $n(t)$ :

$$x(t) = \sum_{k=1}^F A_k \exp(-i2\pi f_k t) + n(t). \quad (6.4)$$

Here,  $A_k$  is the amplitude of the corresponding frequency component  $f_k$ . The MUSIC algorithm is used to estimate the number of coherent components, their direction of

arrival as well as the strength and cross-correlation of the different components. After calculating the auto-correlation matrix from the complex signal, its eigenvectors can be used to efficiently separate the signal from the noise. In the practical application for GAM analysis, which is described in Ref. [130], the auto-correlation matrix is sampled in smaller matrices with size  $n_w$ . The MUSIC power estimate, which is calculated from the noise eigenvectors, yields a pseudospectrum  $P_{\text{MUSIC}}(f)$ , which will show a distinct peak at the signal frequency. The maximum frequency that can be detected is limited by the time resolution of the signal, while the frequency resolution can be set freely. For perfectly uncorrelated signal and noise components,  $P_{\text{MUSIC}}$  would diverge at the signal frequency, however in practice strong and narrow peaks are expected to be found.

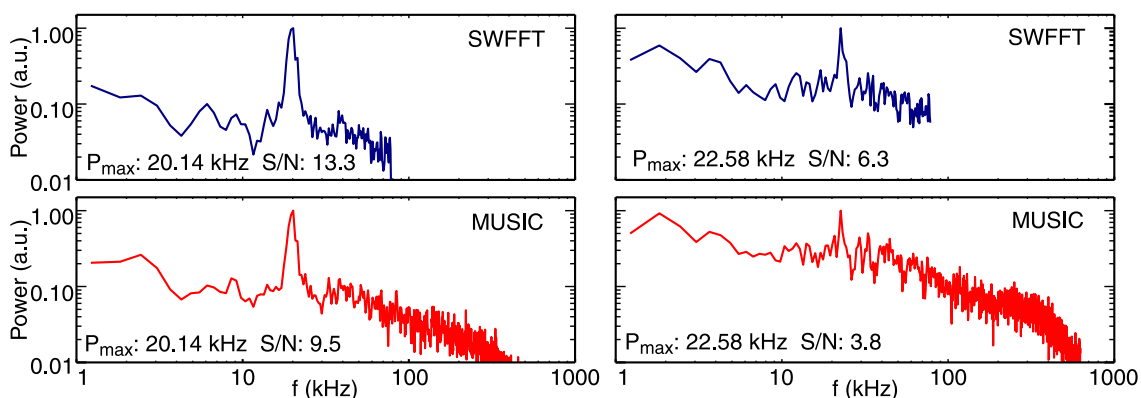


Figure 6.6: Comparison of sliding window FFT (SWFFT) and MUSIC methods for GAM detection. Left: Strong GAM ( $\#29650$ ,  $t = 2.190\text{--}2.205$  s), Right: Weak GAM ( $\#29650$ ,  $t = 2.220\text{--}2.235$  s). MUSIC algorithm parameters as defined in [130]:  $n_{ws} = 32$ ,  $n_{\text{shift}} = 16$ ,  $n_w = 6$ ,  $n_f = 1$  and  $n_{\text{FFT}} = 8192$ .

Figure 6.6 shows average power spectra from two experimental measurements, where GAMs of different intensity and frequency were found. The  $f_D(t)$  signal was computed with both the sliding window FFT (SWFFT) method and with the MUSIC method for comparison. Both methods detect the GAM at the same frequency. The MUSIC algorithm uses multiple parameters for window size ( $n_{ws}$ ), overlap between windows ( $n_{\text{shift}}$ ), number of detectable frequencies ( $n_f$ ) and frequency resolution ( $n_{\text{FFT}}$ ). Various combinations of these parameters were tested for GAM detection, and best results were generally obtained with  $n_{ws} = 32$ ,  $n_{\text{shift}} = 16$ ,  $n_w = 6$ ,  $n_f = 1$  and  $n_{\text{FFT}} = 8192$ . Generally, the SWFFT method is much faster to compute and manages to detect the GAM with slightly better signal to noise ratio.

This is contrary to Tore Supra results where the MUSIC algorithm proved superior for GAM detection [130]. All experimental GAM measurements presented in this work have been obtained using the conventional SWFFT approach.

## 6.4 Cross-correlation techniques

This section introduces two cross-correlation techniques which are used to investigate GAM correlation and propagation in Sec. 9.3. In the first method, which for example was used to study GAM propagation at the TEXTOR tokamak [56], the spatio-temporal cross-correlation between a radially fixed and a radially moving channel is calculated. In the second method, measurements from two fixed positions are used to calculate a local estimate of the wavenumber and frequency spectrum [128].

### 6.4.1 Spatio-temporal cross-correlation

In this method, two channels are used to measure plasma fluctuations, one of which is at a fixed radial position while the other moves radially. In TEXTOR, for example, a stationary and a mobile Langmuir probes were used [56]. In ASDEX Upgrade, the Doppler reflectometer setup can be modified to allow simultaneous measurements from the same poloidal angle [125]. One channel probes the plasma with a fixed frequency, i.e. at a fixed radial position, while the other channel increases its probing frequency stepwise to scan the accessible radial region. During each of these steps, the Doppler shift time series  $f_D(t)$  is computed as described in Sec. 6.2.

After bandpass filtering the signal from both channels in the broad range of expected GAM frequencies between 5 and 30 kHz, which lessens the effect of any non-GAM fluctuations, the cross-correlation  $P_{12}(\rho_{\text{pol}}, \tau_l)$  between the Doppler shift time series from channels 1 and 2, with time lag  $\tau_l = t_2 - t_1$ , is calculated for each radial position  $\rho_{\text{pol}}$  of channel 2. The normalised cross-correlation function between two signals  $x(t)$  and  $y(t)$  is defined as

$$P_{XY}(\tau_l) = \frac{1}{\sigma_x \sigma_y} \int \tilde{x}(t) \tilde{y}(t + \tau_l) dt. \quad (6.5)$$

Here, the tilde signifies the difference from the mean value of  $x(t)$  and  $y(t)$ ,  $\sigma_x$  and  $\sigma_y$  are the standard deviations of the signals. In discrete signal analysis, the integration is replaced by a sum over consecutive timesteps. An example plot of  $P_{12}(\rho_{\text{pol}}, \tau_l)$  is

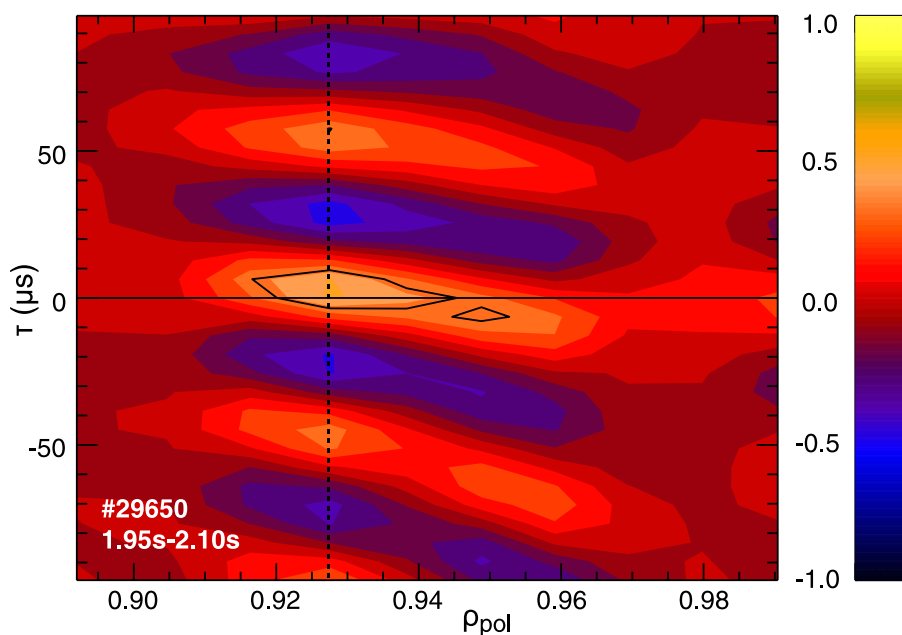


Figure 6.7: Cross-correlation  $P_{12}(\rho_{\text{pol}}, \tau_l)$  between  $f_D$  time series obtained from Doppler measurements by a fixed channel at  $\rho_{\text{pol},1} \approx 0.927$  and a radially sweeping channel in the range  $0.89 < \rho_{\text{pol},2} < 0.99$  during ASDEX Upgrade limiter discharge #29650,  $t = 1.95\text{--}2.10$  s.

show in Fig. 6.7. Here, the fixed channel is at a radial position of  $\rho_{\text{pol},1} \approx 0.927$ . The maximum for the cross-correlation is found, as expected, close to zero time delay and no radial separation between the two channels. When the sweeping channel is further away from the fixed channel, the correlation decreases. This shows the radial width over which the GAM is coherent. Similarly, when looking at the time-delay axis, the correlation alternates between positive and negative values, where the lag between two maxima corresponds to the period of the GAM oscillation. In this example, an inclination is visible in the regions of high correlation: when the sweeping channel is further inside the plasma than the fixed channel, the correlation maximum is found at  $\tau_l > 0$ , whereas the maximum shifts to  $\tau_l < 0$  when the sweeping channel is radially outwards from the fixed position. Similar observations were made in TEXTOR [56] and can be interpreted as evidence of radial GAM propagation, in this example in the radially inward direction.

## 6.4.2 Two-point correlation method

In 1982, Beall *et al.* described a method for the estimation of wavenumber and frequency spectra from measurements made by pairs of fixed probes, which they used to study drift-wave turbulence [128]. The motivation was to find a way to allow the computation of wavenumber spectra from experimental data, without the need of simultaneous fluctuation measurements in many separate points, since this would usually increase the cost of the experimental apparatus and could also interfere with the observations for invasive measurement techniques such as Langmuir probes.

In this two-point correlation method, only one pair of fixed probes would be necessary, or, in the case of this work, one pair of Doppler channels with fixed probing frequencies. The cross-phase  $\theta(\omega)$  between the signals  $x_1(t)$  and  $x_2(t)$  from the two channels is computed from their complex cross-spectrum  $H(\omega)$ :

$$\theta(\omega) = \tan^{-1}(H(\omega)), \quad \text{where} \quad H(\omega) = |\hat{x}_1^*(\omega)\hat{x}_2(\omega)|. \quad (6.6)$$

Here, the hat denotes the Fourier transform and the star the complex conjugate.  $\theta(\omega)$  is then used to calculate the local wavenumber  $K(\omega)$ :

$$K(\omega) = \frac{\theta(\omega)}{\Delta r}, \quad (6.7)$$

where  $\Delta r$  is the radial separation between the two channels. The distance between the channels determines the wavenumber range that can be probed:

$$-\frac{\pi}{\Delta r} < K(\omega) < \frac{\pi}{\Delta r}. \quad (6.8)$$

The wavenumber range is divided into  $N$  intervals  $[K_n, K_n + \Delta K]$  of width  $\Delta K = 2\pi/(N\Delta r)$ . Ensemble averages over  $M$  partitions of the data are used to compute estimates of the local wavenumber and frequency spectrum  $S_l(\omega, K_n)$  by summing over the sample power  $S_j(\omega)$  for all points within each wavenumber interval:

$$S_l(\omega, K_n) = \frac{1}{M} \sum_{j=1}^M S_j(\omega) I_{[0, \Delta K]} [K_n - K_j(\omega)] \quad (6.9)$$

Here,  $I_{[0, \Delta K]}(x)$  is an indicator function, which is 1 for  $0 < x < \Delta K$  and 0 otherwise. From this spectrum, information about the average wavenumber and frequency of

the plasma fluctuations can be extracted.

# Chapter 7

## GAM frequency scaling

This chapter presents results from the experimental investigation of GAM frequency scaling in ASDEX Upgrade. Particular focus is placed on the plasma elongation  $\kappa$ , as previous experiments in non-circular plasmas at ASDEX Upgrade [60, 65] and other devices [66, 69] indicate significant deviations from the basic GAM frequency as predicted by Winsor. Section 7.1 presents the shape-scan experiments that are used for the scaling analyses. Some theories suggest that, in addition to the plasma elongation  $\kappa$  and the safety factor  $q$ , other geometrical parameters such as the Shafranov shift gradient  $\Delta'$ , radial elongation gradient  $s_\kappa$  and inverse aspect ratio  $\epsilon$  impact the GAM frequency scaling. Experimentally, these quantities are somewhat interlinked and difficult to vary independently. Therefore, the focus is put on the leading terms with the largest expected impact,  $\kappa$  and  $q$ . Section 7.2 compares the experimental shape-scan results to a wide range of theoretical predictions. Section 7.3 addresses the possible influence of other plasma parameters on the GAM frequency scaling. The chapter concludes with a summary and discussion of the findings in Sec. 7.4. This chapter contains and expands on results previously published in Ref. [78].

### 7.1 Description of experiments

To study the influence of the plasma shape (cf. Sec. 4.4) on the GAM, a set of special shape-scan experiments were performed. During a single deuterium plasma discharge, the boundary elongation  $\kappa_b$  (i.e. the value of  $\kappa$  at the last closed flux surface) was substantially varied, while other parameters such as the safety factor  $q$  were kept as constant as possible. Figure 7.1 (bottom) shows a case in which

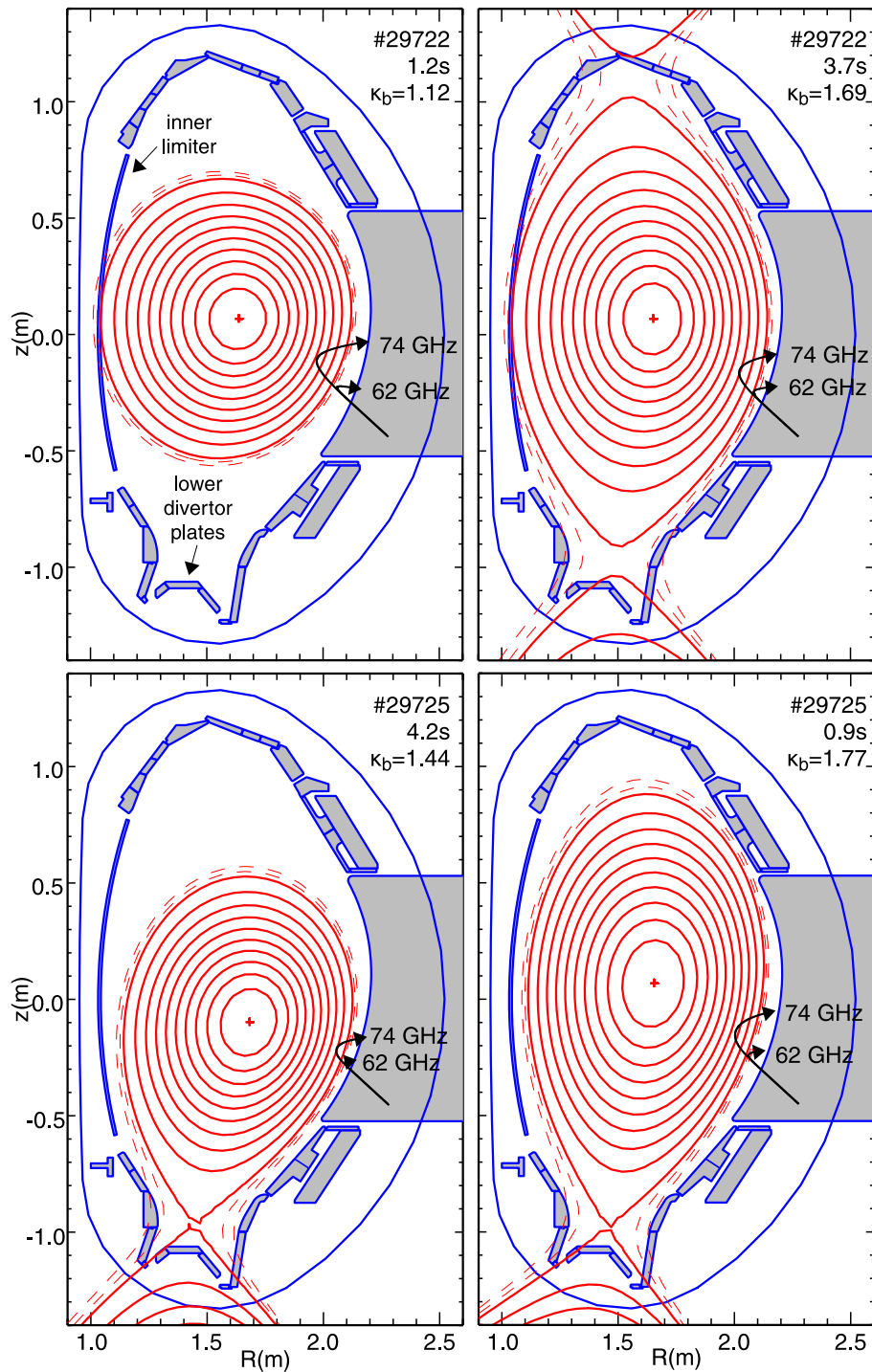


Figure 7.1: Plasma shape during beginning and ending of two shape-scan discharges. Top: Limiter discharge #29722. Bottom: Divertor discharge #29725. The red surfaces indicate constant poloidal flux  $\Psi_{\text{pol}}$ . The black lines indicate the probing range and measurement locations of the Doppler reflectometer.

a lower single divertor configuration was modified from  $\kappa_b = 1.77$  to  $\kappa_b = 1.44$ . The counterpart is shown in Fig. 7.1 (top), where a nearly circular limiter plasma ( $\kappa_b = 1.12$ ) is stretched to a higher elongation ( $\kappa_b = 1.69$ ), nearly resulting in a double null configuration (cf. Fig. 4.4). Previous ASDEX Upgrade experiments [65] that looked into the role of the elongation featured mainly low- $\kappa$  limiter discharges and high- $\kappa$  divertor discharges, leaving a gap in the range of intermediate elongation and no overlap between limiter and divertor data. This new set of discharges closes that gap, making it possible to separate the influence of both the plasma elongation as well as the configuration, e.g. the presence of an X-point null field. Figure 7.1 also overlays beam traces computed using the TORBEAM code showing the path of the beam's central ray for X-mode microwaves at the lowest and highest probe frequencies that are used in these experiments. The corresponding launch/receiver antennas are below the midplane and tilted upward by  $42.5^\circ$ , as pictured in Fig. 5.6.

Figure 7.2 shows time traces of typical plasma quantities from one of the limiter discharges. Using control coils, the plasma boundary elongation  $\kappa_b$  is steadily increased throughout the discharge, from 1.1 to approximately 1.7. At the same time, the plasma current  $I_p$  is increased from 0.6 to 1.0 MA in order to maintain the edge safety factor at a constant value of  $q_{95} \approx 4$ . Using feed forward gas fuelling, it was also attempted to keep the line-averaged density at a constant level of  $n_e \approx 2.5 \times 10^{19} \text{ m}^{-3}$  in order to maintain the Doppler measurements in the same radial region, but some small variation between  $2$  and  $3 \times 10^{19} \text{ m}^{-3}$  could not be avoided. The edge density near the separatrix or last closed flux surface was typically close to  $n_{\text{edge}} \approx 0.5 \times 10^{19} \text{ m}^{-3}$ . In this discharge the magnetic field strength was kept constant at  $B = -2.4 \text{ T}$  and a moderate electron cyclotron resonance heating power of  $0.4 \text{ MW}$  was applied. These values of magnetic field and density were chosen to allow for X-mode Doppler measurements in the edge region of the plasma, where GAMs are typically observed during L-mode discharges at ASDEX Upgrade. Specifically, GAMs are usually detected inwards from the region of the radial electric field minimum at the plasma edge toward the  $n_e$  pedestal top, and never outside of the separatrix or last closed flux surface. The location and range of GAM measurements, i.e. slightly below the midplane on the low field side edge, can also be seen in Fig. 7.1. The poloidal angle of beam incidence  $\theta$ , as well as the poloidal plasma location, remain roughly constant in all configurations.

Figure 7.3 shows typical edge plasma radial profiles of electron temperature  $T_e$ , density  $n_e$  and safety factor  $q$  during low- and high-elongation phases of a limiter

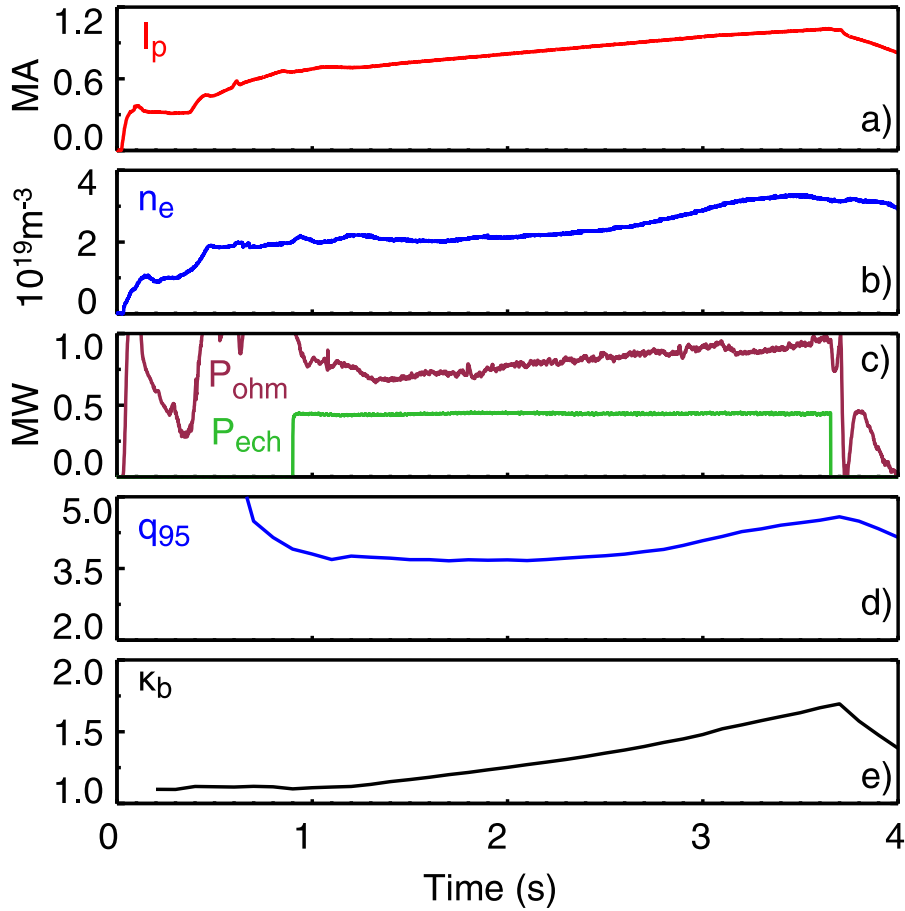


Figure 7.2: Time traces of AUG shape-scan discharge #29722, showing the evolution of a) plasma current  $I_p$ , b) central line averaged density  $n_e$ , c) Ohmic and ECRH heating power, d) edge safety factor  $q_{95}$  and e) boundary elongation  $\kappa_b$ .  $B_t$  was kept constant at  $-2.4$  T.

discharge. The radial range in which GAMs are detected is slightly wider in the case of low boundary elongation.

To study the radial structure of the GAMs, the Doppler probing frequency is stepped, with one radial sweep consisting of 10–13 steps separated by 1 GHz, each lasting 15 ms. The measurement locations were reconstructed using fitted density profiles from the profile reflectometer and lithium-beam diagnostics. The electron temperature  $T_e$ , which is important for comparison with the theoretical models, was measured with the Thomson scattering and electron cyclotron emission (ECE) diagnostics. Experimental measurements of the ion temperature were not available in all cases and have been scaled from similar discharges. From previous experiments,

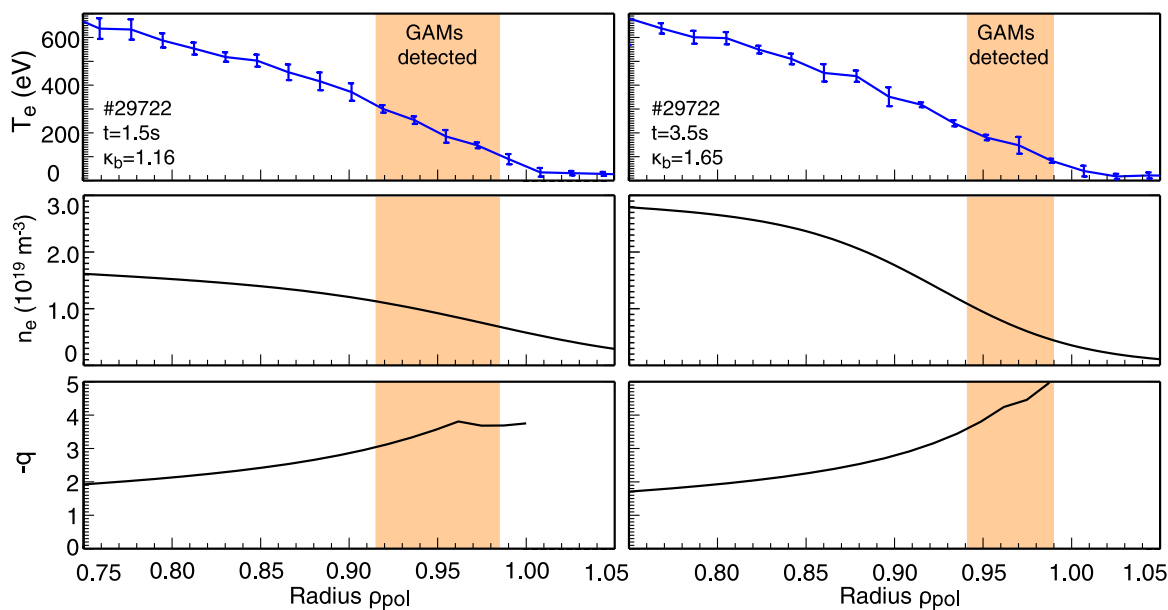


Figure 7.3: Radial profiles of electron temperature  $T_e$  (top), density  $n_e$  (middle) and safety factor  $q$  (bottom) in limiter discharge #29722. Left:  $t = 1.5$  s,  $\kappa_b = 1.16$ . Right:  $t = 3.5$  s,  $\kappa_b = 1.65$ . The radial region in which GAMs were detected is highlighted.

for measurements towards the plasma pedestal top,  $T_i \approx T_e$  was assumed, whereas in divertor discharges closer towards the separatrix, the ion temperature can rise to  $T_i \approx 1.2T_e$  [131].

For the comparison of GAM frequency and amplitude measurements to theoretical models, a database consisting of 59 radial sweeps, taken during three shape-scan discharges, was evaluated. During each radial sweep the strongest detected GAM peak (or none, if no clear GAM peak could be determined) is used in the analysis. The range of plasma boundary elongation in the database is  $1.13 < \kappa_b < 1.78$ , GAMs are detected in the radial range of  $0.92 < \rho_{\text{pol}} < 0.99$  at densities of  $0.6 \times 10^{19} \text{ m}^{-3} < n_e < 1.3 \times 10^{19} \text{ m}^{-3}$ ; the local safety factor  $q$  varies between 3 and 5.

## 7.2 Comparison to existing models

In this section, GAM frequency measurements from the previously described shape-scan experiments are compared to a number of electrostatic models: the original simple fluid model by Winsor (Sec. 7.2.1); a heuristic scaling by Conway, which

accounts for the influence of plasma elongation (Sec. 7.2.2); a fluid model by Angelino, which also accounts for plasma elongation (Sec. 7.2.3); a gyrokinetic model by Sugama and Watanabe (Sec. 7.2.4); and a gyrokinetic model by Gao, which includes additional geometric quantities (Sec. 7.2.5).

### 7.2.1 Comparison with Winsor's basic scaling

The derivation of Winsor's original prediction [50] for the GAM frequency  $f_{\text{GAM}}$  from a fluid model for a circular plasma approximation was discussed in Sec. 3.4. In this model, the GAM frequency contains as parameters only the sound velocity  $c_s$ , the major radius  $R_0$  and the safety factor  $q$ :

$$\omega_{\text{GAM}} = 2\pi f_{\text{GAM}} = \frac{c_s}{R_0} \sqrt{2 + q^{-2}}. \quad (7.1)$$

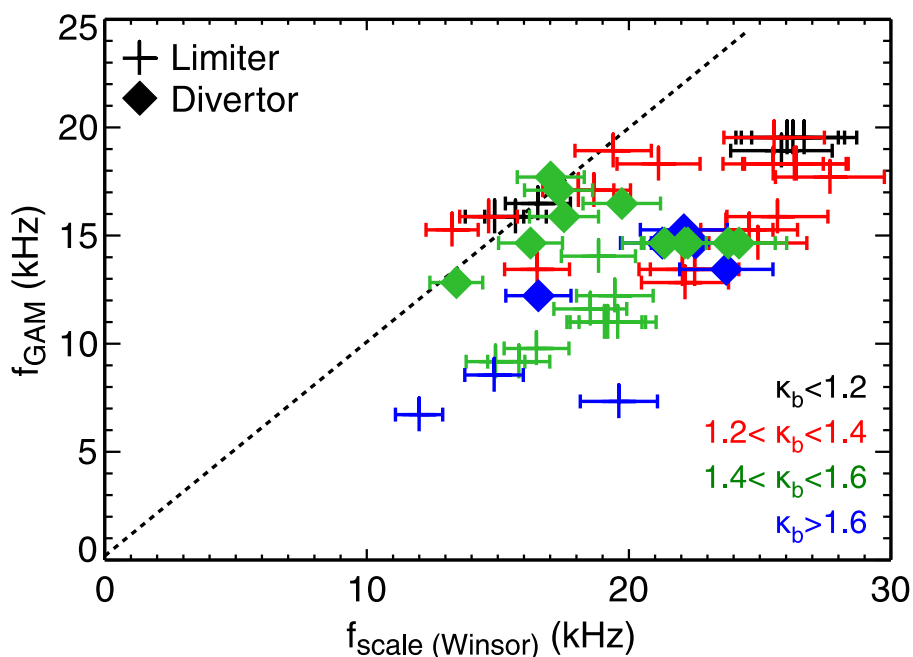


Figure 7.4: Comparison of the experimental results ( $f_{\text{GAM}}$ ) with Winsor's scaling law ( $f_{\text{scale}}$ ). All points refer to GAMs in a range of radial positions  $0.91 < \rho_{\text{pol}} < 0.99$  and safety factor  $3.5 < q_{95} < 5$ . The degree of elongation is indicated by colour. Crosses: GAMs from limiter discharges. Diamonds: GAMs from divertor discharges.

Figure 7.4 compares the experimentally observed GAM frequency as a function of the frequency predicted by Winsor's scaling,  $f_{\text{scale}}$ . In this and the following figures, GAM data from both limiter and divertor discharges is presented together,

represented by plus and diamond symbols, respectively. The symbol colour signifies the boundary elongation corresponding to each GAM measurement. The main sources of uncertainty for  $f_{\text{scale}}$  are the errors in  $T_e$  and  $T_i$  (and therefore the sound velocity) and in the extraction of the GAM frequency from the spectrum. The errors in the temperatures consist mostly of contributions due to uncertainties in the ECE measurements and uncertainty in the measurement position due to the fitted density profile. These are estimated to be of the order of 15%. The uncertainty for the safety factor  $q$  is determined by the steepness of the  $q$  profile. Example profiles can be seen in Fig. 7.3. For plasmas with low boundary elongation  $\kappa_b$ , the  $q$  profile is usually relatively flat and small uncertainties in the radial coordinate only translate to minimal variation in  $q$ . For elongated plasmas, especially in divertor configuration, the  $q$  profile is steeper in the edge and an error of up to 5% is expected.

The error in the measured GAM frequency is dictated by the frequency resolution due to the chosen FFT parameters and here is approximately 0.3 kHz, which is below 5% for all GAM measurements in the database. Since an error of this magnitude is comparable to the symbol size, it is not pictured in Fig. 7.4.

It can be seen that Winsor's scaling generally overestimates  $f_{\text{GAM}}$ . Especially for GAMs in plasmas with high  $\kappa_b$ , i.e. in typical ASDEX Upgrade lower single null configuration, the discrepancy becomes large. This result is expected from earlier AUG results [60,65] and supports the need for models incorporating the influences of plasma geometry. In this case, limiter and divertor data fall in the same range and show no systematic differences.

## 7.2.2 Comparison with Conway's heuristic model

In order to account for the observed deviation from Winsor's model in elongated plasmas, Conway *et al.* tested a number of possible empirical scaling models incorporating local elongation  $\kappa$ , boundary elongation  $\kappa_b$ , local safety factor  $q$ , edge safety factor  $q_{95}$  and inverse aspect ratio  $\epsilon$  [65]. The best agreement to the experimental data, consisting largely of low- $\kappa_b$  limiter discharges and high- $\kappa_b$  divertor discharges, was found for

$$\omega_{\text{GAM}} = \frac{c_s}{R_0} 4\pi \left( \frac{1}{1 + \kappa_b} - \epsilon \right). \quad (7.2)$$

This empirical model was found to give good agreement for GAMs in the edge

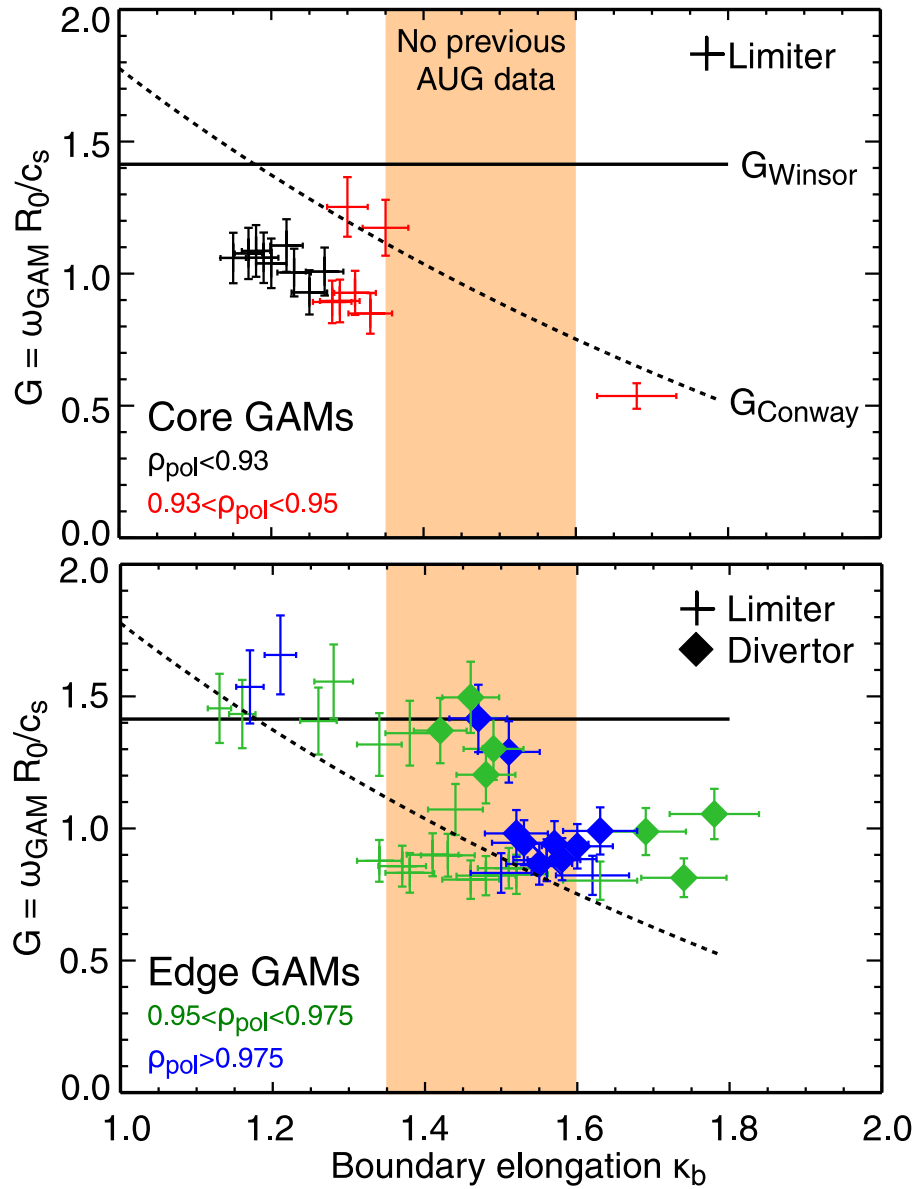


Figure 7.5: Scale factor  $G = \omega_{\text{GAM}} R_0 / c_s$  as function of the plasma boundary elongation  $\kappa_b$  for the whole data set with  $3.5 < q_{95} < 5$ , compared to the Conway and Winsor models.

of elongated plasmas, but does not reduce to Winsor's scaling for  $\kappa_b \rightarrow 1$ . In this particular model the influence of  $q$  is not accounted for, as its effect on the experimental GAM frequency was not found to be strong.

The influence of the boundary elongation on the GAM frequency in the new set of shape-scan discharges used throughout this work can be seen in Fig. 7.5. It shows the scale factor  $G$ , which was determined by measuring the GAM frequency and normalizing to  $c_s/R_0$  in order to remove the dependence of  $f_{\text{GAM}}$  on the local plasma temperature. Variations in  $q$  were neglected for this figure.  $G = \omega_{\text{GAM}}R_0/c_s$  was then plotted against the plasma boundary elongation at the corresponding time in the discharges. Highlighted is the area of intermediate plasma elongation, in which no previous experimental data was available. The dataset was separated into GAMs in the plasma core, i.e.  $\rho_{\text{pol}} < 0.95$ , and GAMs in the plasma edge.

In both sets, a general trend for lower GAM frequencies at higher plasma elongations can be observed, however there are some key differences. Core GAMs are almost exclusively observed at low plasma boundary elongation in limiter plasmas, and are shown to mostly have a scale factor below what would be expected both according to the classical Winsor scaling and the heuristic model by Conway.

For edge GAMs in limiter plasmas, the scale factor is close to the Winsor scaling at low elongation, but overall follows the Conway scaling as  $\kappa_b$  increases. For divertor GAMs, which are generally only seen in the plasma edge, there is also a tendency for lower GAM frequency at higher  $\kappa_b$ . However,  $G$  is higher than estimated based on the Conway scaling, in particular for GAMs in the range  $0.95 < \rho_{\text{pol}} < 0.975$ .

Figure 7.6 shows a direct comparison for core and edge GAMs of the measured GAM frequency  $f_{\text{GAM}}$  with the predicted GAM frequency  $f_{\text{scale}}$  from Conway's scaling. For better visibility there are no error bars included in this and the following figures. As the uncertainties in the temperatures are the strongest influence on the errors in all frequency scalings, the error bars in Fig. 7.4 may be used as a reference.

In comparison to Winsor's scaling, the Conway model yields better agreement to the present data. However, the systematic deviations for core limiter GAMs and divertor GAMs need to be considered. These effects which are observed here may be related to the radial GAM structure and the selection of the GAM peaks: as will be discussed in Sec. 9.2, depending on the discharge scenario the GAM structure can alter significantly. In low- $\kappa_b$  limiter discharges, GAMs are found both in the core and in the edge simultaneously, either as a continuum with radially changing frequency, or as two neighbouring plateaus over which the frequency is locked. However, in

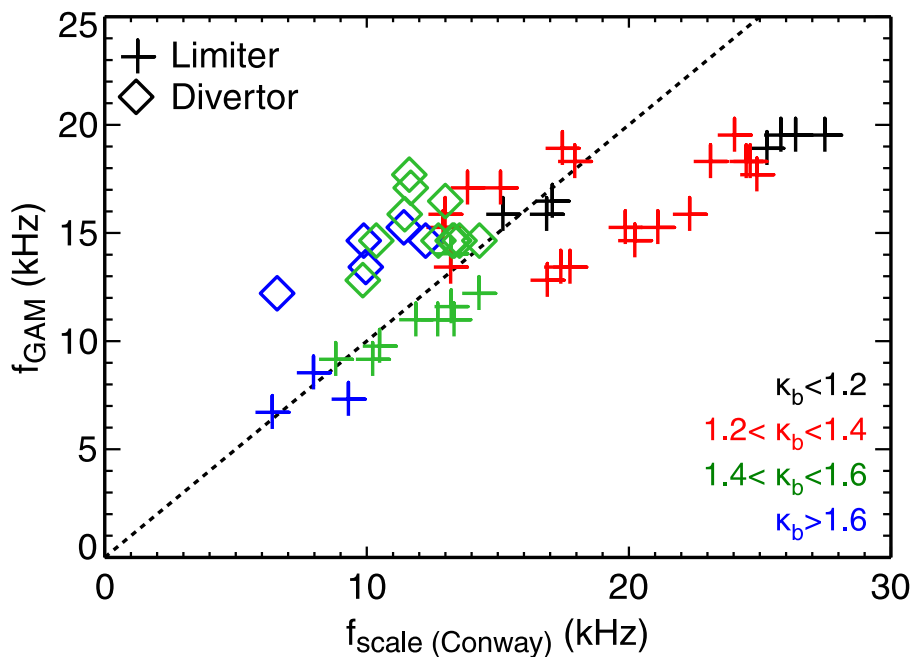


Figure 7.6: Comparison of the experimental results  $f_{\text{GAM}}$  with Conway's scaling law  $f_{\text{scale}}$ .

each radial sweep only the strongest GAM was selected, which is typically found near the core for the continuum scenario, but in the outer plateau for the case of two locked GAMs.

Therefore, the lower than expected GAM frequency may not just depend on the radial position, but the overall structure. For divertor discharges, the GAM is almost always locked to a single frequency over a certain radial width. For these calculations, the GAM position and local temperature is again taken from the maximum peak. However, the GAM extends further inside. If the innermost position of the GAM plateau were used to predict the frequency scaling, the divertor points in Fig. 7.5 would shift downwards (or to the right in Fig. 7.6), and the agreement would be improved.

### 7.2.3 Comparison with Angelino's fluid model

In order to establish an analytical relation between GAM properties and the plasma geometry, in 2008 Angelino *et al.* derived a prediction for the GAM frequency from a fluid model [73]. The derivation takes the geometry into account through the local

elongation  $\kappa$  [132]:

$$\omega_{\text{GAM}} = \frac{v_{T_i}}{R_0} \sqrt{(\tau + \gamma_i) \left[ \frac{8}{3 - 2\kappa + 3\kappa^2} + \frac{1}{q^2} \right]} \quad (7.3)$$

Here,  $\tau = T_e/T_i$ , specific heat ratio  $\gamma_i = 1$  and  $v_{T_i} = \sqrt{T_i/m_i}$ . Angelino uses the local elongation  $\kappa$  instead of the boundary elongation  $\kappa_b$ . For the comparison,  $\kappa$  is obtained from the CLISTE equilibrium code [133]. For  $\kappa \rightarrow 1$ , the formula reduces to Winsor's scaling (Eq. 3.10).

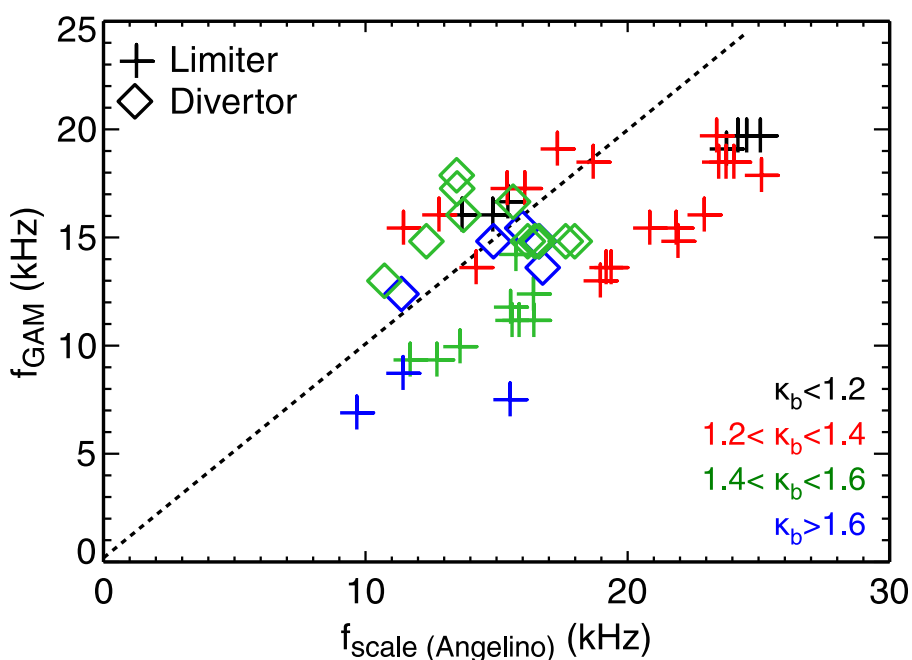


Figure 7.7: Comparison of the experimental results ( $f_{\text{GAM}}$ ) with Angelino's scaling law ( $f_{\text{scale}}$ ).

The comparison of measured GAM frequencies to Angelino's scaling are shown in Fig. 7.7. The agreement is similar to that obtained with Conway's heuristic model. In general, the scaling fits the data much better than Winsor's simplified fluid model, but there are large discrepancies for limiter GAMs at low  $\kappa$ , towards the plasma core. The predicted GAM frequency lies above the measurements. However, Angelino's scaling appears to give a better fit for GAMs in divertor plasmas.

### 7.2.4 Comparison with Sugama and Watanabe's gyrokinetic model

GAMs have also been theoretically described using an electrostatic gyrokinetic approach. Here, Sugama and Watanabe derived a prediction of the GAM frequency from a gyrokinetic model under the assumption of large aspect ratio and circular plasma shape, i.e.  $\kappa = 1$  [72, 134]:

$$\omega_{\text{GAM}} = \frac{v_{T_i}}{R_0} \sqrt{\left(\frac{7}{4} + \tau\right) \left[1 + \frac{2(23 + 16\tau + 4\tau^2)}{q^2(7 + 4\tau)^2}\right]}. \quad (7.4)$$

While this model neglects the plasma elongation and other geometric quantities, it is often used for validation in other experimental [69] or numerical [135] work, and therefore a comparison to the dataset of this thesis is worthwhile.

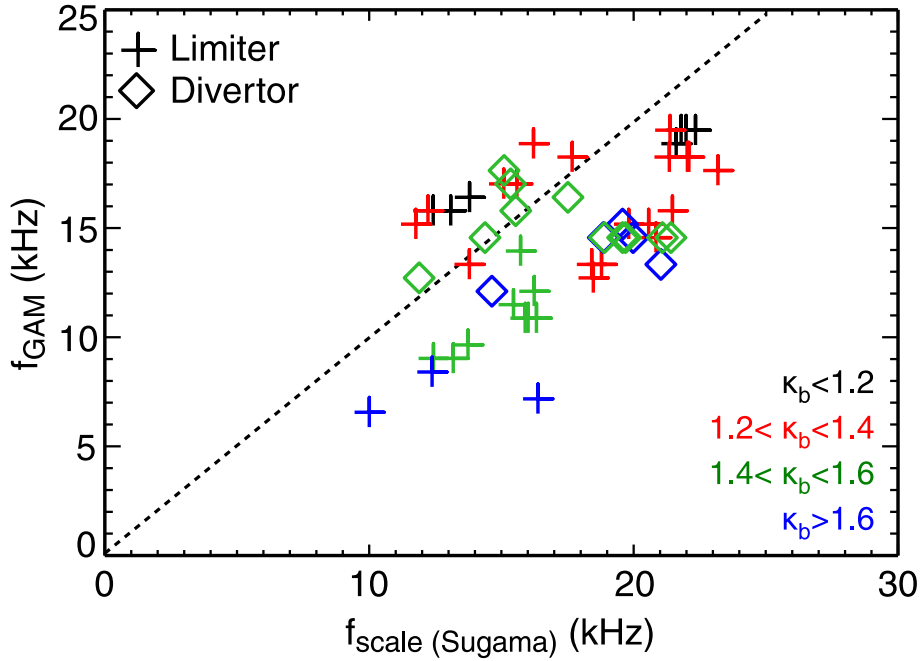


Figure 7.8: Comparison of the experimental results ( $f_{\text{GAM}}$ ) with Sugama and Watanabe's scaling law ( $f_{\text{scale}}$ ).

Figure 7.8 shows the results of the comparison between the Sugama-Watanabe scaling and the experimental data. As expected for a model that does not incorporate the plasma elongation, the predicted frequency is mostly higher than the measurements. GAMs in nearly circular limiter discharges with  $\kappa_b < 1.2$ , i.e. close

to the conditions for which the model was intended, appear to be described well. The overall agreement is improved in comparison with Winsor's scaling law, however it is not as good as Conway's heuristic model or Angelino's fluid model.

### 7.2.5 Comparison with Gao's gyrokinetic model

A more involved approach based on an electrostatic gyrokinetic model and incorporating the effects of finite orbit drift width (ODW) was derived by Gao [71, 136, 137] between 2009 and 2011. In contrast to the approaches of Angelino or Sugama and Watanabe, Gao includes a larger number of geometric parameters. Non-linear effects are not included. In the small ODW limit the GAM frequency is given by

$$\omega_{\text{GAM}} = \frac{v_{T_i}}{R_0} \sqrt{\left(\frac{7}{4} + \tau\right) \left(\frac{2}{\kappa^2 + 1}\right) \left(1 - \frac{s_\kappa}{2} \frac{7 + 2\tau}{7 + 4\tau}\right)} \left[1 - \epsilon^2 \frac{9\kappa^2 + 3}{8\kappa^2 + 8} - \Delta'^2 \frac{\kappa^2}{4\kappa^2 + 4} + \epsilon \Delta' \frac{4\kappa^2 + 1}{4\kappa^2 + 4} + \frac{(23 + 16\tau + 4\tau^2)(\kappa^2 + 1)}{2q^2(7 + 4\tau)^2}\right], \quad (7.5)$$

with  $\tau = T_e/T_i$ , inverse aspect ratio  $\epsilon = r/R_0$ , Shafranov shift gradient  $\Delta'$  and the radial derivative of the elongation  $s_\kappa \approx (\kappa - 1)/\kappa$ . Again, the local elongation  $\kappa$  is used. Typical values for  $\Delta'$  in the region of GAM activity are between  $-0.4$  and  $-0.2$  (see also Fig. 4.5). Therefore the contribution of the Shafranov shift gradient towards the GAM frequency is of a similar order of magnitude as the inverse aspect ratio, both of which decrease  $\omega_{\text{GAM}}$  by about 10% for typical values of  $\kappa$ .

The comparison of the experimental data with the Gao scaling in Fig. 7.9 shows some improvements. While in general the experimental frequency lies above the theoretical prediction, the discrepancy between edge and core GAMs in limiter discharges mostly disappears, and the deviation from divertor discharges is less severe. Overall, Gao's scaling exhibits the least scatter between various radial regions or plasma geometries and seems the closest approach so far to presenting a unified picture.

Due to the linear derivation of Gao's equation, the predicted frequency can be understood to give only a lower boundary, whereas non-linear effects may also play a role. The results show GAM frequencies which are always shifted upward with respect to the linear theoretical prediction. This seems consistent with the nonlinear gyrokinetic prediction, according to which the nonlinear frequency shift is always positive [138, 139], whereas nonlinear MHD predictions give both upshifts

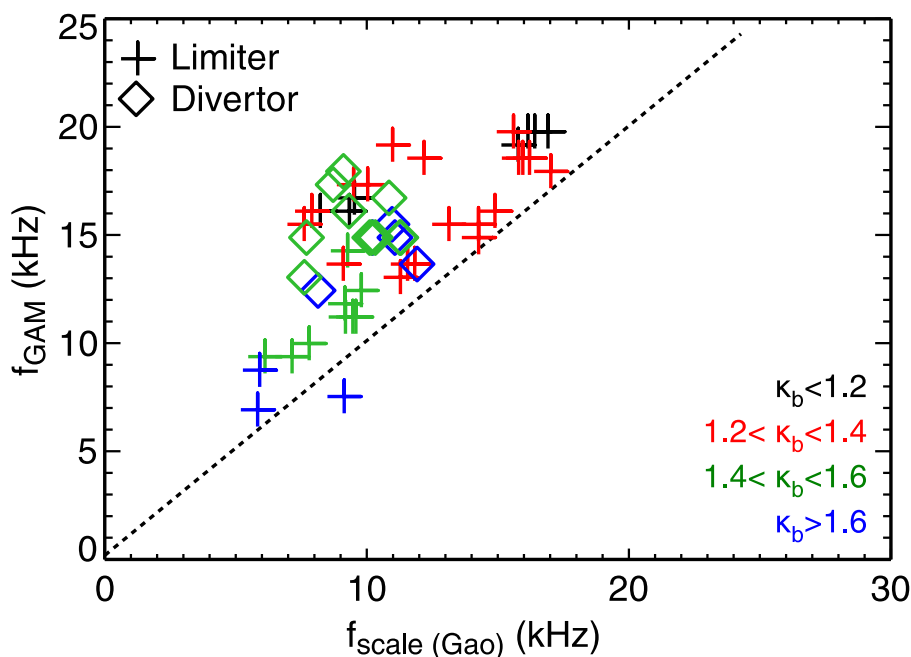


Figure 7.9: Comparison of the experimental results ( $f_{\text{GAM}}$ ) with the Gao scaling law ( $f_{\text{scale}}$ ).

and downshifts depending on the phase delay between the nonlinear force and the GAM oscillation [140].

### 7.3 Further influences on the GAM frequency

Apart from the plasma quantities that were investigated in conjunction with the scaling models from the previous section, other possible influences on GAM properties have been proposed:

- Plasma impurities: due to erosion processes in the plasma vessel, it is unavoidable that a certain level of impurities will be present in any fusion plasma. This can be expressed by the effective charge  $Z_{\text{eff}} = (\sum n_s Z_s^2) / (\sum n_s Z_s)$  which is calculated from all species with density  $n_s$  and charge  $Z_s$ . The effective charge can be measured using spectroscopy. The effect of impurities on GAM frequency and damping were studied by Guo *et al.* [74]. For an exact analysis, each impurity's density, charge, mass and temperature would need to be considered. Overall, impurities are found to decrease the GAM frequency, with higher effective charge leading to stronger reduction. Figure 7.10 shows an ex-

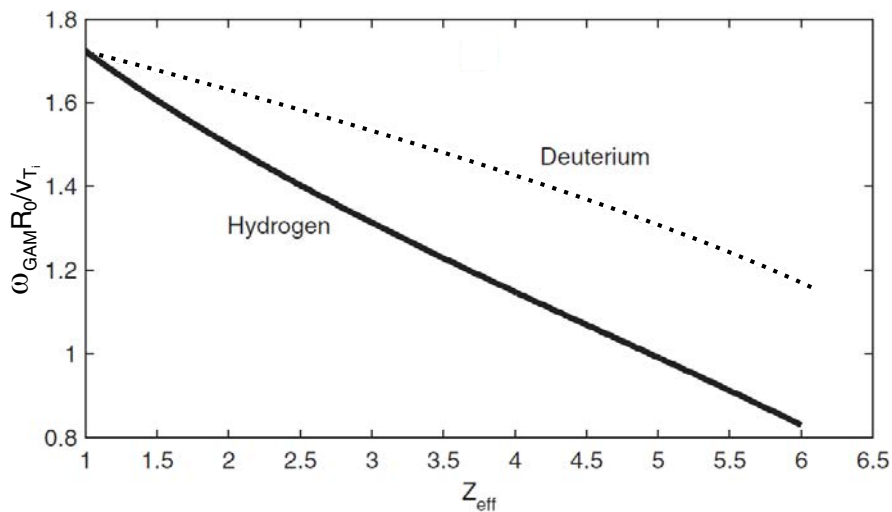


Figure 7.10: Normalized GAM frequency  $\omega_{\text{GAM}}R_0/v_{T_i}$  as a function of effective charge  $Z_{\text{eff}}$  for carbon impurities in hydrogen and deuterium plasmas at  $q = 3$ . Adapted from Ref. [74].

ample case for carbon impurities in hydrogen and deuterium plasmas at  $q = 3$ , indicating that the presence of impurities has a stronger influence on the GAM frequency in hydrogen plasmas than in deuterium plasmas. Calculations for experiments at Tore Supra, where  $Z_{\text{eff}}$  can reach 2.5, showed that the impurity content might contribute variations of up to 10% [69]. In typical ASDEX Upgrade edge scenarios,  $Z_{\text{eff}}$  is not expected to exceed 1.5. For such values of  $Z_{\text{eff}}$  in deuterium plasmas, only very small corrections can be expected.

- Electromagnetic effects: while the investigated models are based on electrostatic approaches, recent modelling [141] suggests that higher plasma  $\beta$  can lead to lowered GAM frequencies. This has been observed in an ASDEX Upgrade discharge, where a 100% increase in  $\beta$  is observed with the onset of ECR heating. The GAM frequency scaling is about 10% lower than would be expected following the increase of the local plasma temperature due to the heating, while other influences such as  $\kappa_b$  or  $q$  remain constant. For the discharges used in this database, however,  $\beta$  only changes by less than 5% in limiter discharges in all cases, while in a few extreme divertor cases at low elongation  $\beta$  increased only by a maximum of 50%. Therefore, electromagnetic effects are not expected to play a significant role for the majority of the database, and may decrease the frequency for a limited number of low- $\kappa$

divertor GAMs, but within the error bars given by the temperature measurements. As electromagnetic models are only recently being investigated, further comparison is beyond the scope of this work.

## 7.4 Discussion

This chapter presents experimental results from Doppler reflectometry measurements on a number of shape-scan experiments in order to study the influence of plasma geometry on the properties of the geodesic acoustic mode. The measurements are compared to heuristic and various theory-based models. It is confirmed that the GAM frequency prediction by Winsor's simplified fluid model shows inaccuracies, as it generally overestimates the GAM frequency, with strong deviations for edge GAMs in elongated tokamak experiments. A comparison with Conway's heuristic model, which was based on a set of low- and high-elongation discharges, yields better agreement, even with the inclusion of new experimental points from limiter discharges at medium plasma elongation. The GAM frequency for core GAMs is generally overestimated, however. More involved theory-based models attempt to account for the observed effects: a fluid model derived by Angelino, which incorporates the effect of plasma elongation  $\kappa$ , yields some improvement on Winsor's scaling. However, large discrepancies are found for low- $\kappa$  limiter plasmas. The overall agreement with the experimental data is still better for the heuristic model. Angelino's model is nevertheless useful as an estimate of the  $\omega_{\text{GAM}}$ -dependence on  $\kappa$  based on theory. The well-known gyrokinetic prediction by Sugama and Watanabe also improves on Winsor's scaling, but does not account for plasma elongation and is less successful than Conway's or Angelino's models. Gao's gyrokinetic-based scaling is the most rigorous model in its inclusion of plasma geometry parameters such as  $\epsilon$ ,  $s_\kappa$  and  $\Delta'$ . It appears to give a lower boundary prediction of the GAM frequency. The systematic underestimation of  $\omega_{\text{GAM}}$  suggests that non-linear effects may play a significant role and should be considered for an accurate prediction of the GAM frequency, however the possibility of non-linear frequency downshift must also be considered.

The presence of GAMs has been confirmed in many plasma devices (see Sec. 3.4 and the references therein) and an overestimation of GAM frequency by the Winsor model has been confirmed on a number of experiments, among others at AS-

DEX Upgrade [60], DIII-D [61, 66], MAST [67] and Globus-M [68]. The thorough comparison of circular Tore Supra measurements and simulations against various models [69] points to several important influences on the GAM frequency. While the divertor geometry allows for more flexible shaping studies at ASDEX Upgrade, especially in terms of plasma boundary elongation  $\kappa_b$ , the Tore Supra results also stress the importance of impurities, which may account for discrepancies of up to 10% in case of high effective charge  $Z_{\text{eff}} > 2.5$ . In the case of ASDEX Upgrade discharges with  $Z_{\text{eff}} < 1.5$ , impurities are expected to provide a significantly smaller correction. In the comparison of ASDEX Upgrade data with the gyrokinetic model, it is shown that other shaping terms which can be varied only in a limited range, such as the inverse aspect ratio  $\epsilon$  and the Shafranov shift gradient  $\Delta'$  may also play a non-negligible role. Recent results from the spherical Globus-M tokamak only show good agreement with the GAM frequency predicted by the gyrokinetic scaling, highlighting the importance of the terms including the inverse aspect ratio  $\epsilon$ . There are still more parameters that are expected to influence the GAM frequency, but which are not always easily varied and studied. Pressure anisotropy, for example, is expected to impact the GAM frequency [75], but was shown to have little effect at Tore Supra [69]. Toroidal rotation is expected to provide an upshift of the GAM frequency [76, 77] but the magnitude of this effect might be small due to little external momentum input in the plasma discharges investigated here. A relatively strong influence on the GAM frequency can be expected from variations in the isotope mass. ASDEX Upgrade results show an increase of the GAM frequency by 30–40% when the plasma fuelling is changed from deuterium to hydrogen, which matches the change of  $c_s \propto m_i^{-0.5}$ .

In summary, this chapter presents results from a careful study of the geometry dependence of GAM frequency scaling. In particular the influence of plasma boundary elongation  $\kappa_b$  is investigated and documented. Multiple theoretical models manage to reproduce the order of magnitude of the experimentally observed GAM frequency, as well as the generally observed trend towards lower  $f_{\text{GAM}}$  at lower temperatures and higher elongation. The most advanced model by Gao, based on a gyrokinetic description, is shown to give a reliable lower boundary estimate of the GAM frequency. To advance beyond the current level of accuracy in the prediction of GAM frequencies, a comprehensive model incorporating not just the plasma geometry, but also the radial GAM structure (cf. Ch. 9), plasma impurities, toroidal rotation and non-linear effects is needed.



# Chapter 8

## GAM amplitude scaling

While the previous chapter focused exclusively on the behaviour of the GAM frequency during experiments in which the plasma geometry was varied, it is also important to investigate the amplitude of the geodesic acoustic mode. The method for determining the GAM amplitude from Doppler reflectometry measurements at ASDEX Upgrade was introduced in Sec. 6.2.

The GAM amplitude is a measure for the steady-state strength of the GAM and the significance that it can have in the reduction of turbulence through the shear decorrelation mechanism (cf. Sec. 3.3). The stationary GAM amplitude results from a balance between the non-linear drive from the gradient-driven turbulence, damping due to collisional and collisionless processes and the energy transfer between various scales.

Section 8.1 gives a short overview of the range of GAM amplitudes found in the dataset and presents results on the scaling of the GAM amplitude with plasma elongation and variations of safety factor  $q$ . The reason for placing special importance on these parameters is that the GAM frequency, which is strongly impacted by  $\kappa_b$ , and the safety factor have the strongest influence on determining the collisionless damping rates according to the various models which were used in this study. Section 8.2 addresses the GAM drive. Various models for GAM damping, collisional and collisionless, are contrasted and compared in Sec. 8.3. A summary and discussion is given in Sec. 8.4.

## 8.1 GAM amplitude scaling with $\kappa_b$ and $q$

The GAM damping rate is expected to have a substantial impact on the determination of the GAM amplitude. In most models for the collisionless damping rate (cf. Sec. 8.3), the leading terms include the local safety factor  $q$  and the GAM frequency  $\omega_{\text{GAM}}$ . As was established in the previous chapter, the plasma boundary elongation can significantly influence the GAM frequency, an investigation of the GAM amplitude as a function of both  $q$  and  $\kappa_b$  is worthwhile.

Other geometric parameters, such as the inverse aspect ratio  $\epsilon$ , the Shafranov shift gradient  $\Delta'$  or the radial derivative of the elongation  $s_\kappa$  also appear as variables in some models. However, their impact on the overall damping rate is of a lower order than  $q$  or  $\kappa$ , especially within their range of variation in the experiments used for this work.

The GAM amplitude scaling studies were performed using the same set of discharges that was presented in Sec. 7.1. Therefore, the peak-to-peak amplitude  $A_{\text{GAM}}$  can be measured for plasmas with a wide range of elongations,  $1.1 < \kappa_b < 1.8$ . While the experiments were designed to keep the edge safety factor  $q_{95}$  as constant as possible, some variation is still present in the dataset. Additionally, the local safety factor  $q$  is expected to change strongly across small distances in the plasma edge, leading to a range of  $3 < q < 5$  in the dataset.

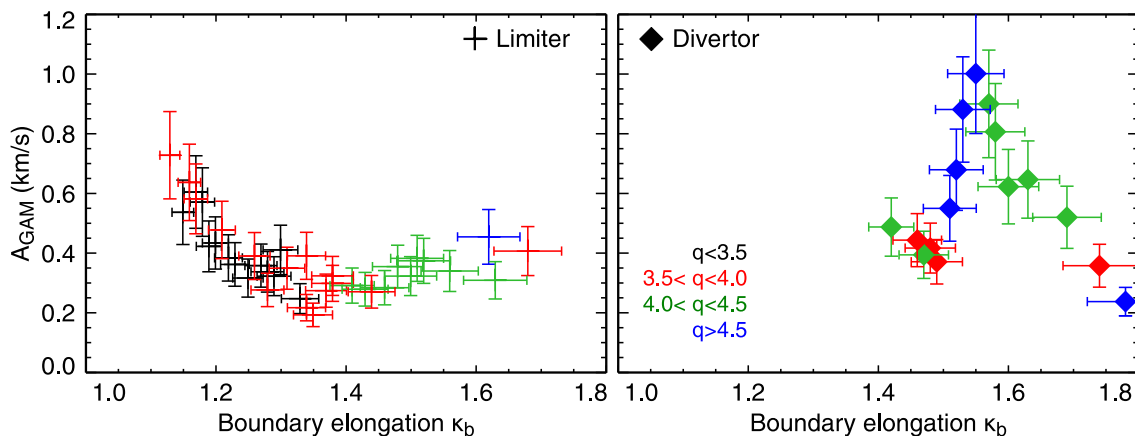


Figure 8.1: GAM amplitude against boundary elongation  $\kappa_b$ , colour-coded for varying local safety factor  $q$ . Left: data from limiter discharges. Right: data from divertor discharges. The drive term  $\nabla T_e / \sqrt{\kappa_b}$  is not kept constant and varies within 4–7.5 keV/m.

As shown in Figs. 8.1 and 8.2, the GAM amplitudes for this set of discharges

fall in the range of 0.2–1.0 km/s. For plasma conditions where GAMs are usually measured, i.e. the edge region of L-mode plasmas, the mean perpendicular plasma velocity is in the range of 2–5 km/s [122]. Hence the GAM can cause a perturbation of the plasma velocity by up to 50%. The ratio between GAM amplitude and frequency is used to estimate the poloidal displacement caused by the GAM, and is of the order  $A_{\text{GAM}}/\omega_{\text{GAM}} \approx 1$  cm, which is comparable to typical values of the poloidal turbulence correlation length in the edge (see [23, 142] and references therein). The radial edge turbulence correlation length is of similar size and is also comparable to the observed radial extent of GAMs in AUG plasmas, as shown in Ch. 9.2.4 and Ref. [65]. The dataset is formed from values taken at the radial position of maximum GAM amplitude in each discharge condition.

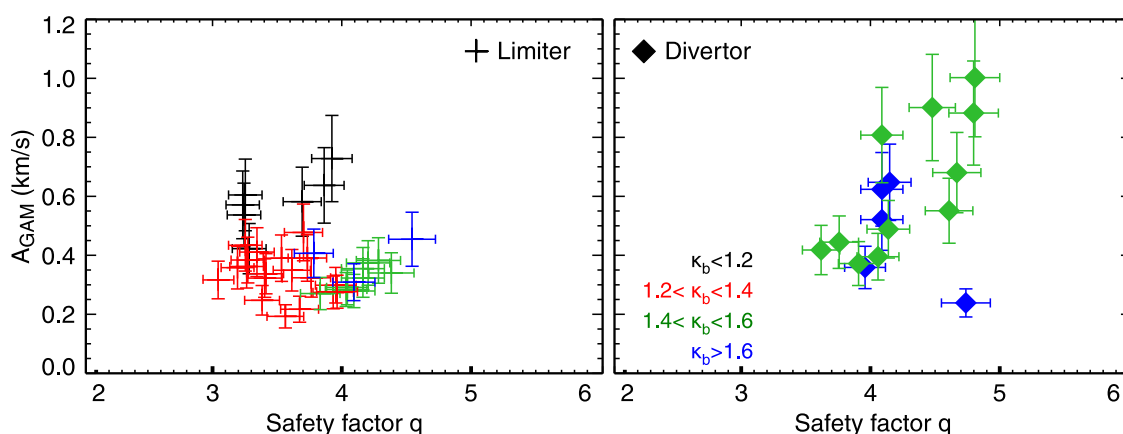


Figure 8.2: GAM amplitude against local safety factor  $q$ , colour-coded for varying boundary  $\kappa_b$ . Left: limiter GAMs. Right: divertor GAMs. The drive term  $\nabla T_e/\sqrt{\kappa_b}$  varies within 4–7.5 keV/m.

Figure 8.1 shows GAM amplitudes for the whole dataset against the plasma boundary elongation  $\kappa_b$ , colour-coded for ranges in local safety factor  $q$ . Figure 8.2 is the counterpart, showing GAM amplitude against  $q$ , with  $\kappa_b$  ranges marked by the colour. For clarity, GAMs from limiter and divertor discharges have been separated in both figures. The error in the GAM amplitude is influenced by the uncertainties of  $k_{\perp}$  and the integration over the GAM peak. It is approximated as 20%. The errors in  $\kappa_b$  and  $q$  are estimated as discussed in Sec. 7.2.1.

For limiter discharges the results in Fig. 8.1 are similar to earlier ASDEX Upgrade experiments [79] with the added benefit of a large number of points in a previously unavailable region for  $\kappa_b$ . There is a clear inverse dependence of  $A_{\text{GAM}}$  on the

elongation  $\kappa_b$ , and only a weak direct dependence on local  $q$  evident. For  $\kappa_b > 1.4$  the amplitude tends to become insensitive to elongation. There is also a trend for higher  $\kappa_b$  to be accompanied by higher  $q$  due to the experimental constraints.

For the case of divertor plasmas the effect of the X-point and strong shaping is more evident with discharges generally having higher  $q$ . The lowest GAM amplitudes in divertor plasmas are either found at low  $q$ , or at very high  $\kappa_b$ . Very high  $q$  raises  $A_{\text{GAM}}$ , while for moderate  $q$  (3.5–4.5), the impact of  $\kappa_b$  is seen again. For low to moderate  $q$  (3–4),  $A_{\text{GAM}}$  approaches the limiter values. At intermediate elongation of  $\kappa_b$ , the highest GAM amplitudes are observed. These particular points however, as will be shown in Sec. 8.3, correspond to GAMs in discharge conditions with low collisionless and collisional damping.

The dependence of  $A_{\text{GAM}}$  on  $q$  is more clearly seen in Fig. 8.2. Low-amplitude GAMs can appear regardless of the local  $q$ ,  $\kappa_b$  or plasma configuration. Although, as shown in Fig. 8.1, there is a tendency to higher  $A_{\text{GAM}}$  at lower  $\kappa_b$  for a fixed  $q$ . There is also a trend of high  $A_{\text{GAM}}$  at higher  $q$  in divertor configuration. As a general observation the influence of  $\kappa_b$  shows a clear trend for limiter data, while the influence of  $q$  might be more important for divertor plasmas.

While the safety factor  $q$  and plasma elongation  $\kappa_b$  are expected to impact the damping rate, the GAM drive, which is discussed in the following section, is also expected to influence the GAM amplitude. Figures 8.1 and 8.2 show data from the entire experimental database, which contains a non-negligible variation in the GAM drive. The GAM drive, which is discussed in more detail in Sec. 8.2, is approximated by the term  $\nabla T_e / \sqrt{\kappa_b}$ , following the example of previous ASDEX Upgrade research: the temperature gradient length is roughly proportional to the density gradient length in the edge plasma, which in turn determines the density fluctuation level for gradient-driven turbulence [79]. Figure 8.3 shows a subset of the data, in which  $\nabla T_e / \sqrt{\kappa_b}$  was limited to the intermediate range of 5–6 keV/m. The radial GAM positions in this subset are in the range  $0.94 < \rho_{\text{pol}} < 0.98$ .

For fixed GAM drive, most of the previous observations hold. As seen in Fig. 8.3 (a.1), the GAM amplitude for limiter GAMs still decreases when the elongation increases in the range  $\kappa_b < 1.4$ , before stabilising. Conversely, Fig. 8.3 (b.1) shows no clear relation between GAM amplitude and  $q$  for limiter GAMs, although for each subset of  $\kappa_b$  an increasing trend with  $q$  may possibly be observed. For divertor GAMs with fixed GAM drive, Fig. 8.3 (b.2), there is a clearer tendency towards higher amplitude at higher  $q$ . Figure 8.3 (a.2) shows that the amplitude and elongation

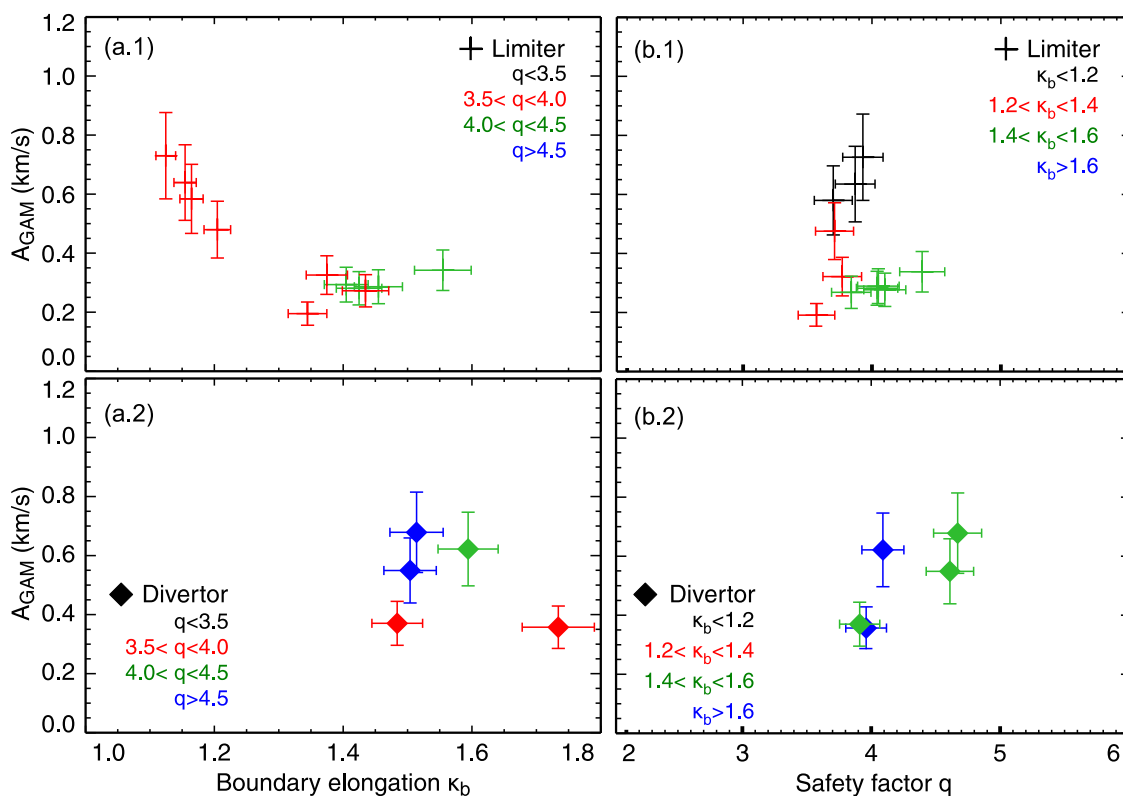


Figure 8.3: Subset of the database with fixed GAM drive, approximated by the normalised temperature gradient:  $5 \text{ keV/m} < \nabla T_e / \sqrt{\kappa_b} < 6 \text{ keV/m}$ . (a) GAM amplitude against  $\kappa_b$ , colour marks variation in  $q$ . (b) GAM amplitude against  $q$ , colour marks variation in  $\kappa_b$ .

have no clear relation for divertor GAMs, however all divertor GAMs fall into the  $\kappa_b$  range in which the amplitude curve has already flattened for limiter GAMs.

## 8.2 GAM drive

The GAM amplitude is determined by several factors: the GAM drive, the GAM damping, and energy transport processes between different components of the turbulent system. An overview of these components was given in Sec. 3.1.4. The energy transfer rate between the background turbulence and the GAM is difficult to estimate and is not addressed further in this work.

The GAM drive, i.e. the energy input into the GAM, is also a quantity that cannot easily be measured. As discussed above, the local temperature gradient  $\nabla T_e$ , normalised by  $\sqrt{\kappa_b}$ , was previously used as a proxy for the turbulence drive in

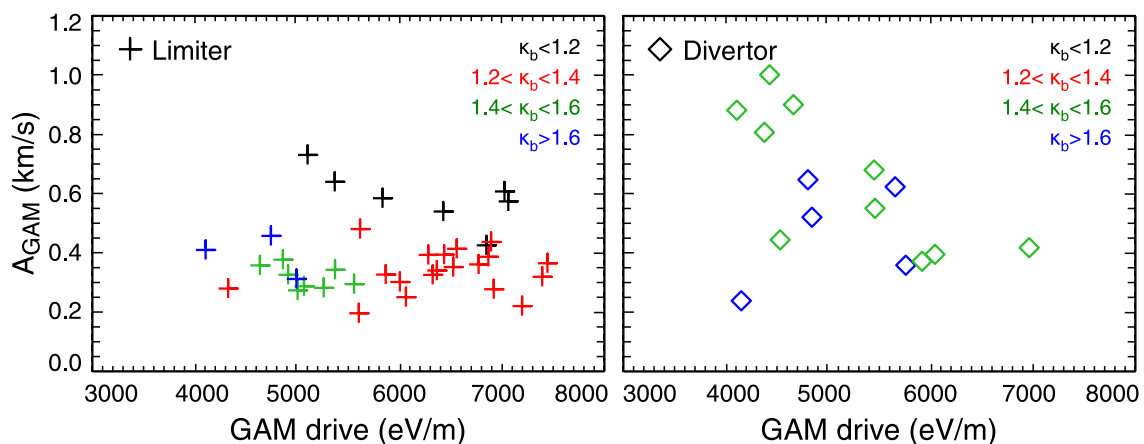


Figure 8.4: GAM amplitude against the normalised electron temperature gradient  $\nabla T_e / \sqrt{\kappa_b}$ , which is used as a proxy for the GAM drive. Left: limiter GAMs. Right: divertor GAMs. The colour marks the plasma elongation  $\kappa_b$ . The local safety factor varies in the range  $3 < q < 5$ .

#### ASDEX Upgrade.

In this new dataset, the factor  $\nabla T_e / \sqrt{\kappa_b}$  falls into the range of 5–7 keV/m for most of the data points, as can be seen in Fig. 8.4. This figure contains GAMs from the complete dataset, i.e. the data is neither limited to a particular elongation, nor to a particular local safety factor, both of which are expected to influence the GAM amplitude through the damping rate. For limiter discharges, GAMs with low and high amplitudes are found regardless of drive. The GAM amplitude in divertor discharges has a large spread at low drive, while at higher drive the maximum GAM amplitude decreases.

Finding the strongest divertor GAMs at low GAM drive might seem counterintuitive, however the damping rate must also be accounted for. As mentioned previously and as shown in the next section, both collisional and collisionless damping rates are very low for these GAMs, resulting in a strong GAM even at comparatively weaker drive.

In order to isolate the influence of the drive itself on the GAM amplitude, several subsets were selected from the complete dataset. Figure 8.5 shows  $A_{\text{GAM}}$  as a function of  $\nabla T_e / \sqrt{\kappa_b}$  for the subset of GAMs with local safety factor  $3.5 < q < 4.5$ . The data was further split into four groups, depending on the boundary elongation  $\kappa_b$ . In general, when safety factor and elongation are kept constant, there is no clear influence of the GAM drive on the amplitude. At the lowest elongation in Fig. 8.5

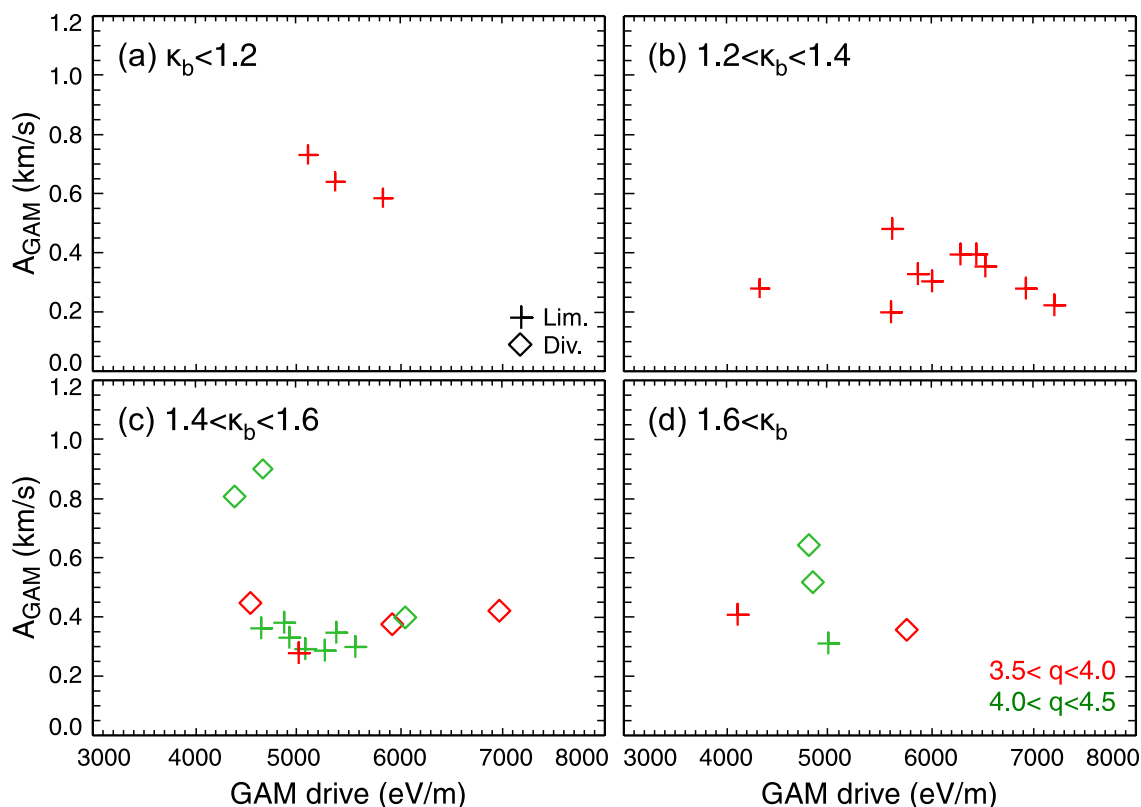


Figure 8.5: GAM amplitude against  $\nabla T_e / \sqrt{\kappa_b}$  for fixed safety factor  $3.5 < q < 4.5$  and boundary elongation. (a)  $\kappa_b < 1.2$ . (b)  $1.2 < \kappa_b < 1.4$ . (c)  $1.4 < \kappa_b < 1.6$ . (d)  $1.6 < \kappa_b$ .

(a), a slight downward trend of  $A_{\text{GAM}}$  can be observed, however it is well within the error bars (cf. Fig. 8.1). For higher  $\kappa_b$ , such as in Fig. 8.5(b) and (c), the curve is mostly flat, with the exception of the high-amplitude divertor points which were addressed above.

The overall influence of the GAM drive on the GAM amplitude level in this set of measurements, at least when used in this simple approximation, appears to be weak in comparison to the GAM damping, which is impacted by both plasma elongation  $\kappa_b$  and safety factor  $q$ .

### 8.3 GAM damping

This section focuses on the influence of the damping rate on the GAM amplitude. There are two damping processes that need to be considered: the collisionless Landau damping and the collisional damping. The collisionless damping rate of GAMs

has been calculated for numerous theoretical models, and is often used in the validation of numerical codes. Therefore, a comparison of multiple collisionless damping rates is presented here. Collisional damping of GAMs has been less studied, but is shown to play a significant role for GAMs in ASDEX Upgrade.

### 8.3.1 Collisionless damping for negligible $k_r$

In previous works that considered the impact of damping on the GAM amplitude, there has been a focus on collisionless Landau damping, which is often approximated as  $\gamma \propto \omega_{\text{GAM}} \exp(-q^2)$  [73, 79, 143]. Gao has more recently derived a more extensive formula from a gyrokinetic approach in the limit of negligible GAM radial wavenumber  $k_r \rightarrow 0$  [144]:

$$\gamma_{\text{c.less}} = -\frac{\pi^{1/2}}{2} \frac{v_{T_i}}{R} \frac{(R\omega_{\text{GAM}}/v_{T_i})^6}{7/4 + \tau} q^5 \exp \left[ -\left( \frac{qR\omega_{\text{GAM}}}{v_{T_i}} \right)^2 \right] \quad (8.1)$$

This formula gives a monotonically decreasing  $\gamma$  in the experimental range  $3 < q < 5$ , which appears to be consistent with the results of Fig. 8.2 showing the GAM amplitude increasing with  $q$ .

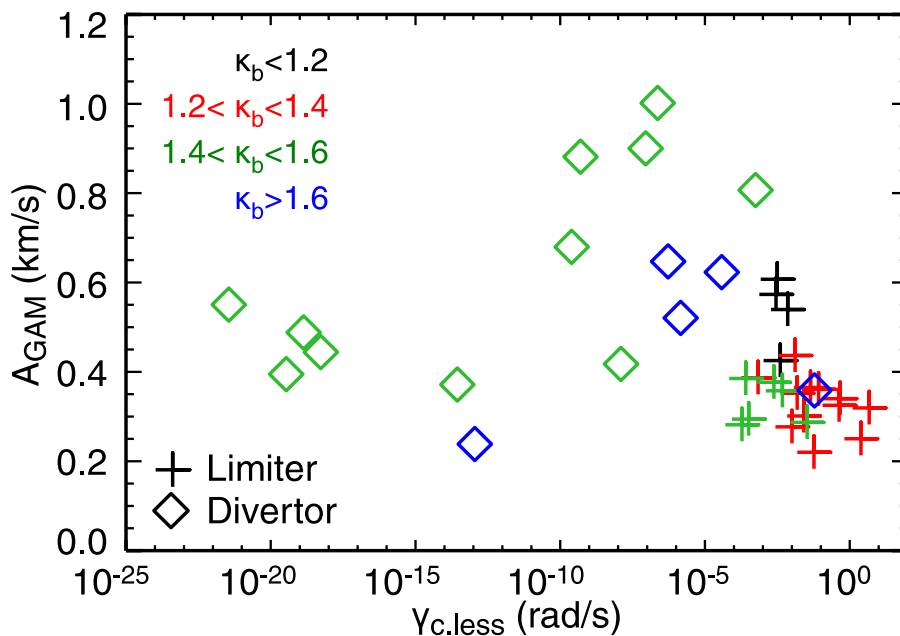


Figure 8.6: GAM amplitude against collisionless damping rate  $\gamma_{\text{c.less}}$  in the limit  $k_r \rightarrow 0$  (Eq. 8.1).

Figure 8.6 shows the measured GAM amplitude  $A_{\text{GAM}}$  as a function of the collisionless damping rate  $\gamma_{\text{c.less}}$ , according to Eq. 8.1. There is a very large variation in  $\gamma_{\text{c.less}}$ , over 25 orders of magnitude. Due to the large scatter of  $A_{\text{GAM}}$ , there is no clear dependence between damping rate and GAM amplitude, contrary to what would be expected if collisionless damping was the dominant process. While the lowest  $A_{\text{GAM}}$  are found at high  $\gamma$ , there is no straightforward trend for the limiter data, and the divertor  $A_{\text{GAM}}$  even tend to be larger at higher collisionless damping rates. If values below  $10^{-10}$  Hz are ignored there is perhaps a trend of decreasing  $A_{\text{GAM}}$  with rising  $\gamma_{\text{c.less}}$ . Nevertheless, the plasma elongation appears to have an influence on the collisionless damping rate, as most GAMs with  $\kappa_b > 1.4$  have significantly lower  $\gamma$ . This is due to the factor  $\omega_{\text{GAM}}R/v_{T_i}$  in the exponential, which will decrease for elongated plasmas (cf. Fig. 7.5). Further, the damping rates for divertor plasmas are much lower than those for limiter plasmas, with the exception of only a few points, which is due to the strong influence of  $q$ , which is generally higher in the edge region of divertor plasmas.

It must be noted that even the largest collisionless damping rates that are calculated using this model are orders of magnitude below the GAM frequency, which would let the GAM oscillate virtually unperturbed for many periods before any significant damping effect could take place. As shown in the following section, the real collisionless damping rates at ASDEX Upgrade are likely to be much larger.

### 8.3.2 Collisionless damping with finite orbit width effects

Recent theoretical work (see Ref. [145] and references therein) and simulations [135] suggest that finite orbit width effects may play a significant role for the collisionless damping rate in the case of  $q > 2$ . Sugama and Watanabe used a gyrokinetic approach to derive an expression that includes the finite orbit width effects [72, 134]:

$$\begin{aligned} \gamma_{\text{sw}} = & -\frac{\pi^{1/2}}{2} \frac{v_{T_i} q}{R_0} \left[ 1 + \frac{2(23/4 + 4\tau + \tau^2)}{q^2(7/2 + 2\tau)^2} \right]^{-1} \\ & \times \left[ \exp(-\hat{\omega}_{\text{G}}^2) \{ \hat{\omega}_{\text{G}}^4 + (1 + 2\tau)\hat{\omega}_{\text{G}}^2 \} + \frac{1}{4} \left( \frac{k_r v_{T_i} q}{\Omega_i} \right)^2 \right. \\ & \left. \times \exp(-\hat{\omega}_{\text{G}}^2/4) \left\{ \frac{\hat{\omega}_{\text{G}}^6}{128} + \frac{1 + \tau}{16} \hat{\omega}_{\text{G}}^4 + \left( \frac{3}{8} + \frac{7}{16}\tau + \frac{5}{32}\tau^2 \right) \hat{\omega}_{\text{G}}^2 \right\} \right] \quad (8.2) \end{aligned}$$

Here,  $\hat{\omega}_{\text{G}} = R_0 q \omega_{\text{GAM}} / v_{T_i}$  and  $\Omega_i = eB/m_i$ . The impact of the finite orbit width

effect is very sensitive to the radial wavenumber  $k_r$  of the GAM. In AUG the radial wavelength  $\lambda_r$  of the GAM is obtained from radial cross-correlation measurements [146] to be of the order of 4–5 cm, i.e. typically twice the zonal width of the GAMs. This estimate is consistent with previous measurements of the width and spacing of GAM frequency plateaus [65], as well as the results presented in Sec. 9.2.4. A  $\lambda_r$  of this magnitude gives a corresponding  $k_r$  of approximately  $150 \text{ m}^{-1}$ , which should be considered as an upper boundary.  $k_r$  of this magnitude have also been measured in DIII-D [61].

Qiu *et al.* [70] note that Eq. 8.2 is only valid for  $k_r v_{T_i} q^2 / \Omega_i \ll 1$ , which is not the case for the data that is presented here. In the limit of large orbit drift width (ODW) the dominant resonant mechanism changes from low order harmonic transit resonance to high order harmonic resonance, and the damping rate becomes independent of  $q$ . Gao derives the following equation for the collisionless damping rate in the large ODW limit from a gyrokinetic approach, which includes various effects, such as the plasma geometry [71, 137]:

$$\begin{aligned} \gamma_{\text{LODW}} = & -\frac{4\kappa^2 \sqrt{7/4 + \tau} v_{T_i}}{\hat{k}^2 (\kappa^2 + 1)^{3/2} R_0} \left( 1 + \frac{2\kappa^2 + 5}{4\kappa^2 + 4} s_\kappa - \frac{27\kappa^2 + 9}{8\kappa^2 + 8} \epsilon^2 - \frac{7\kappa^2 + 4}{4\kappa^2 + 4} \Delta'^2 \right. \\ & \left. + \frac{9\kappa^2}{4\kappa^2 + 4} \epsilon \Delta' \right) \times \exp \left[ -\frac{\sqrt{7/4 + \tau}}{\hat{k}} \sqrt{\frac{2\kappa^2}{\kappa^2 + 1}} \left( 1 + \frac{3\kappa^2 + 4}{4\kappa^2 + 4} s_\kappa \right. \right. \\ & \left. \left. - \frac{9\kappa^2 + 3}{8\kappa^2 + 8} \epsilon^2 - \frac{3\kappa^2 + 2}{4\kappa^2 + 4} \Delta'^2 + \frac{4\kappa^2 + 1}{4\kappa^2 + 4} \epsilon \Delta' \right) \right] \end{aligned} \quad (8.3)$$

Here,  $\hat{k} = k_r v_{T_i} / \Omega_i$  is the normalised radial wavenumber.

### 8.3.3 Comparison of the collisionless damping rates

Figure 8.7 shows a comparison of the three collisionless damping models for the whole database, plotted against the normalised poloidal flux radius  $\rho_{\text{pol}}$ , with  $\gamma_{\text{c.less}}$  in red from Eq. 8.1,  $\gamma_{\text{SW}}$  in green from Eq. 8.2 and  $\gamma_{\text{LODW}}$  in blue from Eq. 8.3. For the calculation of  $\gamma_{\text{SW}}$  and  $\gamma_{\text{LODW}}$ , a constant estimate of  $k_r = 150 \text{ m}^{-1}$  is used. While for selected cases,  $k_r$  has been measured between 75 and  $150 \text{ m}^{-1}$ , accurate measurements for each GAM in the database do not exist, and the calculated damping rates should be taken as an upper boundary. Including the low  $k_r$  effects raises  $\gamma_{\text{c.less}}$  by 4 to 12 orders of magnitude, depending on radius and  $q$ . In the large ODW limit, the damping rate  $\gamma_{\text{LODW}}$  lies approximately 2 to 3 orders of magnitude below

$\gamma_{\text{sw}}$ , but still significantly above the  $\gamma_{\text{c.less}} (k_r \rightarrow 0)$  value. For these models, the damping rate is closer to the measured GAM frequency, in particular towards the plasma core.

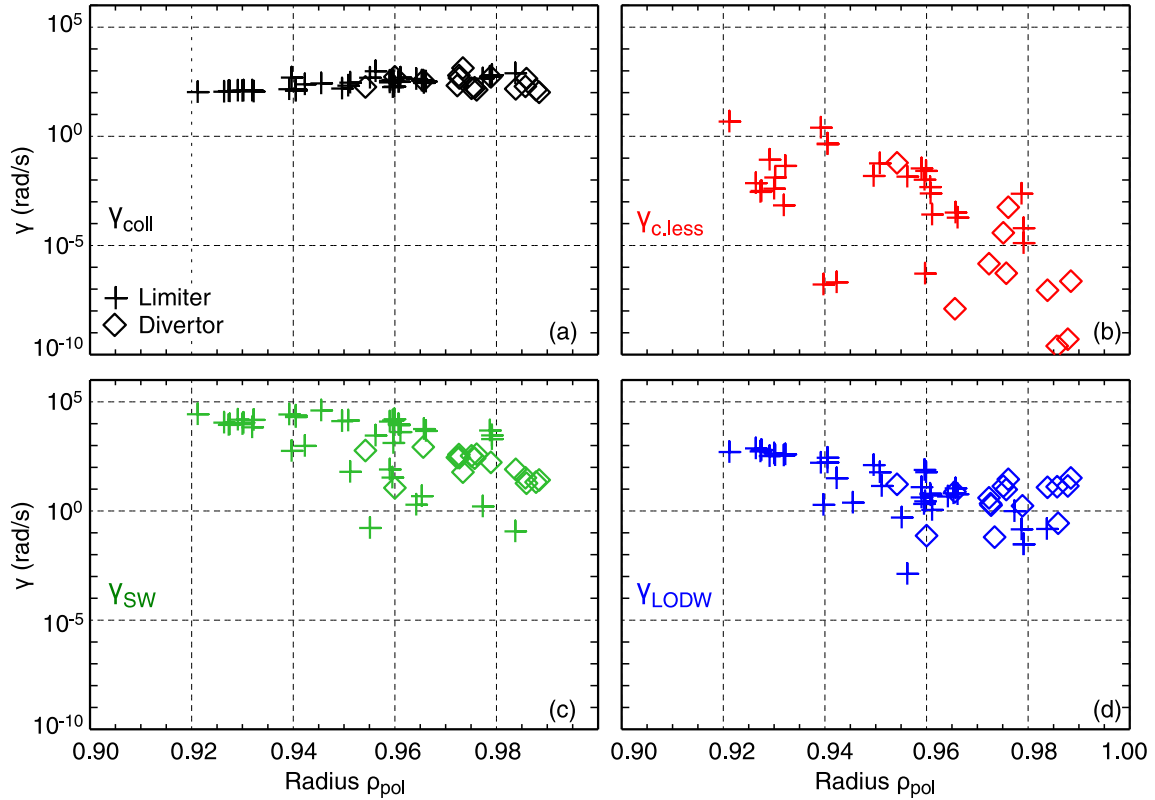


Figure 8.7: Comparison of damping rates against normalised poloidal flux radius  $\rho_{\text{pol}}$ . (a) Collisional damping rate (black). (b) Collisionless damping for  $k_r \rightarrow 0$  (red). (c) Collisionless damping with finite ODW corrections (green). (d) Collisionless damping in the large ODW limit (blue). A constant value of  $k_r = 150 \text{ m}^{-1}$  is used.

### 8.3.4 Collisional damping

The effect of collisional damping should also be taken into account. As recently noted by Gao [145], collisional damping has often been ignored as it was not thought to play a large role in the plasma core. But, as GAMs are observed in the plasma edge region, the collisional damping may in fact play the dominant role. A first estimation of the collisional damping rate for GAMs was given by Novakovskii *et al.* as  $\gamma = -4/7\nu_i$  (the original publication mistakenly included a  $q$  in the denominator) [34, 147]. The

ion collisionality in a deuterium plasma is defined as

$$\nu_i = 4.80 \times 10^{-2} \sqrt{1/2} \frac{n_e}{T_i^{3/2}} \ln \Lambda. \quad (8.4)$$

Here,  $\nu_i$  is in Hz,  $n_e$  is in  $\text{m}^{-3}$ ,  $T_i$  in eV and the Coulomb logarithm is  $\ln \Lambda \approx 17$ . Using a gyrokinetic model, Gao derived the following equation for the collisional damping rate [145]:

$$\left(\frac{7}{4} + \tau\right) \frac{qR}{v_{T_i}} \gamma + \frac{3qR}{8v_{T_i}} \nu_i + \frac{qR^3}{v_{T_i}^3} \gamma (4\gamma^2 + 4\gamma\nu_i + \nu_i^2) = 0 \quad (8.5)$$

In the case of  $\nu_i qR/v_{T_i} \ll 1$  and  $\gamma qR/v_{T_i} \ll 1$ , the formula simplifies to

$$\gamma_{\text{coll}} = -\frac{3}{14 + 8\tau} \nu_i. \quad (8.6)$$

Numerical calculations confirm that all the AUG experimental GAM measurements satisfy this condition. Note, unlike Eq. 8.1, there is no implicit  $\kappa$ -dependence here.

Figure 8.7(a) shows the collisional damping  $\gamma_{\text{coll}}$  from Eq. 8.6 in black. A comparison of the various damping rates indicates that, if ODW effects are neglected, the collisional damping rate is orders of magnitude above the collisionless damping rate  $\gamma_{\text{c.less}}$ . This observation was similarly noted recently in Tore Supra [69]. However, when the contribution of  $k_r$  is taken into account, the collisionless damping rate can become dominant in limiter low  $q$  conditions, while at high  $q$  limiter and divertor edge conditions the collisional term may still dominate or be comparable to the collisionless damping rate.

Experimentally, the variation of  $A_{\text{GAM}}$  with collisional damping is different between limiter and divertor configurations. Figure 8.8 shows the GAM amplitude as a function of  $\gamma_{\text{coll}}$  from Eq. 8.6 for divertor and limiter plasmas. In the divertor case there is a much clearer trend of decreasing  $A_{\text{GAM}}$  with rising  $\gamma_{\text{coll}}$ . In the limiter case, there is more spread in the data, and for each subset of measurements at similar  $\kappa_b$  there is almost no variation with  $\gamma_{\text{coll}}$ . The collisional damping appears to have the effect of setting an upper boundary on the GAM amplitude, particularly for divertor plasmas. In the case of limiter plasmas the GAM amplitude seems to be determined by the boundary elongation, as seen in Fig. 8.1.

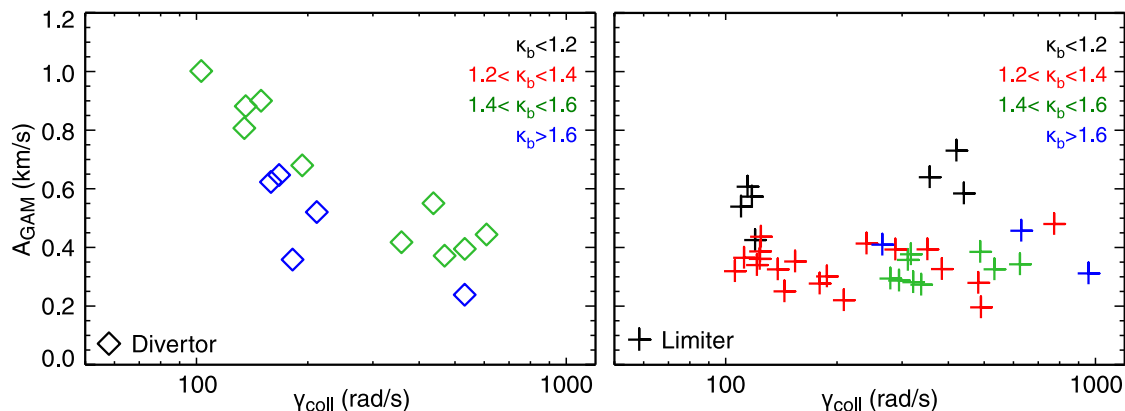


Figure 8.8: Scaling of GAM amplitude against collisional damping rate  $\gamma_{\text{coll}}$ . Left: Divertor plasmas. Right: Limiter plasmas.

## 8.4 Discussion

This chapter investigates the behaviour of the GAM amplitude in relation to changes in plasma geometry, drive and damping. The GAM amplitude is seen to decrease in limiter plasmas with increasing elongation. Low- $q$  GAMs from divertor plasmas exhibit similar amplitudes, whereas the GAM amplitude is found to increase significantly at higher safety factor. The GAM amplitude scaling has been less often studied than the GAM frequency scaling in recent research, with little detailed investigation of the effects of plasma configuration and geometry [52]. Prior results from DIII-D suggest that a large safety factor  $q$  might lead to higher GAM amplitudes due to reduced collisionless damping [66], while first ASDEX Upgrade results exhibit different observations for limiter and divertor plasmas [79]. In the present dataset, in limiter cases the boundary elongation has a clear effect on the GAM amplitude, but not in the divertor case. Here, the role of the X-point in the divertor configuration requires further investigation.

The roles of collisionless Landau damping and collisional damping were investigated in detail. In the absence of  $k_r$  effects, collisional damping clearly dominates over collisionless damping towards the outer plasma edge region. More towards the core region, however, the rising trend of the collisionless damping may cause  $\gamma_{\text{c,less}}$  to become dominant. Tore Supra results similarly predict a stronger influence of collisional damping in the relevant plasma edge region [69]. With inclusion of finite orbit drift width effects, the collisionless damping is increased overall (green and blue points in Fig. 8.7). The green points can be considered an upper boundary

to the collisionless damping rates, based of the current measured  $k_r$  estimates. A lower  $k_r$  would reduce  $\gamma_{\text{SW}}$  towards the original  $\gamma_{\text{c.less}}$  (red points). The large ODW limit values  $\gamma_{\text{LODW}}$  are likewise reduced with decreasing  $k_r$ . Within this picture, the collisional damping would play a larger role for the divertor high  $q$  cases in the plasma edge, while collisional and collisionless damping may play equal roles for limiter low  $q$  cases towards the plasma core. This switch in damping dependency may go towards explaining the different behaviours observed in Fig. 8.8 for the limiter and divertor configurations.

In addition to the GAM damping, the role of turbulence drive must be considered. For the present dataset, the quantity  $\nabla T_e / \sqrt{\kappa_b}$  was used as a proxy for the turbulence drive. While there was some variation in this drive term, no clear influence of the drive on the GAM amplitude could be determined when safety factor  $q$  and elongation  $\kappa_b$  were kept constant. While the largest GAM amplitudes were found at the lowest GAM drive, the same measurements were shown to have very low collisional and collisionless damping, and thus offer no contradiction to the conclusion that the GAM damping rate is the most significant contributor to the amplitude of GAMs in ASDEX Upgrade. In general, it is questionable whether the influences of damping and drive on the GAM amplitude can truly be separated, especially experimentally. In such a self-regulating system, the turbulence level, GAM amplitude, energy transfer processes and gradients are all interlinked, and measurements only record the resulting balance. A full model incorporating all of these factors would be needed to make more reliable predictions.

In summary, this chapter presents results from an extensive database of GAM amplitude measurements and damping rate predictions from a variety of models, which was established from a set of shape-scan experiments at ASDEX Upgrade. Different scaling behaviour is observed for GAMs in divertor discharges, found in the high- $q$  edge region, and for GAMs in limiter discharges, typically observed further towards the core. It is established that for ASDEX Upgrade parameters, predictions of the collisionless damping rate need to account for finite orbit width effects, and that collisional damping must not be neglected. For GAMs in the edge of divertor discharges, the collisional damping rate is found to be dominant, in agreement with an observed decrease of the GAM amplitude for higher collisional damping.

# Chapter 9

## GAM structure and propagation

The two previous chapters covered the scaling behaviour of the GAM frequency, amplitude and the GAM damping rate and dependencies on the plasma geometry. In this chapter, the focus is placed on the radial structure of the GAM in ASDEX Upgrade, as well as the radial propagation and the magnetic signature. Section 9.1 introduces the experiments and the spatial correlation setup of the Doppler reflectometers that was used in order to investigate the radial propagation. Section 9.2 presents results on the radial structure of the GAM for different plasma configurations. Section 9.3 investigates the radial GAM propagation using two spatial correlation techniques. The magnetic signature and poloidal structure of the GAM are discussed in Sec. 9.4. The chapter concludes with a discussion of the results in Sec. 9.5.

### 9.1 Description of experiments

This section will give a short overview of the experimental setup that was used for the GAM structure studies. A detailed description of the experimental conditions, the number of sweeps, as well as typical plasma density and temperature profiles can be found in Sec. 7.1, since the same discharges that were used for the scaling studies of GAM frequency and amplitude were also used for the structure investigations. However, for radial correlation studies, which are necessary to investigate the propagation of the mode, it is essential to have simultaneous measurements in at least two different radial positions.

For that purpose, the setup of the ASDEX Upgrade Doppler reflectometers was

modified from its usual configuration, as shown in Fig. 5.6. Instead of having one system operate in O-mode from above the midplane and one system in X-mode from below the midplane, both V-band reflectometers were coupled to the lower X-mode antenna pair, which has a fixed probing angle of  $42.5^\circ$  upwards. While the scaling experiments in chapters 7 and 8 only used one channel that was stepping its probing frequencies, and hence its radial measurement position, within that range, the correlation setup allows simultaneous measurements at both depicted positions. A more detailed description of the experimental setup for correlation Doppler reflectometry can be found in Ref. [125].

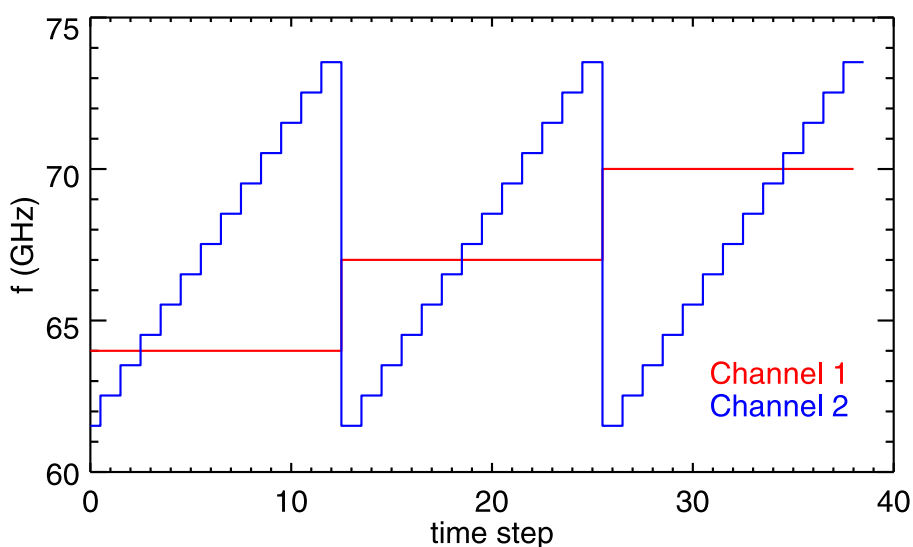


Figure 9.1: Probing frequencies for fixed channel 1 (red) and sweeping channel 2 (blue) during discharge #29722.

In order to investigate the radial GAM propagation, the cross-correlation between simultaneous signals from at least two different radial positions needs to be calculated. To determine the range over which any correlation for the GAM can be found, one channel should remain at a fixed position, ideally at the radial location where the GAM is strongest, while the second channel covers the entire range which is accessible for a V-band reflectometer in X-mode. However, the probing frequency which will reach the location of the strongest GAM is difficult to estimate in advance, as small variations in plasma density can have a large effect. Therefore, the frequency of the fixed channel was also periodically changed in order to ensure that it would at least partially detect a strong GAM. The frequency pattern for channel 1 (fixed) and channel 2 (sweeping) is shown in Fig. 9.1. After each complete radial

sweep of channel 2, the first channel is changed from one of three frequencies to the next, and remains fixed during the next sweep of channel 2. These fixed frequencies were 64, 67 and 70 GHz. Channel 2 was swept from 61.5 to 73.5 GHz. The sweep was started at 61.5 GHz because any lower frequencies in the V-band range would only probe the far scrape-off layer for the chosen experimental conditions, where no valuable GAM data would be expected. The frequencies of channel 2 were set off by 0.5 GHz from the channel 1 frequencies in order to limit possible interference between the channels.

## 9.2 GAM structure

The radial structure of the geodesic acoustic mode has been observed in past experiments at ASDEX Upgrade and many other devices. A list of references can be found in Sec. 3.4.3. Of interest in studies of the structure are the width of the region in which GAMs are found and the variation of GAM frequency and amplitude within that region. In general, there is no single typical radial GAM structure, but instead one of multiple cases may occur:

- Single eigenmode GAM: only one GAM at a fixed frequency is observed, either in a narrow radial range or stretched over a wider radial range.
- Multiple eigenmode GAMs: there are two (or more) neighbouring regions in which the GAMs have different fixed frequencies, possibly with a small overlap region in which two GAMs may be measured simultaneously.
- Continuum GAM: the GAM frequency changes continuously over the entire radial range in which GAMs are detected.

In past ASDEX Upgrade experiments [65], the plasma boundary elongation  $\kappa_b$  and the safety factor  $q$  appeared to have the strongest influence on both the observable GAM region as well as the radial GAM structure: the higher the  $q$  and the lower the  $\kappa_b$ , the further in GAMs were observed. For limiter shots with low elongation, multiple neighbouring eigenmode GAMs were seen, while divertor discharges with high  $\kappa_b$  usually featured only a single eigenmode GAM.

In order to expand on these results, the shape-scan experiments described in Secs. 7.1 and 9.1 are well-suited, since they feature different plasma configurations

and a wide range of variation in the plasma shape. In fact, all three cases for radial GAM structure could be observed during these discharges.

### 9.2.1 Multiple eigenmode GAMs

Similar to the previous ASDEX Upgrade results, multiple neighbouring eigenmode GAMs, or multiple plateaus at fixed GAM frequencies, were only observed in the low-elongation phases of limiter discharges, which is also where GAMs are observed the furthest towards the plasma core. Figures 9.2 and 9.3 show the GAM structure for limiter discharge #29722, during its initial nearly circular configuration of  $\kappa_b = 1.12$ .

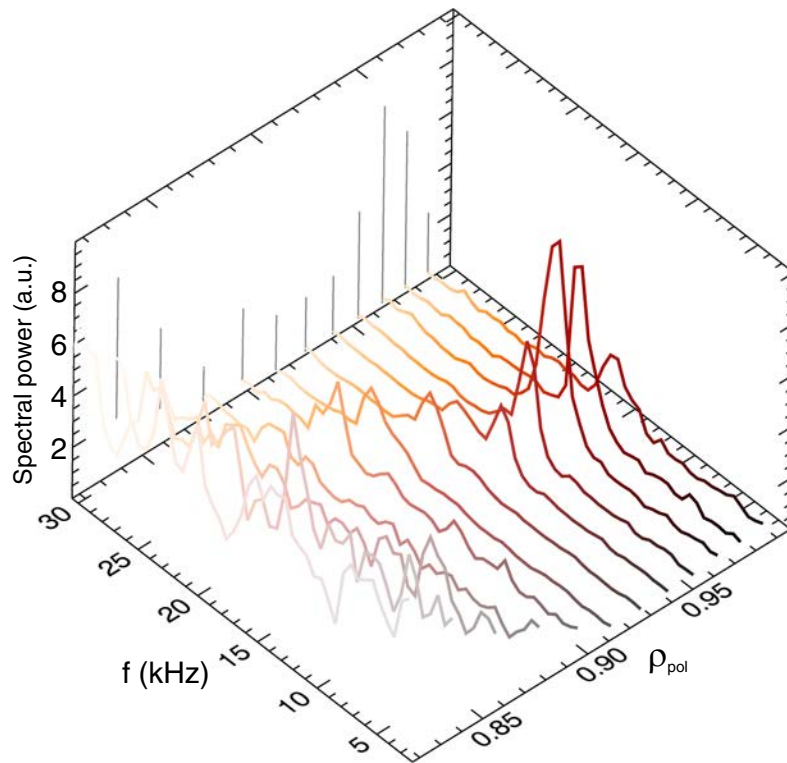


Figure 9.2: Three-dimensional view of the velocity fluctuation power spectra for limiter discharge #29722,  $t = 1.15\text{--}1.35\text{ s}$ , highlighting the radial variation of the GAM frequency and the intensity of the GAM peak.  $\kappa_b = 1.12$ ,  $q_{95} \approx 3.8$ .

Figure 9.3 (c) shows the power spectrum of the plasma velocity fluctuations as a function of the normalised poloidal flux radius  $\rho_{\text{pol}}$ , on top of which the GAM maxima are plotted where GAMs were detected. The strongest GAM peak is seen

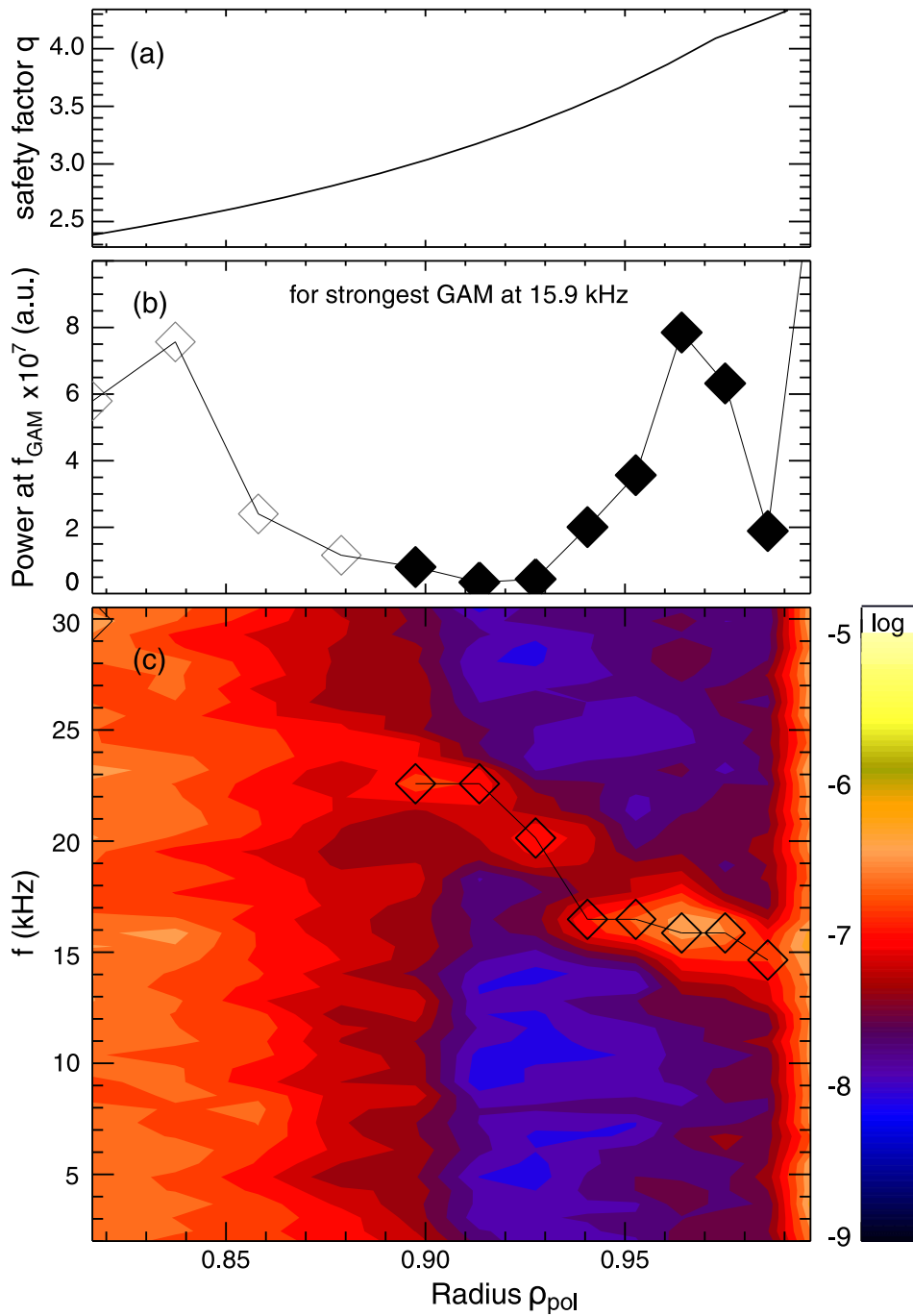


Figure 9.3: ASDEX Upgrade limiter discharge #29722 at  $t = 1.15\text{--}1.35$  s and  $\kappa_b = 1.12$ . a) Radial profile of safety factor  $q$  ( $q_{95} \approx 3.8$ ). b) Radial profile of the spectral power (linear scale) at  $15.9 \pm 0.1$  kHz, the frequency of the strongest GAM. Open symbols refer to measurement positions at which no GAM was detected. c) Contour plot of the velocity fluctuation power spectra (log scale) over the radial range covered by one reflectometer sweep between 61.5 and 73.5 GHz. Overlaid are the detected GAM maxima.

at  $f_{\text{GAM}} = 15.9 \text{ kHz}$  at  $\rho_{\text{pol}} = 0.97$ . Between  $\rho_{\text{pol}} = 0.94$  and  $0.99$ , i.e. over a range of approximately  $2.5 \text{ cm}$ , the GAM frequency appears locked. Then, towards the plasma core, at  $\rho_{\text{pol}}$  between  $0.88$  and  $0.91$ , a second GAM plateau can be seen at  $f_{\text{GAM}} = 22.5 \text{ kHz}$ . There is a short transition region between the two plateaus. Further towards the centre, as well as at the very plasma edge (close to the last closed flux surface), the overall background power increases and no GAMs are detected.

Figure 9.3 (a) and (b) show the radial  $q$ -profile and the spectral power at  $15.9 \text{ kHz}$ , respectively. The safety factor is obtained from the EQH equilibrium reconstruction code. The value of the safety factor is larger than 3 for the observable GAM region. The eigenmode GAM at  $15.9 \text{ kHz}$  is strongly peaked and quickly decreases in strength towards both sides of the plateau, leaving no trace further towards the plasma core in the second plateau region. The filled diamonds signify the measuring positions at which GAMs were detected.

The three-dimensional view of the GAM structure in Fig. 9.2, which has a linear scale for the spectral power, as opposed to the logarithmic scale of the contour plot, illustrates that the outer GAM is many times stronger than the inner GAM, most likely due to the increasing collisionless GAM damping rates in the plasma core, as discussed in the preceding chapter.

Figure 9.4 shows the original set of power spectra for each measurement at probing frequencies between  $61.5$  and  $72.5 \text{ GHz}$  that was used to create the 3D plot and the contour plot in the previous figures. For the higher probing frequencies, from  $67.5 \text{ GHz}$  onwards, the power in the broadband background rises from step to step. Due to this, the GAM peak is less pronounced until it is no longer seen for probing frequencies of  $70.5 \text{ GHz}$  and above.

Multiple eigenmode GAMs, such as in this example, were only found during limiter configuration discharges, at relatively low elongation of  $\kappa_b < 1.35$ . For higher-elongated limiter discharges, there was only a single observable eigenmode (see below). This limit suggests a possible reason why multiple eigenmode GAMs could not be observed in divertor plasmas: even at the lowest achievable elongations,  $\kappa_b$  was still above  $1.4$ , and in more typical scenarios  $\kappa_b$  will be at  $1.6$ – $1.7$ .

## 9.2.2 Continuum GAM

The case of the continuum GAM has some similarities to that of multiple eigenmode GAMs, in that a radial variation of the GAM frequency can be observed which is

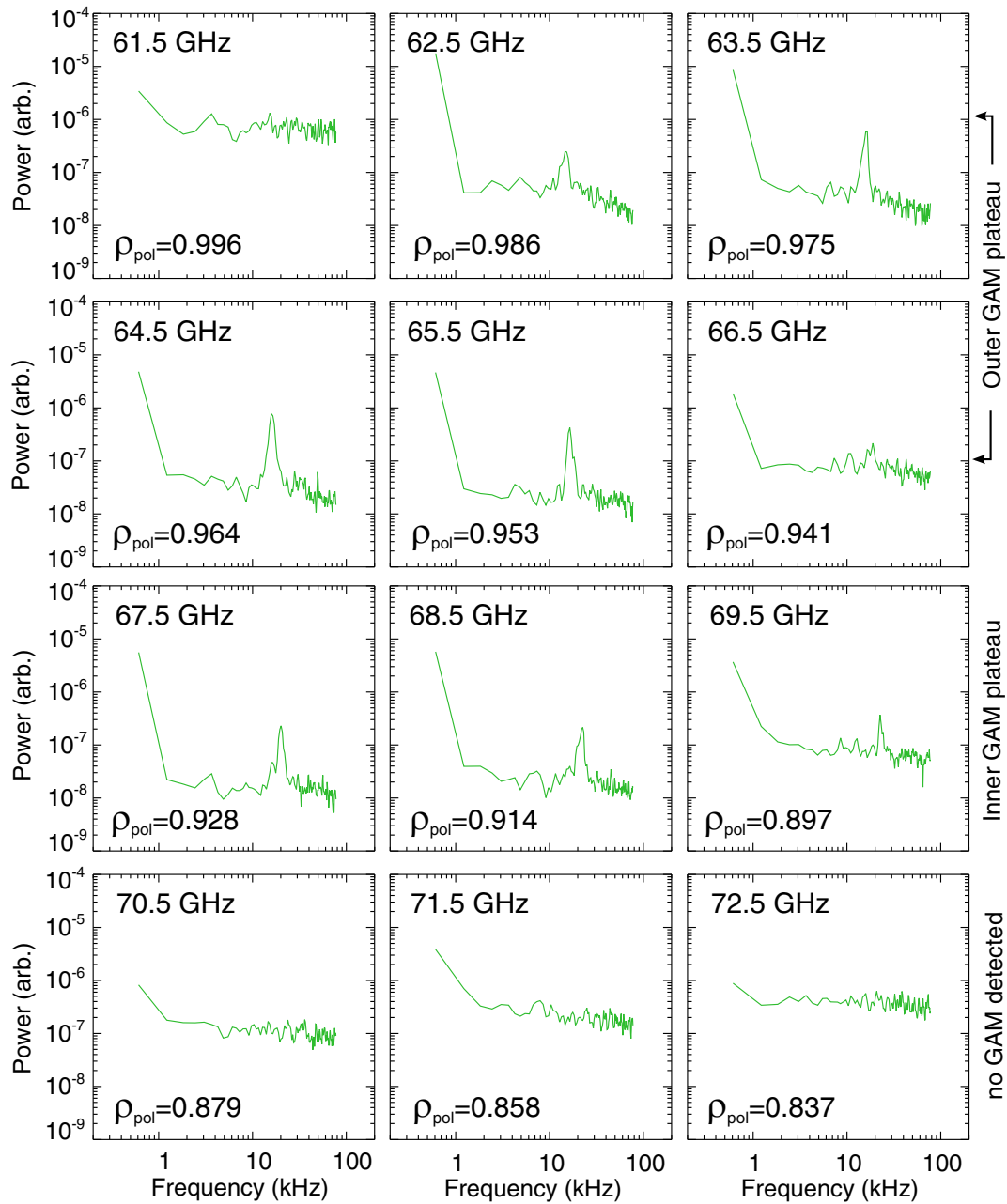


Figure 9.4: Limiter discharge #29722,  $t = 1.15\text{--}1.35\text{ s}$ ,  $\kappa_b = 1.12$ ,  $q_{95} \approx 3.8$ : Raw velocity fluctuation power spectra data for one radial reflectometer sweep from 61.5 GHz (at last closed flux surface) to 72.5 GHz (towards plasma centre,  $\rho_{\text{pol}} \approx 0.84$ ). GAM peaks are visible between 62.5 and 69.5 GHz.

somewhat in line with the predicted scaling based on local plasma temperature. However, while in the previous case it is possible to clearly separate two neighbouring regions, the continuum GAM does not lock to one frequency over a wider range, but instead changes continuously.

Figures 9.5 and 9.6 show an example of a continuum GAM structure from limiter discharge #29650 at low boundary elongation  $\kappa_b = 1.18$ , together with a radial profile of  $q$  and the GAM peak strength at the frequency of the strongest GAM, 19.5 kHz. In this case, GAMs are visible almost over the entire radial range covered by the frequency sweep, i.e.  $\rho_{\text{pol}} = 0.89\text{--}0.97$  (or 4 cm). The curve of the GAM peaks flattens somewhat in the centre, suggesting a weakly locking eigenmode GAM between  $\rho_{\text{pol}} = 0.92$  and 0.97, however the intensity of the GAM peak at 19.5 kHz is already strongly diminished towards the outer part of that region. This is unlike the results from Fig. 9.3, and points towards the presence of a continuum GAM.

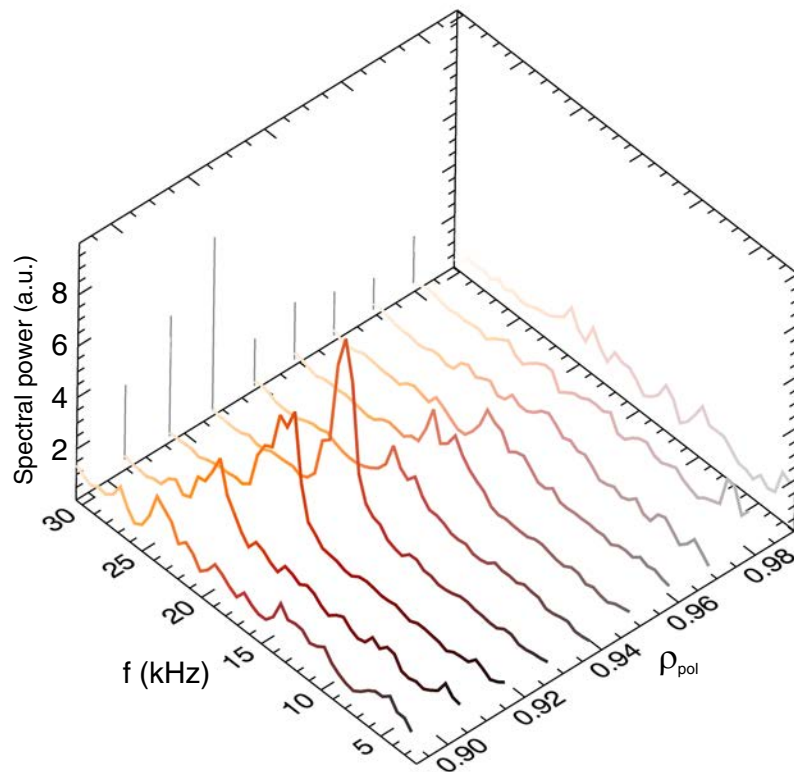


Figure 9.5: Three-dimensional view of the velocity fluctuation power spectra for limiter discharge #29650,  $t = 2.10\text{--}2.25$  s.  $\kappa_b = 1.18$ ,  $q_{95} \approx 3.8$ .

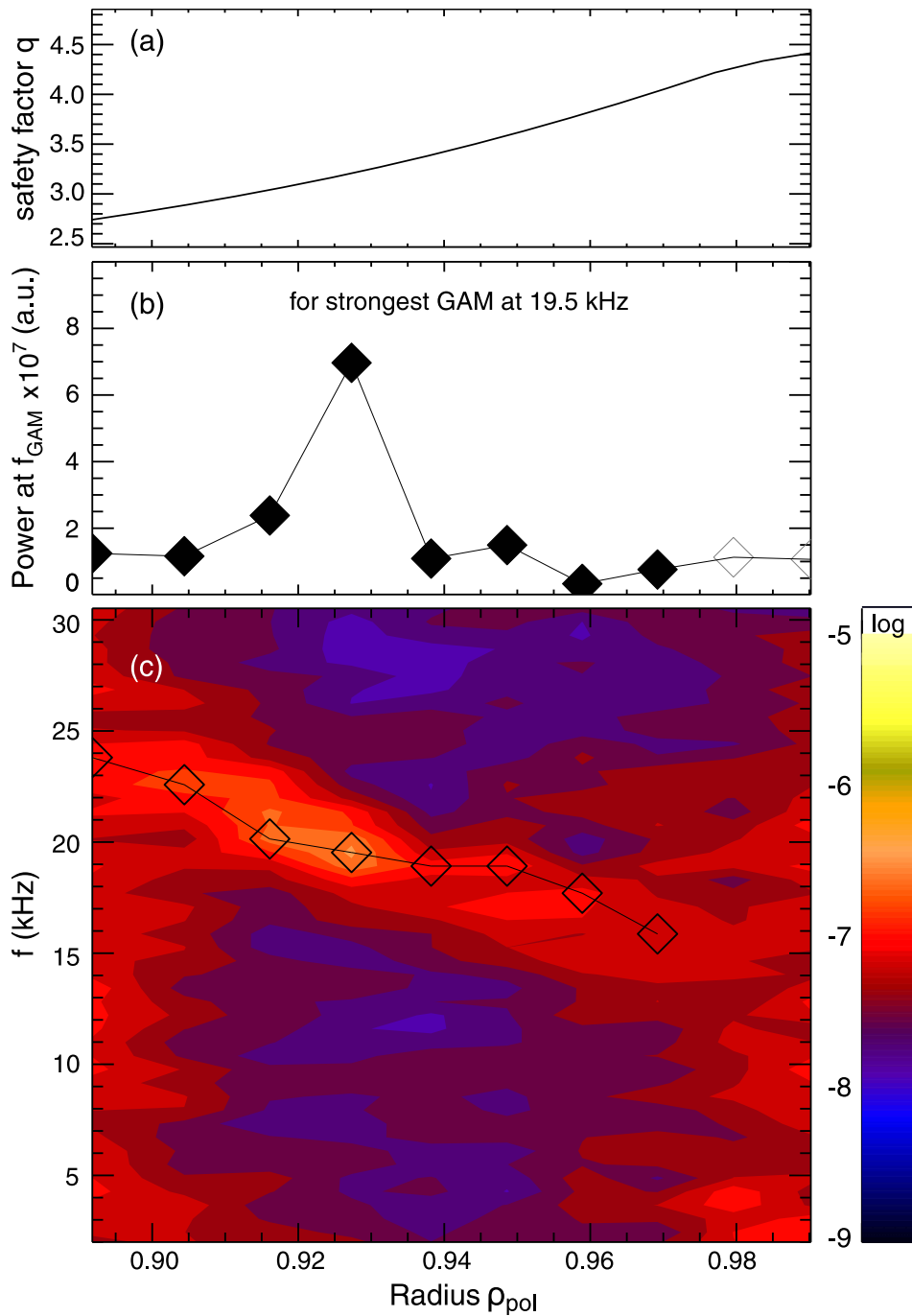


Figure 9.6: Limiter discharge #29650 at  $t = 2.10$ – $2.25$  s and  $\kappa_b = 1.18$ . a) Radial profiles of safety factor  $q$ , with  $q_{95} \approx 3.6$ . b) Radial profile of the spectral power at  $19.5 \pm 0.1$  kHz, the frequency of the strongest GAM. c) Contour plot of the velocity fluctuation power spectra over the radial range covered by one reflectometer sweep between 62.5 and 71.5 GHz. Overlaid are the detected GAM maxima.

The safety factor ranges from 2.7 to 4.0 in the range of GAM observations, which is slightly lower, but of a similar magnitude as before. However, in this discharge the strongest GAM is observed further towards the centre. In addition to the similar  $q$  profile, plasma density and elongation were almost identical in discharges #29650 (continuum) and #29722 (two GAM plateaus). In the continuum discharge there was slightly more ECRH power input, 600 kW as opposed to 400 kW, leading to higher temperatures in the edge, and therefore possible modifications in GAM drive and damping behaviour (see Ch. 8).

Similar to the previous example, the continuum GAM transitions to a single eigenmode GAM once the plasma elongation exceeds  $\kappa_b \approx 1.35$ . Before this transition, the discharge does not exhibit any signs of multiple GAM plateaus. The transition over the course of the discharge is depicted in Fig. 9.7. First, at low elongation, the GAM frequency varies between 15 and 23 kHz over a wide radial range. Then, as the elongation approaches  $\kappa_b \approx 1.3$ , the overall GAM frequency is lowered. This agrees with the expected frequency scaling behaviour, see Ch. 7. The structure itself changes, the gradient in the frequency flattens and a locked frequency GAM appears to develop near the plasma edge. Finally, as the elongation exceeds  $\kappa_b > 1.4$ , there is almost no more variation in the GAM frequency over the measurement range.

Due to an increase in the plasma density towards the end of the discharge, the cutoff positions are moving further toward the plasma edge, partially into the scrape-off layer. The overall measuring region covered by one radial sweep shrinks. Simultaneously, the strongest GAM also moves outward to the locked plateau and the width of the GAM region decreases. Measurements from discharge #29722, where the radial sweep went further into the plasma even at high  $\kappa_b$ , confirm this narrowing of the GAM region.

### 9.2.3 Single eigenmode GAM

As mentioned in the previous sections, whenever the plasma elongation exceeds a limit of approximately  $\kappa_b = 1.35$ , the radial structure of the GAM changes to a single locked frequency in a relatively narrow range.

Figure 9.8 shows the radial GAM structure of limiter discharge #29722 during its highest elongation at  $\kappa_b = 1.67$ . It can be seen that the radial range in which GAMs are observed has shrunk significantly to a width of less than 2 cm, which is consistent

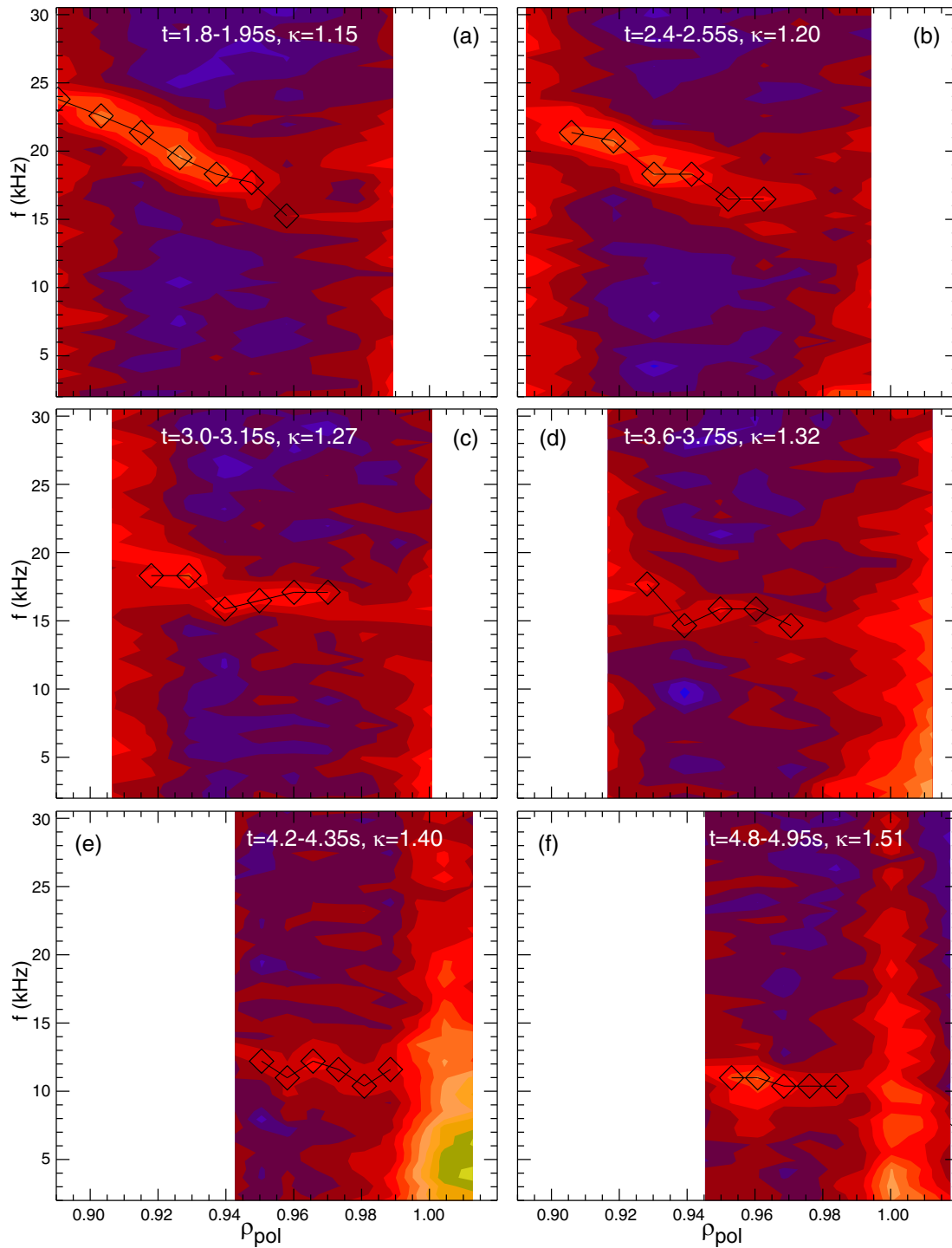


Figure 9.7: Limiter discharge #29650, transition from continuum GAM to single eigenmode GAM during variation of the plasma shape from nearly circular ( $\kappa_b = 1.15$ ) to elongated ( $\kappa_b = 1.51$ ). The radial region of measurement varies due to movement of the cutoff positions with increasing plasma density. The same colour scale was used for all plots.

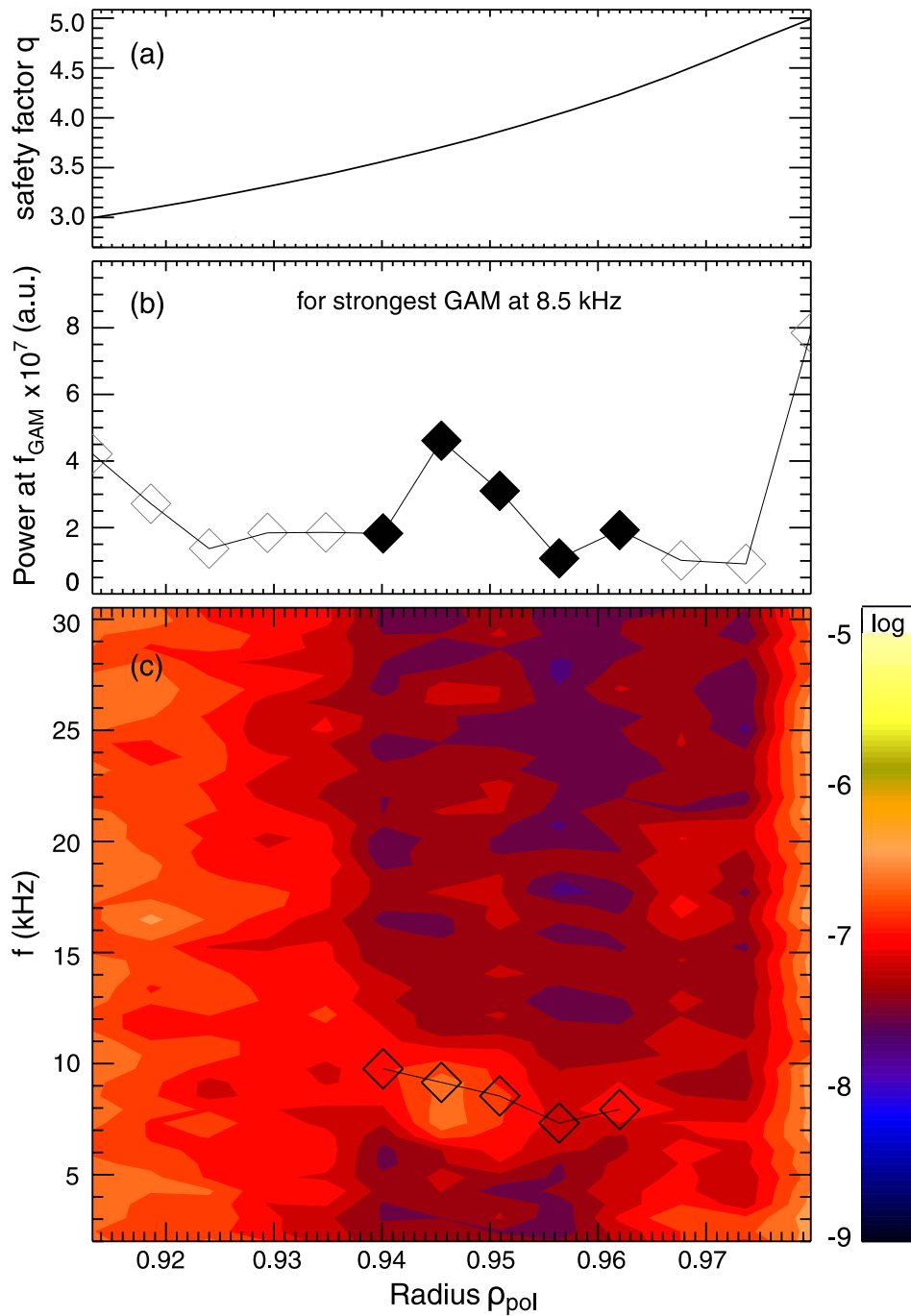


Figure 9.8: Limiter discharge #29722 at  $t = 3.50\text{--}3.70$  s and  $\kappa_b = 1.67$ . a) Radial profile of safety factor  $q$ ,  $q_{95} \approx 3.8$ . b) Radial profile of the spectral power at  $8.5 \pm 0.1$  kHz, the frequency of the strongest GAM. c) Contour plot of the velocity fluctuation power spectra over the radial range covered by one reflectometer sweep between 61.5 and 73.5 GHz. Overlaid are the detected GAM maxima.

with the previous observations. The safety factor in the GAM measurement region has increased overall in comparison to the low- $\kappa$  limiter phases, and is now at  $3.5 < q < 4.3$ , with the strongest GAM at  $q = 3.7$ . In comparison to the previous cases, the strongest GAM peak is weaker and less distinct from the background. This matches observations from the previous chapter on the scaling of the GAM amplitude in limiter discharges. Overall, regardless of whether the GAM exhibited a multiple eigenmode or a continuum structure during low elongation limiter discharges, it transitions to a single eigenmode GAM of comparable radial width and strength.

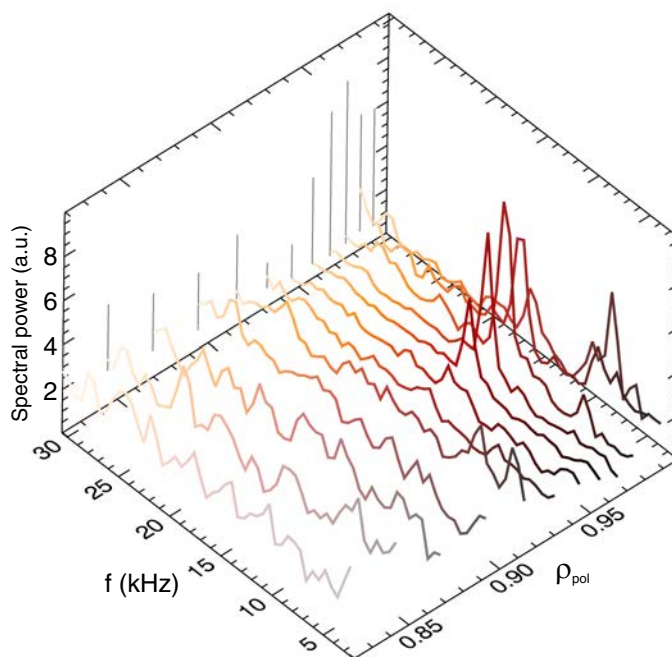


Figure 9.9: Three-dimensional view of the velocity fluctuation power spectra for divertor discharge #29725 with large  $\kappa_b = 1.74$ ,  $t = 0.97\text{--}1.17$  s,  $q_{95} \approx 3.6$ .

The typical radial GAM structure that is observed in divertor discharges is of a similar nature, but with some differences. Figures 9.9 and 9.10 show the GAM structure,  $q$  profile and GAM peak intensity for divertor discharge #29725 during its high-elongation phase at  $\kappa_b = 1.74$ . Both plasma elongation and width of the GAM region are comparable to the high- $\kappa$  limiter phase,  $\Delta_{\text{GAM}} \approx 1$  cm, however the GAM peak is a bit further towards the plasma edge, where the safety factor is  $q \approx 4.3$ . The GAM peak is also much more distinct from the background, even though the overall background power level is increased.

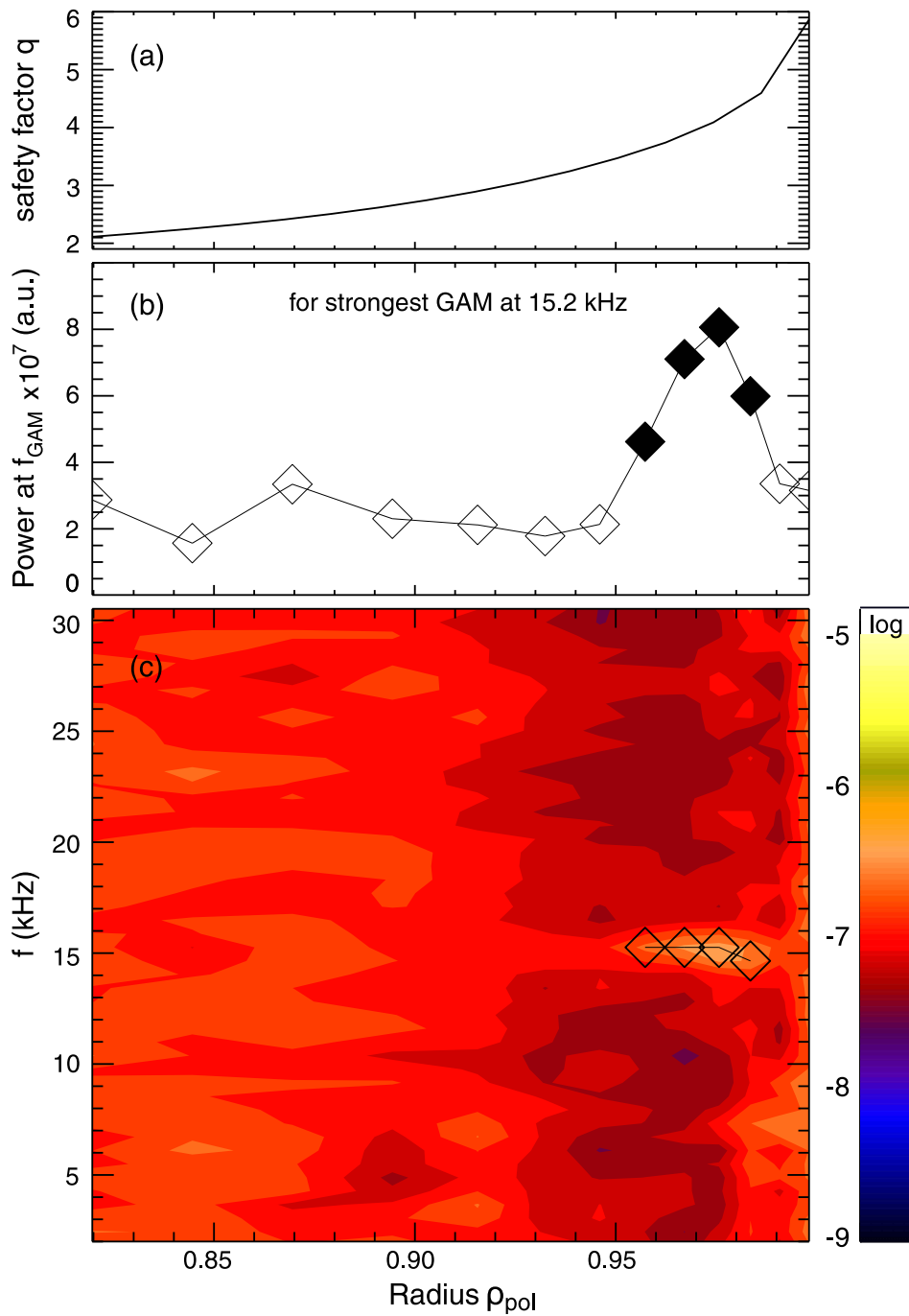


Figure 9.10: Divertor discharge #29725 at  $t = 0.97$ – $1.17$  s and  $\kappa_b = 1.74$ . a) Radial profile of safety factor  $q$ , with  $q_{95} \approx 3.6$ . b) Radial profile of the spectral power at  $15.2 \pm 0.1$  kHz, the frequency of the strongest GAM. c) Contour plot of the velocity fluctuation power spectra over the radial range covered by one reflectometer sweep between 61.5 and 73.5 GHz. Overlaid are the detected GAM maxima.

At the lowest plasma elongation that was reached for divertor discharges in the shape-scan experiments,  $\kappa_b = 1.45$ , the fundamental observations on the GAM structure do not change from the high- $\kappa$  scenario. The width of the GAM plateau does not change, and the GAM remains as a single eigenmode. Only the intensity of the GAM over the background decreases somewhat, approaching the level of the high- $\kappa$  limiter phase from Fig. 9.8.

### 9.2.4 Width of GAM region

Throughout the previous sections, example plots have shown how the radial width of the GAM region,  $\Delta_{\text{GAM}}$ , changes under different discharge conditions. Figure 9.11 shows the behaviour of  $\Delta_{\text{GAM}}$  for the complete dataset, where the tendency of the GAM region to decrease with increasing elongation is seen.

For the GAMs in limiter discharges, the trend is very clear. The widest region of about 4 cm is seen at the lowest elongation ( $\kappa_b \approx 1.15$ ), and as the elongation increases the average width shrinks until it reaches approximately 1 cm (for  $\kappa_b > 1.4$ ). For divertor GAMs, with the exception of one outlier, the width of the GAM region never exceeds 2 cm, and stays relatively constant at the same level of the high- $\kappa$  limiter case.

In conjunction with the previous GAM structure results, this suggests that whenever the GAM becomes locked to a single eigenmode in the plasma edge, the width of the GAM region similarly locks to approximately 1 cm.

## 9.3 GAM propagation

The question of whether the geodesic acoustic mode propagates in the radial direction has been investigated in multiple experiments (see Sec. 3.4.3). The results of these experiments do not give one single answer, as GAM propagation has been observed in both radially inward and outward directions. On ASDEX Upgrade, the propagation of GAMs had not been previously studied, as the diagnostic setup needs to be modified according to the prescription in Sec. 9.1 in order to allow for systematic radial correlation measurements.

As outlined in Sec. 6.4, there are multiple correlation techniques that can be employed to study the radial propagation of the GAM: measuring the inclination of the temporal-spatial cross-correlation contours, calculating the radial derivative

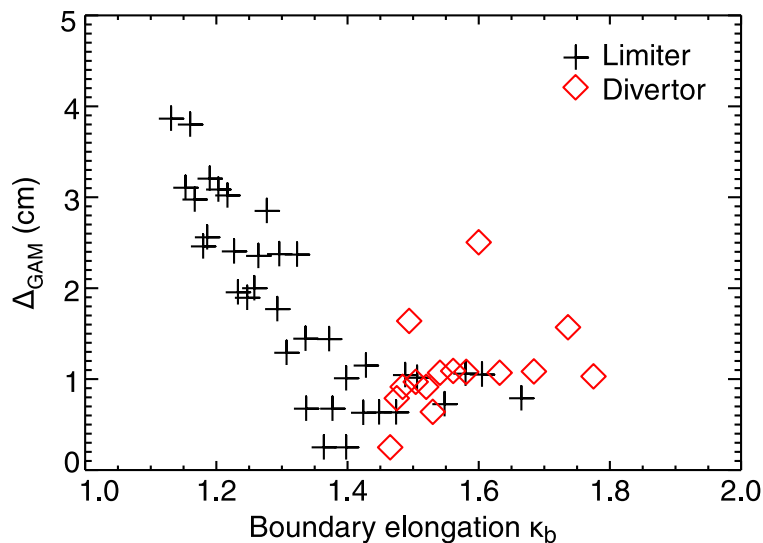


Figure 9.11: The width of the region in which GAMs were observed against the corresponding plasma boundary elongation  $\kappa_b$ , with data from limiter (crosses) and divertor (diamonds) discharges.

of the cross phase at the GAM frequency, or calculating the wavenumber spectrum using a two-point correlation method.

### 9.3.1 Cross-correlation tilt and cross-phase derivative

As outlined in Sec. 9.1, in order to make radial cross-correlation measurements, one reflectometer channel was kept at a constant frequency, while the other channel's frequency is increased stepwise to scan the radial range.

The temporal-spatial cross-correlation  $P_{12}(\tau_l, \rho_{\text{pol}})$  and the radial profile of the cross-phase  $\phi$  at the frequency of the strongest GAM, taken from limiter discharge #29722 during its lowest elongation,  $\kappa_b = 1.12$ , are shown in Figure 9.12. In this phase, the GAM structure showed two neighbouring GAM plateaus. The first channel is probing the plasma edge region at  $\rho_{\text{pol}} = 0.97 \pm 0.005$  with a fixed reference frequency of  $f_{\text{ref}} = 64$  GHz, which places it very close to the centre of a strong eigenmode GAM at 15.9 kHz (cf. Fig. 9.3).

Figure 9.12 (a) shows a contour plot of the cross-correlation between the Doppler shift time series  $f_D(t)$  which are calculated from each channel's raw data, as described in Sec. 6.2. The signals are broadly frequency-filtered over the GAM range of 3–30 kHz. The horizontal axis shows the radial position (the fixed channel is

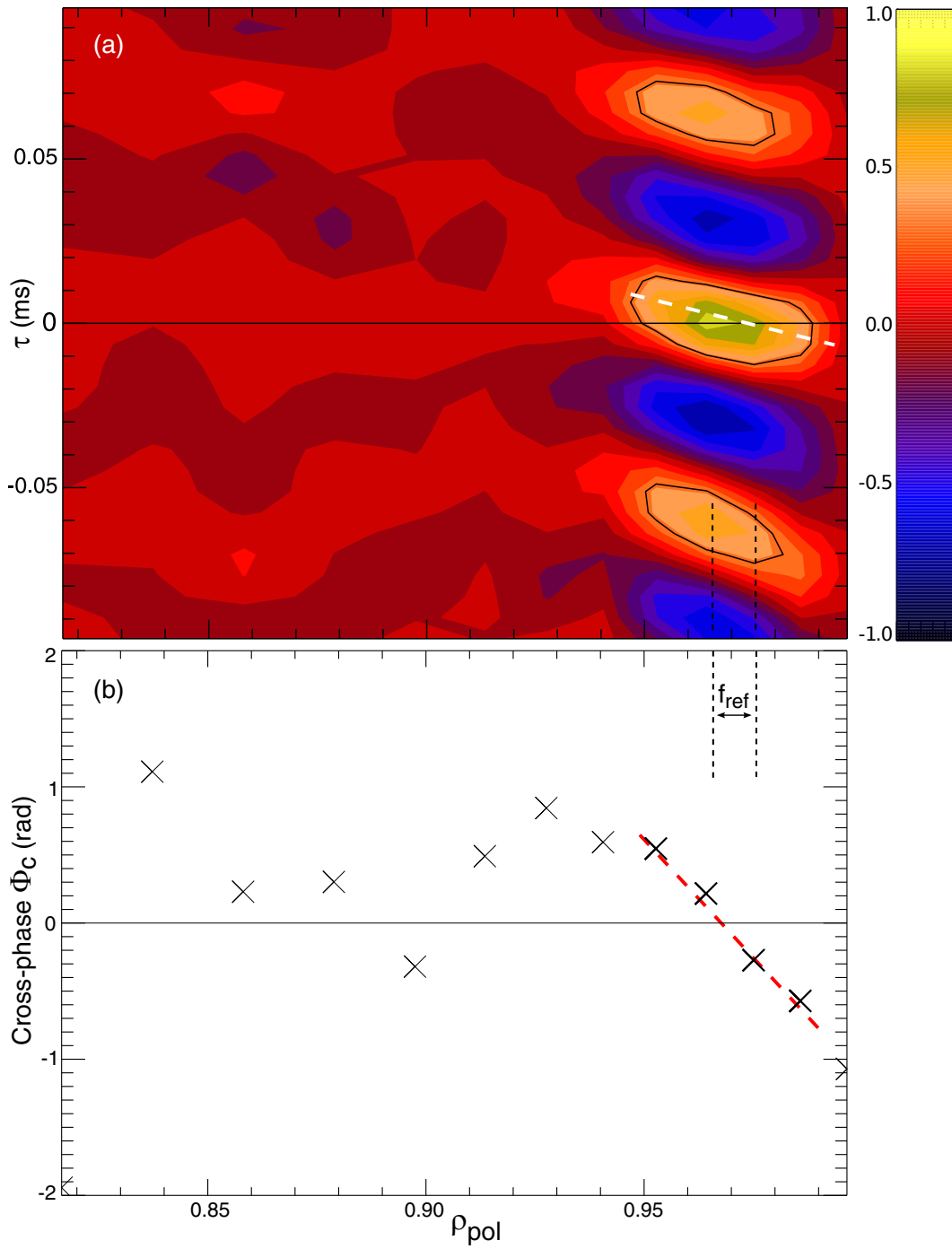


Figure 9.12: AUG limiter discharge #29722 at  $t = 1.15\text{--}1.35\text{ s}$  and  $\kappa_b = 1.12$ . (a) Temporal-spatial cross-correlation  $P_{12}(\tau, \rho_{\text{pol}})$ , with fixed channel at  $\rho_{\text{pol}} = 0.97 \pm 0.005$ . (b) Radial profile of the cross-phase at the frequency of the strongest GAM, 15.9 kHz. Cross-phase derivative in the GAM plateau region:  $\Delta\phi/\Delta r \approx -70 \pm 10 \text{ rad/m}$ .

marked by a black line) and the vertical axis shows the time difference  $\tau_l$ . The strongest cross-correlations are found in the range of  $\rho_{\text{pol}} = 0.95\text{--}0.99$ , which is a direct overlap with the radial region in which the outer eigenmode GAM is observed. As a function of  $\tau_l$  there is an alternation of strong correlation and anti-correlation. The period of this alternation,  $\Delta t = 65$  ms, corresponds to the GAM period, i.e. the inverse of the GAM frequency,  $f_{\text{GAM}}^{-1} = (15.9 \text{ kHz})^{-1} \approx 63$  ms.

A tilt in the correlation pattern is clearly visible in this case. Moving radially inward from the location of the fixed channel, the cross-correlation maximum is shifted towards a positive  $dt$ . This means that the oscillation is delayed with respect to the fixed signal, implying an inward propagation direction. Similarly, this tilt appears to be maintained further outward from the fixed channel, even if the number of data points in that region is very limited. From the tilt angle a radially inward propagation velocity of  $v_r \approx -1.25$  km/s can be estimated.

This observation is matched by considering the radial derivative of the cross-phase at the GAM frequency in Fig. 9.12 (b). Over the range of the GAM plateau, the phase changes linearly with a slope of  $k_r = \Delta\phi/\Delta r \approx -70$  rad/m. From this, the radial propagation velocity can be estimated as  $v_r \approx 2\pi f_{\text{GAM}}/k_r \approx -1.35$  km/s, which is in agreement with the previous result.

The propagation appears to be limited to the range of the locked GAM frequency, as there is no significant correlation with the fixed channel to be found further inside the plasma, for example in the range of the second GAM plateau at  $\rho_{\text{pol}} = 0.90\text{--}0.92$ , implying that the GAM zonal regions are not linked. The radially inward propagation is observed consistently for all limiter GAMs with low elongation, i.e. in both cases with continuum structure and with multiple GAM eigenmodes.

Figure 9.13 shows results from the same discharge during its high-elongation phase, where there is only a single eigenmode GAM in the edge region that can be observed (cf. Fig. 9.8). In this case, there is little to no observable tilt in the pattern, therefore the GAM is in phase over the entire observation region and there close to zero radial propagation. The transition from the pronounced tilt to this state can be observed as the boundary elongation is increased. Note also, due to the decreasing GAM frequency with higher elongation, the time difference between maxima and minima has increased in Fig. 9.13 (a).

The plot of the cross phase at the GAM frequency in Fig. 9.13 (b) confirms that the GAM is in phase across the single eigenmode region.

For the case of GAMs in divertor discharges, where only a single eigenmode

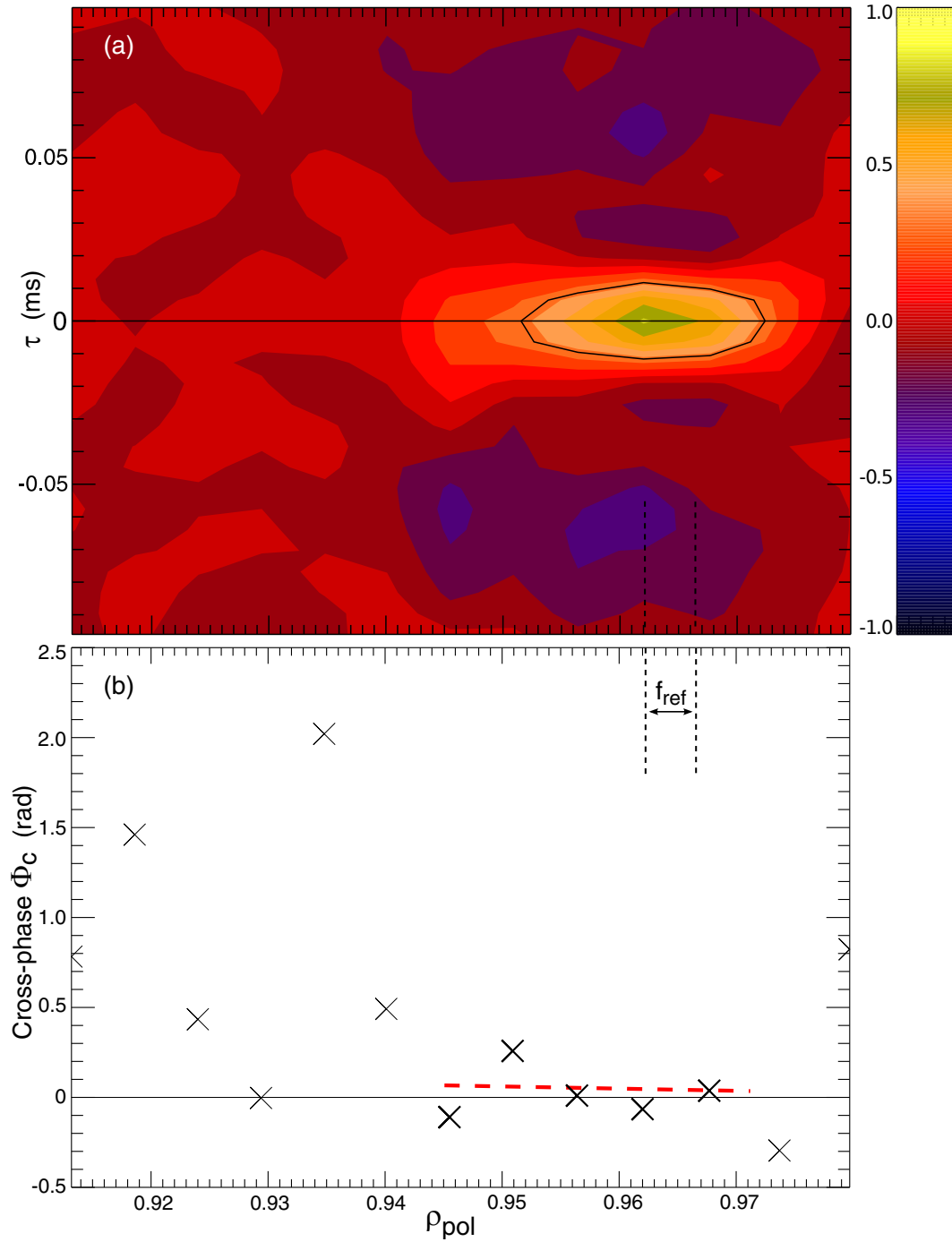


Figure 9.13: AUG limiter discharge #29722 at  $t = 3.50\text{--}3.70$  s and  $\kappa_b = 1.67$ . (a) Temporal-spatial cross-correlation  $P_{12}(\tau, \rho_{\text{pol}})$ , with fixed channel at  $\rho_{\text{pol}} = 0.965 \pm 0.003$ . (b) Radial profile of the cross-phase at the frequency of the strongest GAM, 8.5 kHz. Cross-phase derivative in the GAM plateau region:  $\Delta\phi/\Delta r \approx 0 \pm 5$  rad/m.

GAM is seen, the observations closely correspond to those from the high- $\kappa_b$  limiter discharge. The GAM appears frequency- and phase-locked over the entire GAM observation region, without any significant radial propagation. In general there is no sign of any radially outward GAM propagation in any of the cross-correlation measurements made on ASDEX Upgrade to date.

### 9.3.2 Two-point correlation method

This section reports the determination of the radial propagation velocity by calculating the local frequency and wavenumber spectrum according to the technique by Beall *et al.* [128], which was introduced in Sec. 6.4.

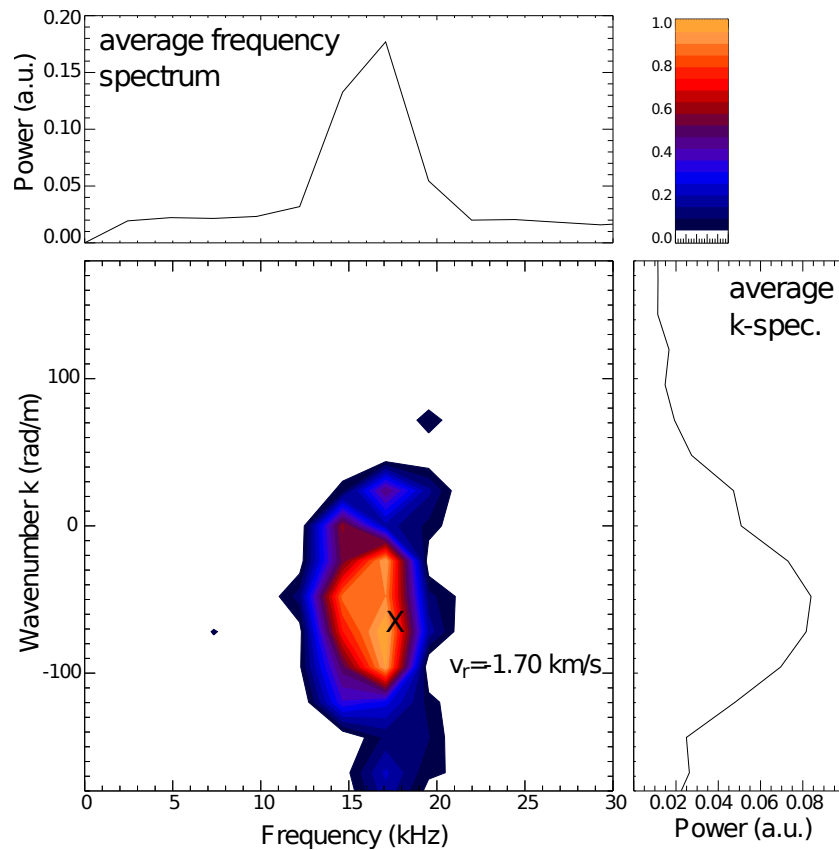


Figure 9.14: Normalised local frequency and wavenumber spectrum  $S_l(\omega, k)$  for limiter discharge #29722 at low elongation,  $\kappa_b = 1.12$ . Maximum:  $f \approx 17.5$  kHz,  $k \approx -65$  rad/m. Top: average frequency spectrum. Right: average wavenumber spectrum.

The two signals used for this analysis are taken from the fixed channel and the

sweeping channel at a point where both are relatively close together. As was seen in the previous section, there is no correlation when the radial separation becomes too large, so it is imperative to pick two points either in the same locked in GAM plateau, or at least nearby during a GAM continuum. Additionally, the radial separation  $\Delta r$  limits the largest measurable wavenumber:  $k_{\max} = \pi/\Delta r$ .

Figure 9.14 shows results for the low-elongation phase of limiter discharge #29722, which was previously analysed via the cross-correlation and phase derivate method in Fig. 9.12. The raw data was taken over  $t = 1.230\text{--}1.245$  s, with the fixed channel at  $\rho_{\text{pol}} = 0.970$  and the sweeping channel at  $\rho_{\text{pol}} = 0.953$ . This places the two channels  $\Delta r \approx 0.8$  cm apart within the same GAM plateau.

The normalised local frequency and wavenumber  $S_l(\omega, k)$  shows a strong peak with a maximum at  $f \approx 17.5$  kHz and  $k \approx -65 \pm 10$  rad/m. The peak shows some spread on both the frequency- and the wavenumber axis. The frequency corresponds closely to the previously measured GAM frequency in the plateau, which was measured as  $f_{\text{GAM}} = 15.9$  kHz at the location of the fixed channel. The negative peak wavenumber indicates radially inward propagation, which agrees with the previous observations. The propagation velocity can be estimated as  $v_r = 2\pi f_{\max}/k_{\max} \approx -1.70$  km/s. This value is a bit larger than the previously determined  $-1.25$  km/s and  $-1.35$  km/s, but it indicates the same direction of propagation, and falls within the same order of magnitude. Within the margins of error for each method of determining the propagation velocity, they all appear to paint the same picture.

Using this method on data from divertor discharges or high-elongation limiter discharges also yields the expected results: a local spectrum  $S_l$  which is peaked around the GAM frequency of the single eigenmode GAM, but which is mostly symmetrical on the  $k$ -axis, indicating no significant radial propagation.

## 9.4 Magnetic GAM signature and structure

Traditionally, the geodesic acoustic mode has mostly been studied by focusing on the associated velocity or density perturbations, which are easily measured with a wide range of diagnostics, such as the Doppler reflectometer. In the fluid picture of the original derivation, the GAM was an electrostatic phenomenon [50]. However, recent theoretical work suggests that the GAM, if seen in the full electromagnetic

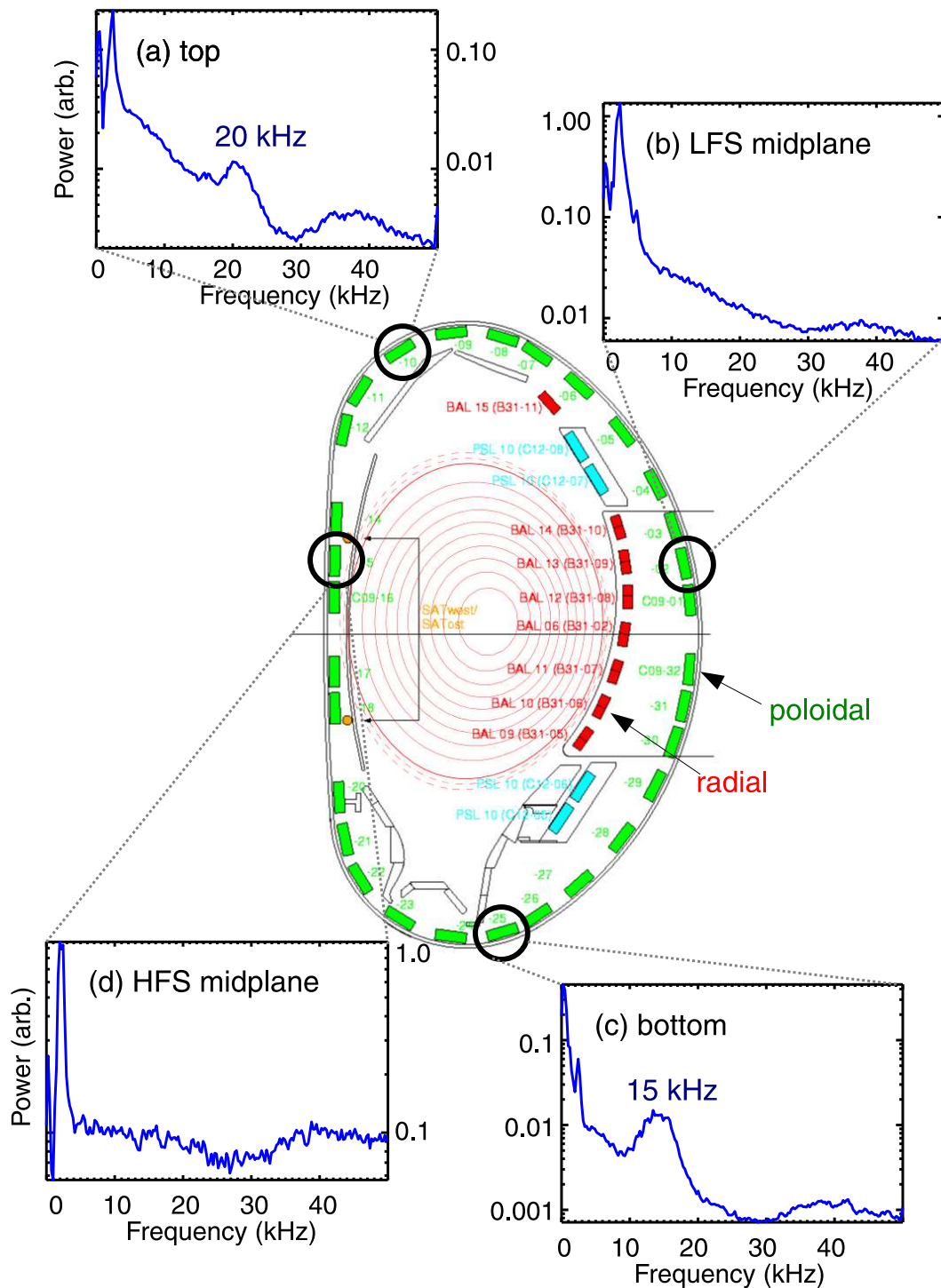


Figure 9.15: Power spectra from selected  $\partial B_\theta/\partial t$  Mirnov coils during low-elongation phase of limiter discharge #29722. Different GAM frequencies, corresponding to the two neighbouring GAM plateaus, are seen at top and bottom, respectively. Coils near the midplane show no GAM.

picture, should also have a measurable magnetic component [148] with a poloidal  $m = 2$  structure [149]. This section presents the first findings on the magnetic GAM signature and structure in ASDEX Upgrade.

As introduced in Sec. 4.3, there is among others a full poloidal set of Mirnov coils measuring variations in the poloidal magnetic field strength. A number of power spectra from selected Mirnov coils in various poloidal positions, for the case of limiter discharge #29722 at low elongation  $\kappa_b = 1.12$ , are shown in Fig. 9.15. This is the same phase and discharge that was discussed in Sec. 9.2.1, i.e. in this case there are two neighbouring eigenmode GAMs at approximately 15 and 22 kHz, respectively.

The example spectra show that, depending on the poloidal position, the magnetic signal can vary strongly. The coils near the midplane, on both high-field side and low-field side, do not show any peak in the GAM frequency range. The bottom coil picks up a distinct peak around 15 kHz, which corresponds to the radially outer GAM. The top coil, however, has a larger peak at about 20 kHz, corresponding to the inner eigenmode GAM, and only a small possible peak near 15 kHz.

The reason for the observation of GAM signatures with different frequencies in different poloidal positions is not clear at this point. In a limiter configuration, the lower coils are slightly further removed from the plasma than the upper coils, which might be responsible for a less strong magnetic signal from the 20 kHz GAM in the lower coil. This, however, would suggest that the 15 kHz GAM signal should still be stronger in the upper coil, which is not the case.

Figure 9.16 shows a number of power spectra from the poloidal Mirnov coils for the high-elongation phase of divertor discharge #29725,  $\kappa_b = 1.74$ . As shown in Sec. 9.2.3, the GAM has a single eigenmode structure in divertor discharges, especially with high elongation. In this case, the GAM was locked to a frequency of approximately 15 kHz. Here there are clear signs of a magnetic GAM signature at this frequency in positions near the top and bottom of the machine, as well as at the high-field side midplane, where no GAM signature could be seen in the limiter case. On the low-field side midplane, however, there is again no clear GAM peak.

In comparison to the limiter results, the magnetic GAM peak is much narrower here. This is an effect of the strong locking to one frequency across the entire GAM region, as opposed to the frequency variation that was found with the two neighbouring plateaus and the small transition region inbetween. The strongest GAM amplitude, as discussed in Sec. 8.1, is of a similar magnitude for low- $\kappa_b$  limiter

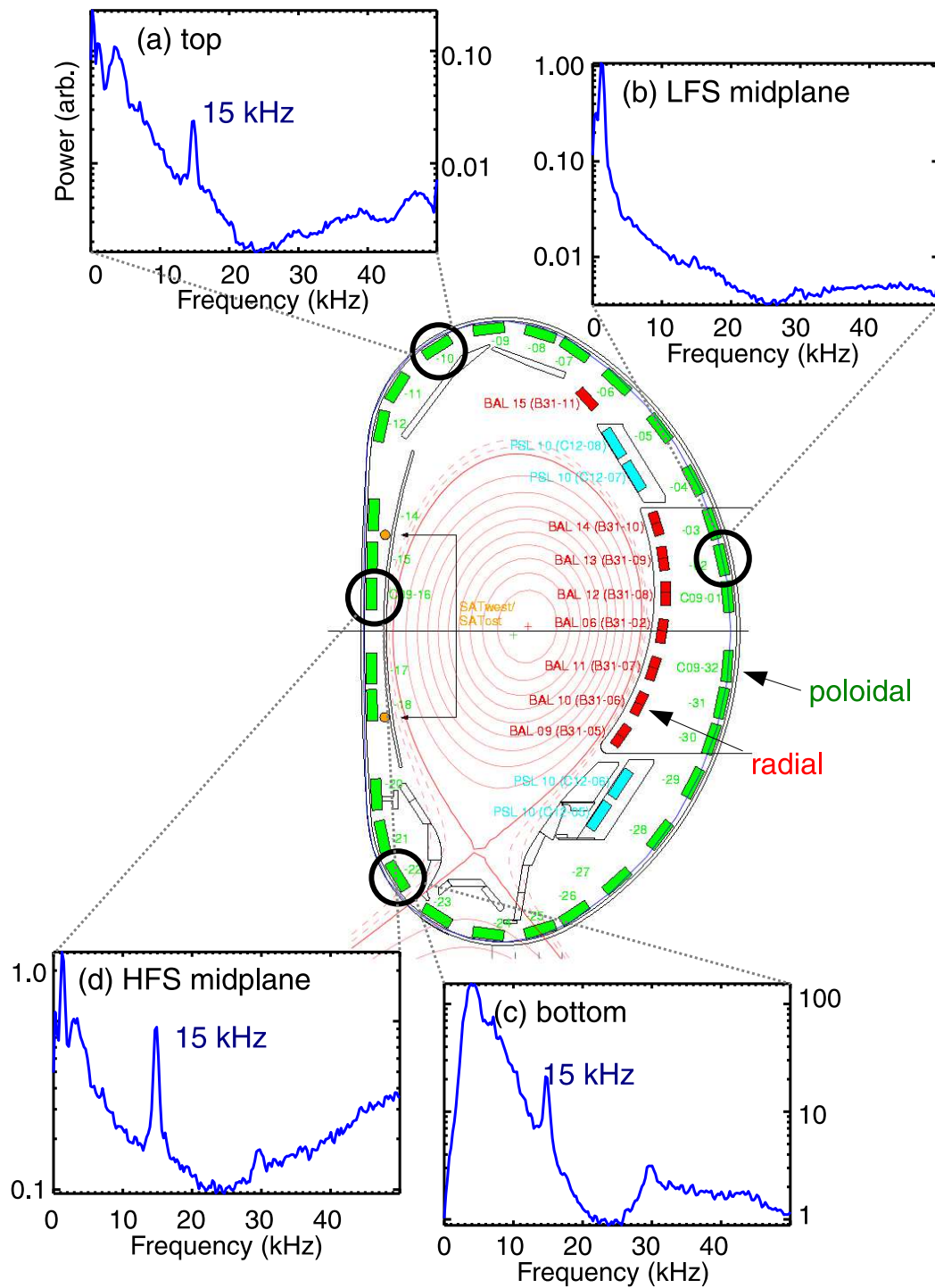


Figure 9.16: Power spectra from selected  $\partial B_\theta / \partial t$  Mirnov coils during high-elongation phase of divertor discharge #29725. One GAM peak near 15 kHz, corresponding to the single eigenmode GAM in this discharge, is seen in the top, bottom, and high-field side coils, with only little evidence near the low-field side midplane.

discharges and high- $\kappa_b$  divertor discharges.

Apart from confirming the presence of a magnetic GAM signature, the poloidal structure of the magnetic signal can also be investigated using this set of Mirnov coils. Of particular interest is whether the expected poloidal mode structure of  $m = 2$  can be confirmed. Figure 9.17 shows results for the cross-correlation between reference coil C09-09 near the top of the vessel (cf. Fig. 4.3) and the other coils in the poloidal ring, for both the limiter and divertor cases which were previously chosen. The signals were frequency-filtered around the range of measured GAM frequencies. It should be noted that choosing a different reference coil, or a different filter for each of the two GAM plateaus in the limiter scenario did not produce any significant deviation in the poloidal structure, apart from an overall rotation of the correlation maxima and minima if the reference coil was changed.

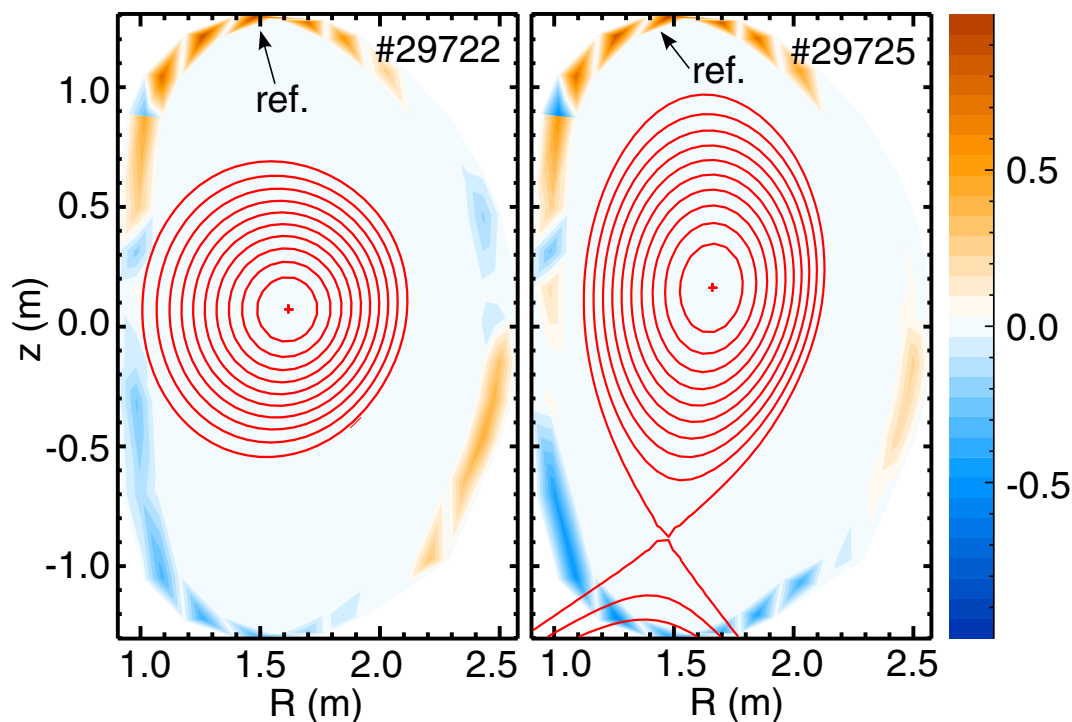


Figure 9.17: Cross-correlation between reference coil C09-09 (top) and the poloidal set of Mirnov coils. Left: limiter discharge #29722 at  $\kappa_b \approx 1.12$ , filtered between 13 and 25 kHz. Right: divertor discharge #29725 at  $\kappa_b \approx 1.75$ , filtered between 10 and 20 kHz.

In both cases, the observed poloidal structure is similar. The strongest positive correlation is found near the reference probe, i.e. centrally above the plasma, but also on the upper high-field side and below the midplane on the low-field side. The

central coils on the bottom, as well as all coils below the midplane on the high-field side are strongly anti-correlated. On the low-field side above the midplane, there is low anti-correlation in the limiter scenario, and no correlation in the divertor case. Overall, the correlation show two maxima and two minima, as would be expected for an  $m = 2$  structure. While the relative lack of poloidal symmetry indicates some deviation from an ideal  $m = 2$  structure, it should be taken into account that the original theory was derived for a circular plasma at large aspect ratio.

These first results indicate that the presence of the X-point could be partially responsible for alterations in the poloidal structure of the magnetic GAM signature, such as the appearance of a peak on the high-field side midplane in Fig. 9.16. The strong shaping effects of the X-point could introduce additional higher  $m > 2$  harmonics on top of the dominant  $m = 2$  structure. In contrast, for measurements from the high- $\kappa_b$  phase of the limiter discharge, where the structure transitions to a single eigenmode GAM similar to the divertor case, albeit with lower GAM amplitude, there is still no observable magnetic GAM signature on the high-field side midplane. It is also possible that the overall noise level in the limiter case is stronger, and the GAM can therefore not be seen in the magnetic signal.

## 9.5 Discussion

This chapter presents experimental results on the structure of the GAM, its radial propagation as well as its magnetic signature and poloidal structure. A specialised experimental setup was chosen for the Doppler reflectometer systems to allow simultaneous measurements from the same poloidal angle at different radial positions.

Previous ASDEX Upgrade experiments have shown that the GAM structure can significantly vary depending on the plasma configuration [65]. The set of shape-scan experiments that were used in this analysis allowed the observation of the GAM in both limiter and divertor configuration at various levels of elongation. During these discharges, three different modes of the GAM structure could be identified: single eigenmode GAM, multiple eigenmode GAMs and continuum GAM. In the first case, the GAM is observed in a single radial plateau, where its frequency is nearly constant. This is the case in all measurements made in divertor plasmas, as well as in limiter plasmas at sufficiently high elongation ( $\kappa_b > 1.35$ ). The other two cases are found in limiter plasmas at lower elongation. In a multiple eigenmode

structure, the GAM frequency is similarly locked near the plasma edge. However, further inside the plasma, a second region with a locked GAM frequency can be observed. In the continuum case, the GAM frequency is not locked, but changes radially. Both continuum and multiple eigenmode structures can be observed to transition to a single eigenmode state as the plasma elongation is increased.

Similar transitions in the GAM structure have been observed at other devices: at TCV, the GAM changed its structure from a single eigenmode to a continuum GAM as the edge safety factor was significantly raised [82]. In the ASDEX Upgrade case, the change in  $q_{95}$  was less strong, however, and in the opposite direction. In experiments at DIII-D, a transition from a multiple eigenmode GAM to a continuum GAM was observed in concurrence with a transition from an L-mode plasma to an Ohmic regime [81].

The width of the observable GAM region appears to be strongly coupled to the plasma elongation. The stronger the plasma deviates from a circular shape, the smaller the GAM region becomes. Previously, this observation has also been linked to the density profile shape [60, 65]: whereas divertor plasmas typically have a density pedestal, with the GAM only measured outside the pedestal, the density profile is more parabolic in limiter plasmas. As can be seen from the density profiles in Fig. 7.3, the limiter discharge in fact begins to develop a density pedestal as the elongation is increased and the GAM observation width shrinks.

The radial propagation of the GAM is also influenced by the GAM structure and the plasma elongation. In the case of low  $\kappa_b$ , i.e. in the continuum or multiple eigenmode regimes, the GAM can be observed to propagate radially inwards at a velocity of approximately 1.5 km/s. In the case of a single eigenmode, the GAM appears to be phase-locked across the entire plateau, without any sign of radial propagation. Radially outward propagation is not observed.

The experiments also confirm that the magnetic signature of the GAM can be observed by the poloidal Mirnov coils. In the case of multiple GAM plateaus, both dominant GAM frequencies are picked up by some, but not all, of the coils. For single eigenmode divertor GAMs, the magnetic signature can also be observed at the midplane on the high-field side, whereas in general the GAM is best seen near the top and bottom of the machine. Cross-correlation measurements show an approximate  $m = 2$  poloidal structure of the GAM, which is in agreement with theoretical predictions [149]. Previous results from TCV have shown a similar poloidal structure with some deviations [64]. Mirnov coil measurements at DIII-D have confirmed

a toroidal  $n = 0$  structure, however only gave an approximate result of  $m \approx 0$  for the poloidal structure [81].

In summary, this chapter presents results on the GAM radial structure, GAM propagation and the poloidal magnetic GAM structure based on the extensive database of ASDEX Upgrade measurements that was established for this thesis. Three distinct types of radial structure are identified and transitions between them during variations of the plasma geometry are observed for the first time. For accurate descriptions of GAM behaviour, and for predictions of GAM frequency scaling, current models will need to be extended to account for these GAM structure observations. The width of the GAM region is found to be related to the plasma elongation. For the first time at ASDEX Upgrade, the magnetic signature of the GAM is detected. Its poloidal  $m = 2$  structure is confirmed, in agreement with theoretical predictions.

# Chapter 10

## Summary and conclusion

The goal of this thesis was the measurement and characterisation of fundamental properties of the geodesic acoustic mode (GAM), such as its radial structure and its scaling behaviour, i.e. GAM frequency and amplitude, under variations of the plasma configuration and geometry. Since the GAM has been shown play a central role in the moderation of plasma turbulence and turbulent transport through shear flows and the transition to the H mode, understanding these fundamental properties is essential. The measurements of these GAM properties were obtained using a V-band (50–75 GHz) X-mode Doppler reflectometer system during L-mode discharges in the ASDEX Upgrade tokamak. The flexible shaping capabilities of ASDEX Upgrade allowed for a set of experiments, during which the plasma shape was scanned between nearly circular and highly vertically elongated states, in both limiter and divertor (i.e. X-point) configurations, which, based on previous research was expected to impact all of the above-mentioned fundamental GAM properties [60, 65, 66, 69, 79].

Based on these experiments, the three key goals which were stated in the introduction to this thesis can now be addressed:

- *Characterising the GAM frequency scaling behaviour as a function of plasma geometry and comparing it to theoretical and empirical models.*

While the plasma shape was varied, including the stretching of the boundary elongation in the range  $1.12 < \kappa_b < 1.69$  for limiter discharges and  $1.44 < \kappa_b < 1.77$  in the divertor case, GAMs were identified in the plasma edge region. For each radial scan, properties of the strongest detected GAM were compiled in a database, which was then used for comparisons to numerous models. The original fluid model by Winsor [50], which only considers

local sound velocity  $c_s$  and safety factor  $q$ , overestimated the GAM frequency, especially for GAMs near the last closed flux surface in high- $\kappa_b$  scenarios. Better agreement, especially for edge GAMs was found with the fluid model by Angelino [73], which takes the local plasma elongation  $\kappa$  into account and replicates the observed trend of lower  $f_{\text{GAM}}$  at higher elongation. The heuristic model by Conway [65], which was first developed after observing these deviations from the expected scaling for high- $\kappa_b$  edge GAMs, gave reasonable agreement with the data, in particular for edge limiter GAMs. The gyrokinetic model by Gao [71], which considers not just  $q$  and  $\kappa$  but also the Shafranov shift gradient  $\Delta'$  and the radial derivative of  $\kappa$ , was shown to give a lower boundary estimate of the GAM frequency, where non-linear effects might play a role in the upshift of the experimental GAM frequency. An accurate physics-based model for prediction of the experimental GAM frequency, which is impacted by a multitude of factors, has still not been obtained. The development of such a model is paramount for the prediction of GAM behaviour in scenarios which differ significantly from the experimental conditions available today. However, between the lower boundary estimate from Gao's gyrokinetic scaling and the predictions from Angelino's fluid scaling, a rather narrow range of expected GAM frequencies can be estimated for most discharge conditions.

- *Investigating the behaviour of the GAM amplitude during variation of the plasma geometry, and relating it to collisional and collisionless GAM damping rates as predicted by multiple models.*

The GAM amplitude results from a balance of turbulence drive, collisional and collisionless damping, as well as energy transfer processes. The collisionless GAM damping rates, which have been the focus of most theoretical work on GAM damping, usually strongly depend on local safety factor  $q$  and the GAM frequency, which in turn is heavily influenced by  $\kappa$ , as was learned in the GAM frequency scaling investigation. In a direct comparison of the GAM amplitude against  $q$  and  $\kappa_b$ , limiter discharges showed decreasing GAM amplitude with increasing  $\kappa_b$ , until settling at a relatively constant level for  $\kappa_b > 1.3$ . In divertor discharges, where  $\kappa_b$  is always above this threshold value, no clear influence of the elongation was observed, however the GAM amplitude increased for larger values of  $q$ . Looking at subsets of the data with similar turbulence drive, these trends persisted.

A comparison of GAM damping rates predicted for GAMs in the ASDEX Upgrade conditions showed that the collisional damping rate, which depends on the ion collisionality [145], cannot be neglected and may in fact explain some of the experimental observations. In the limit of negligible radial GAM wavenumber [144], the collisionless damping rate would be orders of magnitude below the collisional damping rate for the entire region of GAM observation. However, according to theory and simulations, finite orbit width effects need to be considered [72, 134, 135, 145], resulting in significantly larger damping rates. For ASDEX Upgrade parameters, the so-called large orbit drift width limit was shown to apply [70, 71, 137], resulting in dominant collisional damping for edge GAMs ( $\rho_{\text{pol}} > 0.95$ ) and similar orders of magnitude of collisional and collisionless damping for GAMs towards the core. A comparison of the GAM amplitude in the edge of divertor plasmas to the collisional damping rate supported this observation. An important conclusion from this is that simulations which do not take collisions into account will not accurately model GAM behaviour for ASDEX Upgrade parameters.

- *Identifying the structure and radial propagation of the GAM.*

The radial structure of the GAM had previously been observed to vary substantially depending on plasma configuration [65, 81, 82]. During the experiments for this thesis, three distinct types of radial structure were identified. In the case of the continuum GAM, which was observed for limiter discharges at low elongation, the GAM frequency changes radially, as would be expected from the frequency scaling laws where  $f_{\text{GAM}}$  depends on the local electron and ion temperatures  $T_e$  and  $T_i$ . A second structure that was identified in low- $\kappa_b$  limiter discharges is the multiple eigenmode state, where two neighbouring plateaus with locked GAM frequency are observed. For continuum GAMs, the strongest GAM was seen further inside the plasma, while in the multiple eigenmode case the GAMs in the plateau near the edge had the higher amplitude. As the boundary elongation was increased and approached a threshold value of  $\kappa_b \approx 1.35$ , the width of the region in which GAMs were detected was observed to shrink in both cases, as they transitioned to the third type of structure, the single eigenmode GAM. In this state, which was also found for all GAMs in divertor discharges (where  $\kappa_b > 1.35$  is always the case), the GAM appeared in a narrow region near the plasma edge, with a single dominant frequency.

The decrease in the width of the GAM region and the transition to a single eigenmode state for limiter GAMs appears to be coupled to the decrease of the limiter GAM amplitude, which follows the same curve.

Radial correlation Doppler measurements during the same experiments allowed the investigation of the GAM radial propagation, which had previously been observed in both radially inward and outward directions at other experiments [56,64,83,84]. Analysis with two correlation techniques showed evidence of a radially inward propagation velocity, in the range of 1–2 km/s, for low- $\kappa_b$  limiter discharges in both continuum and multiple eigenmode states. However, for increased elongation, as the structure transitioned to the single eigenmode state, and therefore also in all divertor discharges, no radial propagation could be observed within the measurement uncertainties.

First ASDEX Upgrade results for detecting the GAM's magnetic signature and its poloidal structure were also presented. Correlation measurements indicated agreement with the theoretically predicted poloidal  $m = 2$  structure [149], but suggest that  $m > 2$  components might be present due to the strong shaping impact of the X-point. The strength of the magnetic signature was shown to vary depending on the poloidal angle and the GAM radial structure. While the GAM magnetic signature was always observed near the top and bottom of the plasma, it was only visible on the high-field side midplane for single eigenmode divertor GAMs, which were shown to have strong GAM amplitude peaks. In the case of a multiple eigenmode structure, the GAM frequency of both the inner and the outer plateau could be detected, however at different poloidal positions. This behaviour is not yet fully understood and warrants further investigation.

In summary, for the research presented in this thesis, a unique set of shape-scan discharges was performed and has been thoroughly documented in an extensive database. From comparison with multiple theoretical models for the GAM frequency scaling, it was learned that the current models, while reproducing the general expected  $c_s/R_0$  trend, are insufficient for accurate prediction of the experimental GAM frequency. The plasma boundary elongation was confirmed to have a large impact on the GAM frequency. The investigation of GAM damping rates demonstrated that collisionless Landau damping rates from models that neglect finite orbit width effects are far too low to affect GAM behaviour in the edge region. When these ef-

fects are included, the collisionless damping rates are significantly higher. However, it was also learned that, for typical ASDEX Upgrade conditions, damping due to particle collisions is of a similar order of magnitude and cannot be neglected. For GAMs in the very edge region, collisional damping was found to be dominant, and appeared to have a direct impact on the GAM amplitude. The most important takeaway from the GAM structure investigations is that the GAM radial structure can fundamentally change, depending on the discharge parameters. The expected continuum GAM with radially varying local GAM frequency proportional to the local sound velocity was only found in limiter discharges with low elongation. In the more typical scenario of a highly-elongated plasma in divertor configuration, the GAM was only observed in an eigenmode-like state with constant frequency over a narrow radial region near the very edge of the plasma.

This means that the current theoretical models and numerical approaches for the study of GAMs and their role in complex plasma turbulence system have severe shortcomings which need to be addressed: frequency scaling models need to incorporate more effects than they currently do, in particular they have to account for the GAM structure and the possible presence of an eigenmode GAM; models for GAM damping and for the prediction of the GAM amplitude need to account for both collisionless and collisional processes, under consideration of finite orbit width effects.

As an outlook for future GAM research, these results suggest multiple promising directions. The impact of the collisional damping rate on the GAM amplitude should be studied in more detail, by performing experiments in which the ion collisionality is varied purposefully for plasmas in elongated divertor configurations, where strong single eigenmode edge GAMs are found. Simultaneous measurements of the ion collisionality, GAM amplitude, GAM frequency, the background turbulence level and the turbulence correlation length should provide further insights into the role of the geodesic acoustic mode in turbulence moderation.

Based on the GAM structure observations, a new set of experiments should also be able to answer the open question of what parameter determines whether the multiple eigenmode state or the continuum state is encountered in low- $\kappa_b$  limiter plasmas. In DIII-D, a transition from multiple eigenmode state to a continuum GAM was observed after external heating was turned off in a discharge [81]. There-

fore, measurements in an otherwise stable, low- $\kappa_b$  discharge in which the heating is increased step by step, should show whether such a transition can be induced at ASDEX Upgrade, and a transition threshold can be identified.

For future investigations of the GAM frequency and amplitude scaling, interaction with theory and modelling appears essential for a full understanding. While there are some isolated models for incorporating, for example, the effects of impurities or toroidal rotation, the development of a comprehensive model that takes into account all of the major factors should be an aim. In particular, a way to estimate the magnitude of non-linear effects would be helpful. Another point that is not accounted for in the current GAM frequency scaling models is the radial GAM structure. While radially locked eigenmodes are the norm, rather than the exception, theoretical models usually describe a GAM continuum. For a more accurate prediction of the GAM frequency, this must be taken into consideration. First results from gyrokinetic GENE simulations for TCV parameters are able to replicate the transition from a global eigenmode GAM to a continuum GAM [150]. Similar simulations for ASDEX Upgrade parameters should enhance the understanding of the experimental results.

Finally, the influence of the plasma isotope on the GAM properties should be studied in more detail. The isotope mass has a direct influence on the sound velocity, and therefore on the GAM frequency. If a sufficiently accurate predictive model for the GAM frequency is found, then variations in the GAM frequency could be taken as an indication of the isotope ratio in the plasma. In D-T plasmas at ITER, where other influence on the GAM such as the shape or the  $q$  profile are expected to be known and kept constant, such a measurement would be highly useful. Additionally, investigating the strength of the GAM amplitude under variations of the isotope is of interest, as the GAM has been speculated to be a contributor to the so-called isotope effect, where plasma confinement was shown to improve unexpectedly when moving from hydrogen to deuterium and tritium plasmas.

# Bibliography

- [1] J. Freidberg, *Plasma Physics and Fusion Energy* (Cambridge University Press, New York, USA, 2007)
- [2] F.F. Chen, *Introduction to Plasma Physics and Controlled Fusion - Volume 1: Plasma Physics* (Plenum Press, New York, USA, 1984)
- [3] U. Stroth, *Plasmaphysik - Phänomene, Grundlagen, Anwendungen* (Vieweg+Teubner, Wiesbaden, Germany, 2011)
- [4] J. Wesson, *Tokamaks - Fourth Edition* (Oxford University Press, Oxford, UK, 2011)
- [5] J. Schirmer, *Plasma Turbulence Studies Using Correlation Doppler Reflectometry on the ASDEX Upgrade Tokamak*, Ph.D. thesis, Ludwig-Maximilians-Universität München (2005)
- [6] S. Klenge, *Dynamik magnetisch eingeschlossener Plasmen am L-H Übergang*, Ph. D. thesis, University of Stuttgart (2005)
- [7] M.G. Dunne, *Inter-ELM evolution of the edge current density profile on the ASDEX upgrade tokamak*, Ph.D. thesis, University College Cork (2013)
- [8] F. Wagner *et al.*, Phys. Rev. Lett. **49**, 1408 (1982)
- [9] G.D. Conway *et al.*, Plasma Fusion Res. **5**, S2005 (2010)
- [10] G.D. Conway *et al.*, Phys. Rev. Lett. **106**, 065001 (2011)
- [11] A.J. Wootton *et al.*, Phys. Fluids B **2**, 2879 (1990)
- [12] J.W. Connor, Plasma Phys. Control. Fusion **35**, B293 (1993)
- [13] R. Sabot *et al.*, Plasma Phys. Control. Fusion **48**, B421 (2006)
- [14] R.J. Fonck *et al.*, Phys. Rev. Lett. **70**, 3736 (1993)
- [15] G.R. McKee *et al.*, Nucl. Fusion **41**, 1235 (2001)

- 
- [16] K. Rahbarnia *et al.*, Plasma Phys. Control. Fusion **50**, 085008 (2008)
  - [17] B.D. Scott, Plasma Phys. Control. Fusion **45**, A385 (2003)
  - [18] A.N. Kolmogorov, Dokl. Akad. Nauk SSSR **30**, 301 (1941)
  - [19] A.N. Kolmogorov, Dokl. Akad. Nauk SSSR **32**, 16 (1941)
  - [20] T. Happel, *Doppler reflectometry in the TJ-II stellarator: Design of an optimized Doppler reflectometer and its application to turbulence and radial electric field studies*, Ph.D. thesis, Universidad Carlos III de Madrid (2010)
  - [21] R.H. Kraichnan, Phys. Fluids **10**, 1417 (1967)
  - [22] R.H. Kraichnan, J. Fluid Mech. **47**, 525 (1971)
  - [23] G.D. Conway, Plasma Phys. Control. Fusion **50**, 124026 (2008)
  - [24] C. Lechte, *Microscopic Structure of Plasma Turbulence in the Torsatron TJ-K*, Ph.D. thesis, Christian-Albrechts-Universität zu Kiel (2003)
  - [25] B. Coppi *et al.*, Phys. Fluids **10**, 582 (1967)
  - [26] S.C. Cowley *et al.*, Physics Fluids B **3**, 2767 (1991)
  - [27] F. Jenko *et al.*, Phys. Plasmas **7**, 1904 (2000)
  - [28] A.D. Gurchenko and E.Z. Gusakov, Plasma Phys. Control. Fusion **52**, 124035 (2010)
  - [29] N.T. Howard *et al.*, Phys. Plasmas **20**, 032510 (2013)
  - [30] D. Told *et al.*, Phys. Plasmas **20**, 122312 (2013)
  - [31] B.B. Kadomtsev and O. P. Pogutse, Nucl. Fusion **11**, 67 (1971)
  - [32] D.R. Ernst *et al.*, Phys. Plasmas **11**, 2637 (2004)
  - [33] F. Merz and F. Jenko, Nucl. Fusion **50**, 054005 (2010)
  - [34] P.H. Diamond *et al.*, Plasma Phys. Control. Fusion **47**, R35 (2005)
  - [35] D.R. Ernst *et al.*, Phys. Plasmas **16**, 055906 (2009)
  - [36] D.R. Smith *et al.*, Phys. Rev. Lett. **102**, 225005 (2009)
  - [37] U. Stroth, *Plasmaphysik - Phänomene, Grundlagen, Anwendungen - Second Edition* (in preparation)
  - [38] H. Biglari *et al.*, Phys. Fluids B **2**, 1 (1990)

- 
- [39] R.J. Groebner *et al.*, Phys. Rev. Lett. **64**, 3015 (1990)
- [40] K.H. Burrell *et al.*, Plasma Phys. Control. Fusion **34**, 1859 (1992)
- [41] B. Scott, Phys. Plasmas **7**, 1845 (2000)
- [42] G.T. Hoang *et al.*, Nucl. Fusion **38**, 117 (1998)
- [43] G.D. Conway *et al.*, Plasma Phys. Control. Fusion **44**, 1167 (2002)
- [44] H.Y. Yuh *et al.*, Phys. Rev. Lett. **106**, 055003 (2011)
- [45] K. Itoh *et al.*, Phys. Plasmas **13**, 055502 (2006)
- [46] G. Birkenmeier, *Experimentelle Untersuchungen zur Struktur und Dynamik von Driftwellenturbulenz in Stellaratorgeometrie*, Ph.D. thesis, Universität Stuttgart (2012)
- [47] P. Manz *et al.*, Phys. Rev. Lett. **103**, 165004 (2009)
- [48] P.H. Diamond and Y.-B. Kim, Phys. Fluids B **3**, 1626 (1991)
- [49] A.M. Dimits *et al.*, Phys. Plasmas **7**, 969 (2000)
- [50] N. Winsor *et al.*, Phys. Fluids **11**, 2448 (1968)
- [51] A. Fujisawa *et al.*, Nucl. Fusion **47**, S718 (2007)
- [52] A. Fujisawa, Nucl. Fusion **49**, 013001 (2009)
- [53] G.R. Tynan *et al.*, Plasma Phys. Control. Fusion **51**, 113001 (2009)
- [54] P.H. Diamond *et al.*, Plasma Phys. Control. Fusion **53**, 124001 (2011)
- [55] K.J. Zhao *et al.*, Phys. Rev. Lett. **96**, 255004 (2006)
- [56] Y. Xu *et al.*, Plasma Phys. Control. Fusion **53**, 095015 (2011)
- [57] P.M. Schoch *et al.*, Rev. Sci. Instrum. **74**, 1846 (2003)
- [58] T. Ido *et al.*, Nucl. Fusion **46**, 512 (2006)
- [59] G.R. McKee *et al.*, Phys. Plasmas **10**, 1712 (2003)
- [60] G.D. Conway *et al.*, Plasma Phys. Control. Fusion **47**, 1165 (2005)
- [61] J.C. Hillesheim *et al.*, Phys. Plasmas **19**, 022301 (2012)
- [62] A. Krämer-Flecken *et al.*, Phys. Rev. Lett. **97**, 045006 (2006)
- [63] A.V. Melnikov *et al.*, Plasma Phys. Control. Fusion **48**, S87 (2006)

- 
- [64] C.A. de Meijere *et al.*, Plasma Phys. Control. Fusion **56**, 072001 (2014)
- [65] G.D. Conway *et al.*, Plasma Phys. Control. Fusion **50**, 055009 (2008)
- [66] G.R. McKee *et al.*, Plasma Phys. Control. Fusion **48**, S123 (2006)
- [67] J.R. Robinson *et al.*, Plasma Phys. Control. Fusion **54**, 105007 (2012)
- [68] A.Yu. Yashin *et al.*, Nucl. Fusion **54**, 114015 (2014)
- [69] A. Storelli *et al.*, Phys. Plasmas **22**, 062508 (2015)
- [70] Z.Y. Qiu *et al.*, Plasma Phys. Control. Fusion **51**, 012001 (2009)
- [71] Z. Gao, Plasma Science and Technology **13**, 15 (2011)
- [72] H. Sugama and T.H. Watanabe, J. Plasma Physics **72**, 825 (2006)
- [73] P. Angelino *et al.*, Phys. Plasmas **15**, 062306 (2008)
- [74] W. Guo *et al.*, Phys. Plasmas **17**, 112510 (2010)
- [75] H. Ren, Phys. Plasmas **21**, 044505 (2014)
- [76] V.P. Lakhin *et al.*, Phys. Lett. A **374**, 4872 (2010)
- [77] J. Yu and X. Gong, Nucl. Fusion **53**, 123027 (2013)
- [78] P. Simon *et al.*, Plasma Phys. Control. Fusion **58**, 045029 (2016)
- [79] G.D. Conway *et al.*, Plasma Phys. Control. Fusion **50**, 085005 (2008)
- [80] K. Itoh *et al.*, Plasma Fusion Res. **1**, 037 (2006)
- [81] G. Wang *et al.*, Phys. Plasmas **20**, 092501 (2013)
- [82] Z. Huang *et al.*, Proc. 41st EPS Conf. on Plasma Physics. (Berlin, Germany), P5.071 (2014)
- [83] D.F. Kong *et al.*, Nucl. Fusion **53**, 113008 (2013)
- [84] T. Lan *et al.*, Phys. Plasmas **15**, 056105 (2008)
- [85] A.D. Liu *et al.*, Phys. Rev. Lett. **103**, 095002 (2009)
- [86] T. Kobayashi *et al.*, Phys. Rev. Lett. **111**, 035002 (2013)
- [87] G.S. Xu *et al.*, Nucl. Fusion **54**, 103002 (2014)
- [88] I. Cziegler *et al.*, Phys. Plasmas **20**, 055904 (2013)

- 
- [89] G.R. Tynan *et al.*, Plasma Phys. Control. Fusion **58**, 044003 (2016)
- [90] A. Herrmann and O. Gruber, Fusion Sci. Technol. **44**, 569 (2003)
- [91] R. Neu *et al.*, Plasma Phys. Control. Fusion **49**, B59 (2007)
- [92] R. Neu *et al.*, J. Nucl. Mater. **438**, S34 (2003)
- [93] A. Herrmann *et al.*, Nucl. Fusion **55**, 063015 (2015)
- [94] B. Plöckl and P.T. Lang, Rev. Sci. Instrum. **84**, 103509 (2013)
- [95] W. Suttrop *et al.*, Fus. Eng. Des. **88**, 446 (2013)
- [96] A. Kappatou, *Investigations of helium transport in ASDEX Upgrade plasmas with charge exchange recombination spectroscopy*, Ph.D. thesis, Technische Universiteit Eindhoven (2014)
- [97] K.-D. Zastrow *et al.*, Nucl. Fusion **38**, 257 (1998)
- [98] B. Streibl *et al.*, Fusion Sci. Technol. **44**, 578 (2003)
- [99] M. Bornatici *et al.*, Nucl. Fusion **23**, 1153 (1983)
- [100] J. Stober *et al.*, EPJ Web of Conferences **32**, 02011 (2012)
- [101] R. Dux *et al.*, J. Nucl. Mater. **313**, 1150 (2003)
- [102] H. Faugel *et al.*, Fus. Eng. Des. **74**, 319 (2005)
- [103] I.G.J. Classen *et al.*, Rev. Sci. Instrum. **81**, 10D929 (2010)
- [104] E. Viezzer *et al.*, Rev. Sci. Instrum. **83**, 103501 (2012)
- [105] B. Kurzan and H.D. Murmann, Rev. Sci. Instrum. **82**, 103501 (2011)
- [106] A. Mlynek *et al.*, Rev. Sci. Instrum. **81**, 033507 (2010)
- [107] A. Mlynek *et al.*, Fusion Sci. Technol. **61**, 290 (2012)
- [108] J. Schweinzer *et al.*, Plasma Phys. Control. Fusion **34**, 1173 (1992)
- [109] E. Wolfrum *et al.*, Rev. Sci. Instrum. **77**, 033507 (2006)
- [110] E. Holzhauser *et al.*, Plasma Phys. Control. Fusion **40**, 1869 (1998)
- [111] M. Hirsch *et al.*, Plasma Phys. Control. Fusion **43**, 1641 (2001)
- [112] A. Silva *et al.*, Rev. Sci. Instrum. **67**, 4138 (1997)
- [113] B. Kurzan *et al.*, Plasma Phys. Control. Fusion **42**, 237 (2000)

- 
- [114] E. Poli *et al.*, Comput. Phys. Commun. **136**, 90 (2001)
- [115] E. Viezzer *et al.*, Nucl. Fusion **53**, 053005 (2013)
- [116] H.W. Müller *et al.*, Nucl. Fusion **51**, 073023 (2011)
- [117] P. Hennequin *et al.*, Proc. 7th Int. Reflectometry Workshop, Garching (2005)
- [118] M. Hirsch *et al.*, Plasma Phys. Control. Fusion **48**, S155 (2006)
- [119] G.R. McKee *et al.*, Phys. Plasmas **7**, 1870 (2000)
- [120] T. Estrada *et al.*, Plasma Phys. Control. Fusion **51**, 124015 (2009)
- [121] G.D. Conway *et al.*, Proc. 8th Int. Reflectometry Workshop, St. Petersburg (2007)
- [122] G.D. Conway *et al.*, Plasma Phys. Control. Fusion **46**, 951 (2004)
- [123] C.H. Tröster, *Development of a flexible Doppler reflectometry system and its application to turbulence characterization in the ASDEX Upgrade tokamak*, Ph.D. thesis, Ludwig-Maximilians-Universität München (2008)
- [124] T. Happel *et al.*, Proc. 10th Int. Reflectometry Workshop, Padova (2007)
- [125] J. Schirmer *et al.*, Plasma Phys. Control. Fusion **49**, 1019 (2007)
- [126] W. Schneider *et al.*, Fusion Eng. Des. **48**, 127 (2000)
- [127] R.J. Groebner *et al.*, Nucl. Fusion **41**, 1789 (2001)
- [128] J.M. Beall *et al.*, J. Appl. Phys **53**, 3933 (1982)
- [129] R.O. Schmidt, IEEE Trans. Antennas and Propagation **AP-34**, 276 (1986)
- [130] L. Vermare *et al.*, Nucl. Fusion **52**, 063008 (2012)
- [131] M. Reich *et al.*, Plasma Phys. Control. Fusion **46**, 797 (2004)
- [132] J.W. Connor and L. Chen, Phys. Fluids **28**, 2201 (1985)
- [133] P.J. McCarthy, Phys. Plasmas **6**, 3554 (1999)
- [134] H. Sugama and T.H. Watanabe, J. Plasma Physics **74**, 139 (2008)
- [135] A. Biancalani *et al.*, Nucl. Fusion **54**, 104004 (2014)
- [136] Z. Gao *et al.*, Nucl. Fusion **49**, 045014 (2009)
- [137] Z. Gao, Phys. Plasmas **17**, 092503 (2010)

- 
- [138] F. Zonca and L. Chen, EPL **83**, 35001 (2008)
  - [139] Z. Qiu *et al.*, Phys. Plasmas **22**, 042512 (2015)
  - [140] M. Sasaki *et al.*, Plasma Fusion Res. **8**, 1403010 (2013)
  - [141] R. Singh *et al.*, Plasma Phys. Control. Fusion **57**, 125002 (2015)
  - [142] T.L. Rhodes *et al.*, Phys. Plasmas **9**, 2141 (2002)
  - [143] T. Watari *et al.*, Phys. Plasmas **12**, 062304 (2005)
  - [144] Z. Gao *et al.*, Phys. Plasmas **15**, 072511 (2008)
  - [145] Z. Gao, Phys. Plasmas **20**, 032501 (2013)
  - [146] P. Simon *et al.*, Proc. 11th International Reflectometry Workshop, Palaiseau (2013)
  - [147] S.V. Novakovskii *et al.*, Phys. Plasmas **4**, 4272 (1997)
  - [148] C. Wahlberg, Phys. Rev. Lett. **101**, 115003 (2008)
  - [149] C. Wahlberg, Plasma Phys. Control. Fusion **51**, 085006 (2009)
  - [150] S. Coda, Private communication (2016)



# Acknowledgements

This thesis could not have been written without the support of a large number of people.

I would like to thank the steering committee of the Erasmus Mundus FUSION-DC programme for giving me the opportunity to participate in the first edition of this international doctoral college. Particular acknowledgments go to *Prof. van Oost*, *Prof. Noterdaeme* and *Kathleen van Oost* for their support in all organisational matters.

I want to express my gratitude to my thesis supervisor *Prof. Ulrich Stroth*, for giving me the opportunity to work at IPP Garching, for his continued support of my work and for his help in difficult times.

A special acknowledgement goes to my direct supervisor *Dr. Garrard Conway*, for dedication beyond the call of duty. His unwavering support and his constant availability for discussing and commenting on my work were invaluable in the creation of this thesis.

Furthermore, I would like to thank *Prof. Bonhomme* and *Prof. Heuroux* from Nancy, as well as *Prof. Hirth* and *Prof. Tovar* from Stuttgart for their role as thesis promoters in this unconventional Ph.D. arrangement.

Special thanks go to *Peter Manz*, *Gregor Birkenmeier* and *Alessandro Biancalani* for valuable scientific discussions.

I would particularly like to thank my colleague and friend *Tim Happel* for making me feel welcome in Garching, both inside and outside of IPP.

For a lot of administrative help, I want to thank *Gabi Dörsch*, *Ingeborg Wagner*, *Ruth Edelmann-Amrhein* and *Dr. Matthias Walker*.

There are too many other people at IPP Garching and IGVP Stuttgart to thank each of them individually, so my thanks go to the entire teams, especially everyone in the ASDEX Upgrade control room, everyone in the turbulence group, my fellow Ph.D. students and the IPP badminton group.

Finally, I want to thank my friends and family for their continued support, including (among many others) *Jörn Rittwage*, who is both; *Martin Glindemann* and *Joe R. Dudlitz*, who joined us for many cooperative (mis)adventures; *Michael Fritschen*, *Daniel Juncu* and *Henrik Schreiber*, who share my passion for driving long distances in small vehicles; *Florian Forster* and *Christian Janning*, who always gave me a reason to visit München; *Janina Preidel*, who was by my side through many ups and downs; and *Cornelia Simon*, *Edgar Simon* and *Hannah Simon*, who are the best family that anyone could wish for.

# Curriculum Vitae

## Persönliche Daten

Name	Patrick Simon
Geburtsdatum/-ort	02.05.1987, Mülheim an der Ruhr
Familienstand	ledig
Nationalität	Deutsch

## Schulbildung

1993–1997	Grundschule Fünter Weg, Mülheim an der Ruhr
1997–2006	Otto-Pankok-Schule, Gymnasium, Mülheim an der Ruhr
Jun. 2006	Abitur (Leistungsfächer: Mathematik und Physik)

## Zivildienst

2006–2007	Zivildienst an der Rembergschule, Mülheim an der Ruhr
-----------	---

## Wissenschaftliche Ausbildung

10/2007–07/2010	Bachelorstudium der Physik an der Rheinisch-Westfälischen Technischen Hochschule Aachen
Jul. 2010	Bachelor of Science in Physik. Bachelorarbeit: <i>Kosmologische Konstante und Tests der allgemeinen Relativitätstheorie im Sonnensystem</i> , bei Prof. Dr. M. Beneke
09/2010–07/2012	Masterstudium im Erasmus-Mundus-Programm FUSION-EP, koordiniert von der Universität Gent, Belgien. Studienorte: KTH Stockholm, Schweden, Universität Carlos III zu Madrid, Spanien, Universität Stuttgart
Jul. 2012	European Master of Science in Nuclear Fusion Science and Engineering Physics. Masterarbeit: <i>Comparative database analyses of plasma edge turbulence in fusion devices</i> , an der Universität Stuttgart bei Prof. Dr. U. Stroth
seit Sep. 2012	Promotion an der Universität Stuttgart und der Université de Lorraine im Rahmen des Erasmus-Mundus-Programms FUSION-DC



## **Eidesstattliche Versicherung**

Hiermit erkläre ich an Eides Statt, dass ich diese Arbeit ausschließlich unter Anleitung meiner wissenschaftlichen Lehrer und unter Verwendung der angegebenen Hilfsmittel angefertigt habe. Sie hat weder ganz noch zum Teil an einer anderen Stelle im Rahmen eines Prüfungsverfahrens vorgelegen.

Garching bei München, den

\_\_\_\_\_

Patrick Simon